

LORENTZ-AUGMENTED ORBIT DYNAMICS AND
MISSION DESIGN

A Dissertation

Presented to the Faculty of the Graduate School

of Cornell University

in Partial Fulfillment of the Requirements for the Degree of

Doctor of Philosophy

by

Brett Jordan Streetman

August 2008

© 2008 Brett Jordan Streetman
ALL RIGHTS RESERVED

LORENTZ-AUGMENTED ORBIT DYNAMICS AND MISSION DESIGN

Brett Jordan Streetman, Ph.D.

Cornell University 2008

The concept of Lorentz Augmented Orbits (LAO) is explored and developed. A spacecraft with a controlled net electrostatic charge moves in a planetary magnetic field. Such a spacecraft experiences a Lorentz force. By proper control of the charge, useful changes to the spacecraft's orbit can be made, making Lorentz propulsion a type of propellantless propulsion.

The dynamics of such a system are explored in depth, using both analytical and numerical methods with a variety of magnetic field models. These dynamics are then applied to several novel mission designs. First, new Earth-synchronous orbits are developed using the Lorentz force. Under certain assumptions, a low-Earth, single-pass repeat groundtrack orbit exists for a constant spacecraft body charge-to-mass ratio. This behavior is then recovered under more realistic conditions, with a non-constant, feedback-controlled charge-to-mass ratio.

The potential of the Lorentz force to expand the performance and flexibility of gravity-assist maneuvers is examined. A standard flyby maneuver is limited by timing and geometry consideration. Using an LAO can open a new range of flyby options, including temporary, reversible capture of spacecraft at a target planet, along with arbitrary direction of exit asymptote. Algorithms are developed to calculate the necessary charge-to-mass ratios.

A realistic spacecraft design, using near-term technology, is developed. Mission design using the performance of this spacecraft architecture, along with a realistic geomagnetic model, is examined. The LAO approach is well suited to be used for

low-Earth inclination change maneuvers. These maneuvers can save considerable propellant, at the expense of longer maneuver duration and electrical power usage.

The possible role of LAOs in spacecraft formation flight is explored. The dynamics of a simple relative orbit system are derived, with their stability and controllability examined. A sample formation maneuver is presented.

BIOGRAPHICAL SKETCH

Brett Streetman was born in 1981 in Richmond, Virginia, to Rick and Kathy Streetman. He grew up in Richmond, graduating from Mills E. Godwin High School in 2000. Brett entered Virginia Tech in the fall of 2000 and received a Bachelor of Science in Aerospace Engineering in 2004. Brett then began graduate study at Cornell University in the fall of 2004. He received a Master of Science in Aerospace Engineering in January 2007, followed by a Ph.D. in Aerospace Engineering in August 2008.

ACKNOWLEDGEMENTS

Thank you to everyone who encouraged, helped, poked, prodded, and generally kept me moving towards this dissertation. I am confident that I chose the right place when I decided to come to Ithaca in pursuit of a graduate education.

Specifically, I would like to thank my advisor, Prof. Mason Peck. The idea of LAO was yours initially, and I was excited about it from the moment you pitched it to me as a young, fresh grad student. Throughout these years, you've been a fount of ideas as well as a sounding board for my thoughts. I greatly appreciate the freedom you gave me to travel the path of my choosing.

I would also like to thank my other committee members, Profs. Joe Burns and Mark Campbell. Joe, your initial guidance into the world of Lorentz-affected orbits proved invaluable. I also still cherish the opportunity I had to work on Cassini-related material with you. Mark, you offered advice and instruction throughout my graduate career, and I greatly appreciate that. I am also grateful for the teaching advice and experience I gained when I was your teaching assistant.

To the other grad students who have helped me along my way, I offer my thanks. From group members to office mates to friends, you've given me many things helped me, not least of which was recreation. The members of Team Peck were always there offer critiques and share ideas with. I would especially like to thank Justin Atchison, for always being behind me (physically and figuratively) on matters of LAO.

I am also grateful to all of the individuals and organizations who have helped fund my graduate work. The NSF IGERT Program in Nonlinear Systems at Cornell was an extraordinary opportunity to collaborate and step outside of my normal research pathways. Thanks to John Guckenheimer for his leadership in this program. Additionally, I received funding from the NASA Institute for Advanced

Concepts, an institution which sadly no longer exists, should be missed by the spacecraft community.

Finally, thanks to all of my family and friends for their love, support, and constant asking of “When are you going to be finished”

TABLE OF CONTENTS

Biographical Sketch	iii
Acknowledgements	iv
Table of Contents	vi
List of Tables	viii
List of Figures	ix
1 Introduction	1
1.1 Overview	1
1.2 Magnetic Fields in the Solar System	3
1.2.1 The Geomagnetic Field	4
1.2.2 Other Planetary Fields	9
1.3 Equations of Motion	11
1.3.1 Equations of Motion in a Non-tilted Dipole Field	11
1.3.2 LAOs in a Hamiltonian Formulation	12
1.3.3 General Energy and Angular Momentum Change	14
1.4 Literature Review	15
1.4.1 Lorentz-Affected Orbits in Natural Systems	16
1.4.2 Spacecraft Charging and Plasma Dynamics	17
1.4.3 Electromagnetic Propulsion Schemes	19
1.4.4 Attitude Control Via the Lorentz Force	20
1.5 Dissertation Contributions and Overview	21
2 New Synchronous Orbits Using the Geomagnetic Lorentz Force	24
2.1 Introduction	24
2.2 Applications	25
2.2.1 Polar Circular Orbit, Non-tilted Dipole Field	26
2.2.2 Equatorial Orbit, Non-tilted Dipole Field	36
2.2.3 Mitigation of Earth Oblateness Effects	44
2.2.4 Tether/LAO Comparison for GT-1 Behavior	46
2.3 Effects of a Tilted Dipole Magnetic Field	47
2.3.1 Tilted Dipole and GT-1 Behavior	48
2.3.2 Recovery of GT-1 Using a Non-constant Charge	51
2.3.3 Feedback Control for $\frac{q}{m}$	55
2.4 Chapter Conclusions	65
3 Gravity-Assist Maneuvers Augmented by the Lorentz Force	67
3.1 Introduction	67
3.1.1 Perturbation Equations	68
3.1.2 Planetary Magnetic Fields	69
3.1.3 Gravity-Assist Maneuvers	69
3.2 Applications	72
3.2.1 Single-Orbit Lorentz Modifications	72

3.2.2	Lorentz Augmented Capture	77
3.2.3	Flyby Shaping Using a Temporary Jovian Capture	83
3.3	Chapter Conclusions	93
4	A General Bang-Off Control Method For Lorentz Augmented Orbits	94
4.1	Introduction	94
4.1.1	Lorentz Perturbations in Spherical Coordinates	94
4.1.2	Partitioning The Geomagnetic Field	97
4.2	Space Vehicle Design	99
4.2.1	Capacitance	100
4.2.2	Power	102
4.2.3	Space Vehicle Mass	103
4.2.4	Performance Estimates	104
4.3	LAO Maneuvers and Limitations	106
4.3.1	Maneuver Limitations	106
4.3.2	Example Maneuver: LEO Inclination Change and Orbit Raising	109
4.3.3	Example Maneuver: GEO Transfer Inclination Change	115
4.4	LAO Power Consumption and Plasma Density-based Control	117
4.5	Chapter Conclusions	121
5	Formation Flight Using the Lorentz Force	124
5.1	Relative Dynamics and Controllability Analysis	124
5.2	Simple LAO Formation Maneuver	131
5.3	Chapter Conclusions	134
6	Conclusion	135
6.1	Summary and Conclusions	135
6.2	Recommendations for Future Work	136
A	Magnetic Potential and Field Expansions	139
B	Canonical Variables and Hamiltonians	142
	Bibliography	145

LIST OF TABLES

1.1	Comparison of planetary magnetospheres throughout the Solar System.	10
2.1	Physical parameters common to all simulations.	33
2.2	Initial conditions for polar, circular orbit.	35
2.3	Initial conditions for equatorial, constant charge integration.	41
4.1	Zone Properties	99
4.2	Space Vehicle Mass Model	104
4.3	Example of Power Calculation for A Spacecraft in a 600km Altitude LEO Circular Orbit at an Inclination of 28.5°	105
4.4	Example of Mass Calculation	106
4.5	LAO Effects for $\frac{q}{m} < 0$ in LEO	108
4.6	Limiting Power Usage Via n_e (in m^{-3}) Sensing for 3 Day Simulations at an Initial Inclination of $i = 28.5^\circ$ at an Altitude of 600 km	119
4.7	Comparison of Power Usage During Both the Hybrid Simulation and the Original, Constant Charge Simulation.	122
5.1	Relative strength of the Lorentz force and the Coulomb force between charged spacecraft.	125

LIST OF FIGURES

1.1	Spherical coordinates used in the derivation of the equations of motion.	5
1.2	Contour plot of the radial component of the geomagnetic field over latitude and longitude. The black contour represents zero. The dashed grey contours are values less than zero; the red contours are values greater than zero.	7
1.3	Contour plot of the component of the geomagnetic field in the $\hat{\phi}$ direction over latitude and longitude. The black contour represents zero. The dashed grey contours are values less than zero; the red contours are values greater than zero.	8
1.4	Contour plot of the component of the geomagnetic field in the $\hat{\theta}$ direction over latitude and longitude. The black contour represents zero. The dashed grey contours are values less than zero; the red contours are values greater than zero.	9
2.1	Graphical representation of the vectors involved in an LAO GT-1 orbit.	30
2.2	Track of a GT-1 LAO orbit in a frame rotating with Earth with $\frac{q}{m} = 2.83$ C/kg.	34
2.3	Comparison of gravitational and Lorentz acceleration magnitudes for a GT-1 LAO orbit with $\frac{q}{m} = 2.83$ C/kg.	34
2.4	Time rate of change in right ascension for a GT-1 LAO orbit with $\frac{q}{m} = 2.83$ C/kg. The top plot shows both analytical and numerical calculations of the right ascension. The bottom plot shows the error between these two curves.	36
2.5	Time rate of change of orbital energy for a GT-1 LAO orbit with $\frac{q}{m} = 2.83$ C/kg.	37
2.6	Earth-fixed orbital path of an equatorial, constant charge LAO satellite with $\frac{q}{m} = -1.77$ C/kg, calculated for synchronous perigee movement.	42
2.7	Argument of perigee angle of an equatorial, constant charge LAO satellite with $\frac{q}{m} = -1.77$ C/kg. The top plot shows both analytical and numerical calculations of the argument of perigee. The bottom plot shows the error between these two curves.	43
2.8	Comparison between two integrations with the same initial conditions. The left plot uses a non-tilted dipole field; the right used a dipole field tilted to 10°	49
2.9	The orbital energy of two tilted dipole integrations with $\frac{q}{m} = -1.77$ C/kg, set to give GT-1 behavior. The left plot is for $\Omega' = -90^\circ$. The right shows an initial angle of $\Omega' = +90^\circ$	51

2.10	Right ascension and energy error over 15 days for a spacecraft using the variable charge-to-mass scheme defined in Eqs. 2.63 and 2.67. The desired average right ascension is 0° . The orbit is initially a 400 km altitude circle. The geomagnetic field is tilted to 10°	55
2.11	Right ascension and energy error over 15 days for a spacecraft under a constant charge. The desired average right ascension is 0° . The orbit is initially a 400 km altitude circle. The geomagnetic field is tilted to 10°	56
2.12	Right ascension and energy error over 15 days for a spacecraft using the feedback control scheme defined in Eq. 2.68. The desired average right ascension is 0° . The orbit is initially a 400 km altitude circle. The geomagnetic field is tilted to 10°	61
2.13	Right ascension and energy error over 15 days for a spacecraft using the open loop scheme and the feedback controller. The desired average right ascension is 70° . The orbit is initially a 400 km altitude circle. The geomagnetic field is tilted to 10°	62
2.14	Right ascension and energy error over 75 days for a spacecraft using the feedback control scheme defined in Eq. 2.68. The desired average right ascension is 45° . The orbit is initially a 400 km altitude circle. The geomagnetic field is tilted to 10°	63
2.15	Matrix norm of the state transition matrix of the system in Eq. 2.71 using data from the simulation shown in Fig. 2.14.	64
2.16	Resampled right ascension error over 75 days for the simulation displayed in Fig. 2.14. The actual right ascension error is Fourier transformed. The power spectral density of this transform is used to find the two main frequencies present, and the error is numerically resampled at the difference between these frequencies. The long-term average error is also subtracted off to create a zero-mean system.	65
3.1	Flyby trajectory vector definitions. The dotted vectors in the heliocentric view indicate a possible LAO trajectory resulting in a significantly larger ΔV	70
3.2	Hyperbolic orbit for single-orbit rotation of periapsis, showing the Keplerian orbit, the numerically calculated solution, and the perturbation solution for charge-to-mass ratio.	76
3.3	Capture of an LAO spacecraft in one half-orbit. The left figure displays the orbital track of the satellite. The right figure shows both the true anomaly of the spacecraft and the spacecraft charge. The charge is turned on as the spacecraft passes through perijove and remains on as it is captured.	81

3.4	Escape of an LAO spacecraft in one half-orbit. The left figure displays the orbital track of the satellite. The right figure shows both the true anomaly of the spacecraft and the spacecraft charge. The charge is initially on and is then is turned off as the spacecraft passes through perijove.	81
3.5	The four stages of the capture and precess scenario.	86
3.6	Arbitrary exit flyby trajectory. The chosen exit angle is 2π , or exactly opposite of the entrance angle. The number of elliptical orbits is 20 and the charge-to-mass ratio is -1.098 C/kg.	91
3.7	Arbitrary exit flyby charge-to-mass ratio. $\frac{q}{m}$ is initially 0 and then increases to -1.098 C/kg at the first perijove. The charge remains constant through all 20 orbits and goes to 0 at the final perijove.	92
3.8	Arbitrary exit flyby orbital eccentricity. The eccentricity is initially hyperbolic, but is reduced to an elliptical value. Through each orbit e oscillates between values above one and below one, until the final escape.	93
4.1	Eight distinct zones of the geomagnetic field, numbered I-VIII.	98
4.2	LAO spacecraft with cylindrical stocking capacitor. The dotted line surrounding the capacitor suggests the effective boundary of the plasma sheath.	101
4.3	Orbit Average Power and $\frac{q}{m}$ vs. Capacitor Potential	107
4.4	Effect of Earth oblateness on the eccentricity under the quadrant control.	111
4.5	Orbital elements for the LEO plane-change and orbit-raising maneuver.	112
4.6	Optimal charge-to-mass ratio for inclination change.	114
4.7	Orbital elements for the GTO plane-change maneuver. Plot (a) is the semimajor axis, plot (b) is the inclination, plot (c) is the orbital eccentricity, and plot (d) is the argument of perigee.	116
4.8	Comparison of hybrid simulation of constant charge-to-mass ratio with plasma density-limited control to constant $\frac{q}{m}$ only control.	121
5.1	Reference Coordinates	125
5.2	Track of the formation satellites with reference frame centered on Satellite A. Circular points represent starting positions, with triangular points denoting finishing positions.	133
5.3	Charge-to-mass ratio in C/kg for each LAO satellite in the formation. The maximum q/m ratio for each satellite was capped at a magnitude of 0.005 C/kg.	134

CHAPTER 1

INTRODUCTION

1.1 Overview

There are two fundamentally different types of spacecraft propulsion: traditional and propellantless. Traditional propulsion systems store propellant in some form onboard the spacecraft. This propellant is then expelled from the spacecraft with some momentum, imparting an equal and opposite momentum to the spacecraft. Propellantless propulsion systems expend no propellant. Instead, these systems exchange energy and momentum with the spacecraft's environment in some way. Some propellantless propulsion techniques, such as solar sails, harvest momentum expelled from the sun.[1] Others, such as electrodynamic tethers, interact with a magnetic field to do work upon the spacecraft.[2] Propellantless propulsion can greatly extend the lifetime of a traditional spacecraft mission by eliminating the need for such expendables. Additionally, propellantless propulsion can enable novel mission designs not possible with traditional propulsive systems.

The propellantless propulsion technique discussed herein allows one to realize a Lorentz Augmented Orbit (LAO). An LAO-capable spacecraft carries a net electrostatic charge, either an excess of electrons or ions. Such a spacecraft behaves as charged particle subject to interactions with a planetary magnetic field. We begin with a summary of the elementary electrodynamics involved. The Lorentz force experienced by a particle of charge q (Coulombs) moving through a magnetic field \mathbf{B} is given by

$$\mathbf{F}_L = q\mathbf{v}_r \times \mathbf{B} \tag{1.1}$$

where \mathbf{v}_r is the particle velocity with respect to the magnetic field. This force,

named after Dutch physicist and Nobel Prize winner Hendrik Lorentz, accelerates a spacecraft that is already subject to the force of gravity, augmenting the familiar Keplerian dynamics. An LAO exploits the interaction between a planetary magnetic field and an electrostatic charge built up on a satellite.[3] Thus, an LAO results from electrodynamic propulsion that does not require a tether. A tether system normally entails a long conductive wire, through which a current is forced. The drifting electrons in the tether provide the moving charged particles necessary for the Lorentz force. In the LAO scheme, the spacecraft itself becomes the moving charged particle, creating a current along its orbital path.

An LAO is achieved by a spacecraft that uses electrical power to maintain a net electrostatic charge on its body, and this net charge causes an interaction between the magnetic field and the vehicle in the form of the Lorentz force. The magnitude and direction of the force are defined by the size and polarity of the charge on the satellite q , the velocity of the vehicle with respect to the magnetic field \mathbf{v}_r , and the strength and direction of the magnetic field \mathbf{B} :

$$\mathbf{F}_L = q(\mathbf{v} - \boldsymbol{\omega}_E \times \mathbf{r}) \times \mathbf{B} \quad (1.2)$$

where the position of the satellite is given by \mathbf{r} , and $\boldsymbol{\omega}_E$ represents the planet's angular velocity. In an inertial frame the planetary magnetic fields rotate with the planet.[4] The relative velocity, \mathbf{v}_r , that causes the Lorentz force results from the difference between the inertial spacecraft velocity, \mathbf{v} , and the velocity of the magnetic field, $\boldsymbol{\omega}_E \times \mathbf{r}$. The power system of the satellite can then modulate the net charge to control the propulsive force.

The energy stored in a planet's rotation is used to do work on the vehicle, as is seen more clearly in Section 1.3. The size of the force is limited by only the charge-holding capacity (i.e. its self capacitance) and available power of the

satellite. However, the direction of thrust is fixed with respect to the velocity direction of the spacecraft and the direction of the magnetic field. This limitation is not so restrictive as to render the system useless, though. With appropriate planning and orbit design, many useful applications of Lorentz propulsion can be realized.

This dissertation sets out to describe the dynamics of an LAO. Informed by these dynamics, we create new missions and applications using LAOs. While the effect of the Lorentz force on natural systems is well documented and understood (see Section 1.4), the use of the Lorentz force to achieve spacecraft engineering mission design goals is a new contribution. This dissertation attempts to identify possible uses of LAOs in meaningful missions by examining Lorentz-augmented dynamics, control, applications, and spacecraft design.

This chapter continues with an review of magnetic fields present in the Solar System, with a particular emphasis on the Earth's field, including a description of the three field models used in this dissertation. This section is followed by a derivation of the equations of motion that describe an LAO, along with general expressions for the change in energy and angular momentum of a charged spacecraft. The first chapter concludes with a review of relevant literature and an overview of the rest of the dissertation.

1.2 Magnetic Fields in the Solar System

The LAO concept can be applied to a spacecraft mission that involves an orbit around any central body that has an appreciable magnetic field. This work considers the fields of Earth and Jupiter primarily, but the general principles are

not restricted to these planets. The Sun also has a magnetic field, but it is not examined in depth here.

1.2.1 The Geomagnetic Field

The Earth's magnetic field is a complex structure. Several models of varying depth and accuracy are used to describe it in this dissertation. The simplest but least accurate model of the Earth's magnetic field is a dipole aligned with Earth's spin axis, referred to herein as the non-tilted dipole model. This model is used in parts of Chapter 2, Chapter 3, and Chapter 5. A more accurate model is the tilted dipole model, a dipole field that has been tilted some angle away from the Earth's spin axis (or true north pole). This tilted dipole model is used in Chapter 2. Finally, the most accurate model is a full spherical harmonic model. This type of model uses many coefficients, such as the International Geomagnetic Reference Field, to describe the field in terms of spherical harmonic functions. In particular, this dissertation uses the IGRF95 (or IGRF-7) model[5]. This model is used in Chapter 4. Based on the magnitudes of these spherical harmonic coefficients, one can say that the non-tilted dipole component represents about 75% of the field, with the tilted dipole adding another 15%, and higher-order components combining for the remaining 10%. An important note on the magnetic field is that it is represented in Earth-fixed coordinates. The field itself is locked in step with the rotation of the Earth, as shown in Rothwell.[4] In implementing either the tilted dipole or spherical harmonic models, one must be careful to distinguish between Earth-fixed longitudes and inertial longitudes.

Most of the dynamics examined in this work use a spherical coordinate system. The spherical coordinates consist of radius r , colatitude angle ϕ , and azimuth from

the x -direction θ , as shown in Fig. 1.1. The unit vector $\hat{\mathbf{n}}$ represents the Earth's

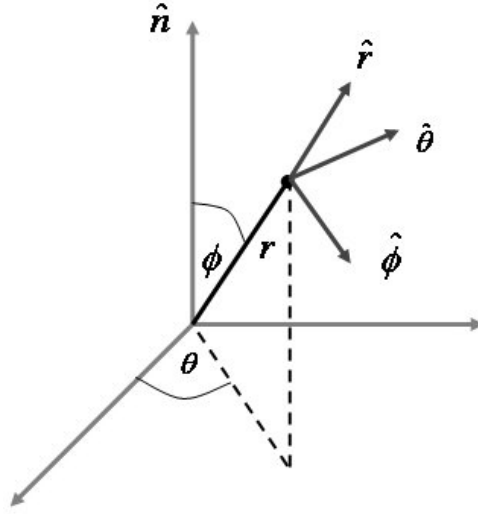


Figure 1.1: Spherical coordinates used in the derivation of the equations of motion.

spin axis, with the x - and y -directions being in the equatorial plane. The x -direction is inertially fixed and aligned with the first point of Ares. The non-tilted dipole magnetic field is expressed as

$$\mathbf{B} = \frac{B_0}{r^3} [2 \cos \phi \hat{\mathbf{r}} + \sin \phi \hat{\phi} + 0\hat{\theta}] \quad (1.3)$$

where B_0 is the strength of the field in Weber-meters, and the unit vectors are as shown in Fig. 1.1. The field rotates with the Earth. In the non-tilted field case, r and ϕ are equivalent in both the rotating field frame and the inertial frame. Because the dipole is axisymmetric, the magnetic azimuth does not directly contribute to the Lorentz force. For the Earth, the geographic North Pole is in fact the magnetic South Pole; the north side of a compass needle is attracted to the geomagnetic south pole. We desire a coordinate system that has geographic north in the z -direction, so we work with a dipole field that is essentially flipped upside down. We correct for this fact by using a B_0 term that is negative.

The tilted-dipole model is implemented with two new parameters: α represents the angle between the magnetic north pole and geographic north pole, and Ω_m represents the longitude of the magnetic north as measured from the inertial x -axis. As the geomagnetic field is locked in step with the Earth's rotation, Ω_m varies with respect to time as

$$\Omega_m = \omega_E t + \Omega_m(0) \quad (1.4)$$

where $\Omega_m(0)$ is the initial location of the magnetic pole. The general vector model of a dipole field is

$$\mathbf{B} = \frac{B_0}{r^3} \left[3(\hat{\mathbf{N}} \cdot \hat{\mathbf{r}})\hat{\mathbf{r}} - \hat{\mathbf{N}} \right] \quad (1.5)$$

where $\hat{\mathbf{N}}$ is a unit vector along the magnetic north pole. α is the angle between $\hat{\mathbf{N}}$ and $\hat{\mathbf{n}}$. This quantity is independent of time. The angle Ω_m depends on time and locates the $\hat{\mathbf{N}}$ vector. $\hat{\mathbf{N}}$ is fixed in an Earth-fixed frame, but rotates in an inertial frame. For the Earth, the magnetic north pole is in northern Canada, with $\alpha = 11.7^\circ$ and an Earth-fixed longitude of -114° .

The spherical harmonic model of the Earth's magnetic field can be made arbitrarily complex. The field takes the form of

$$\mathbf{B} = \sum_{n=1}^{\infty} \sum_{m=0}^n \mathbf{B}_{n,m} \quad (1.6)$$

where $\mathbf{B}_{n,m}$ is the component of the magnetic field of degree n and order m . See Roithmayr[6] for explicit calculations of $\mathbf{B}_{n,m}$. The magnetic field can also be defined by the magnetic vector potential field \mathbf{A} , where

$$\mathbf{B} = \nabla \times \mathbf{A} \quad (1.7)$$

The magnetic vector potential field can be used in Hamiltonian formulations of

the dynamics of the systems. The components of the \mathbf{A} can be written as[7]

$$\mathbf{A}_{n,m} = R_E \left[\left(\frac{1}{n} \right) \left(\frac{R_E}{r} \right)^{n+1} \left\{ m \frac{P_n^m(\cos \phi)}{\sin \phi} [-g_{n,m} \sin m\theta + h_{n,m} \cos m\theta] \hat{\phi} - \frac{\partial(P_n^m(\cos \phi))}{\partial \phi} [g_{n,m} \cos m\theta + h_{n,m} \sin m\theta] \hat{\theta} \right\} \right] \quad (1.8)$$

where R_E is the radius of the Earth, P_n^m represents the associated Legendre functions, and $g_{n,m}$ and $h_{n,m}$ are IGRF coefficients. The θ values in Eq. 1.8 must be represented in an Earth-fixed coordinate system. Expressions for $\mathbf{A}_{n,m}$ and $\mathbf{B}_{n,m}$ up to $n = m = 2$ are given in Appendix A.

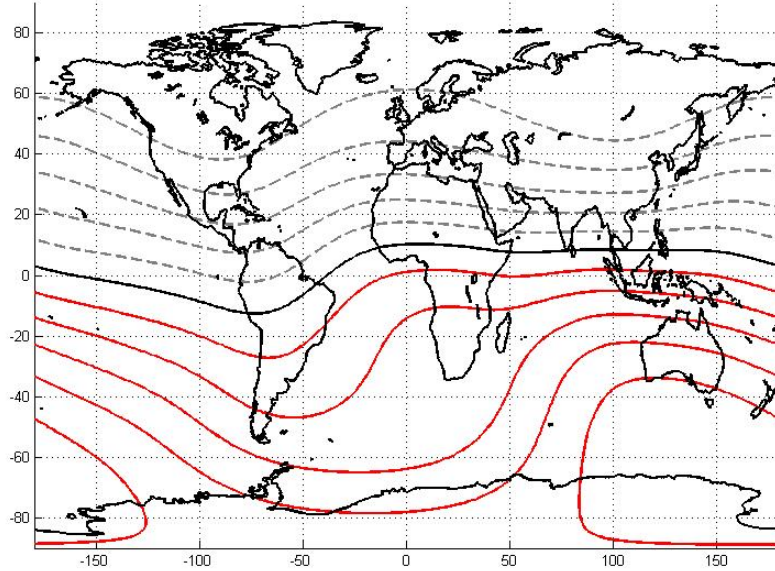


Figure 1.2: Contour plot of the radial component of the geomagnetic field over latitude and longitude. The black contour represents zero. The dashed grey contours are values less than zero; the red contours are values greater than zero.

Figure 1.2 shows a contour plot of $(\mathbf{B} \cdot \hat{\mathbf{r}})$ over (Earth-fixed) latitude and longitude at an altitude of 600 km. Positive values are represented by red contours, and negative contours are dashed grey. The black contour is referred to as the

magnetic equator and indicates where the radial component is zero. In the traditional lexicon, the magnetic equator is where the field has no inclination (or “dip”). For the non-tilted dipole model, the magnetic equator would lie on the latitudinal equator, but the additional higher-degree terms modify its location significantly.

Figure 1.3 shows a contour plot of $(\mathbf{B} \cdot \hat{\phi})$. Again, dashed grey contours are

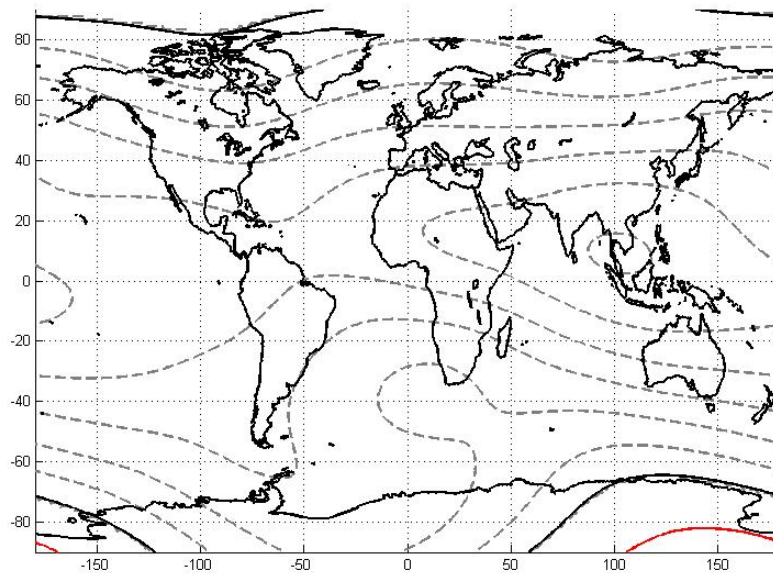


Figure 1.3: Contour plot of the component of the geomagnetic field in the $\hat{\phi}$ direction over latitude and longitude. The black contour represents zero. The dashed grey contours are values less than zero; the red contours are values greater than zero.

negative and red positive, with black being zero. The $\hat{\phi}$ -component of the field is generally negative, except for small polar regions. The $\hat{\phi}$ -component is small near these polar regions and is largest near the magnetic equator.

Figure 1.4 shows a contour plot of $(\mathbf{B} \cdot \hat{\theta})$. The contour colors are as above. Figure 1.4 shows distinct regions of positive and negative values. The zero contour represents the line of zero declination (or zero difference between true north and

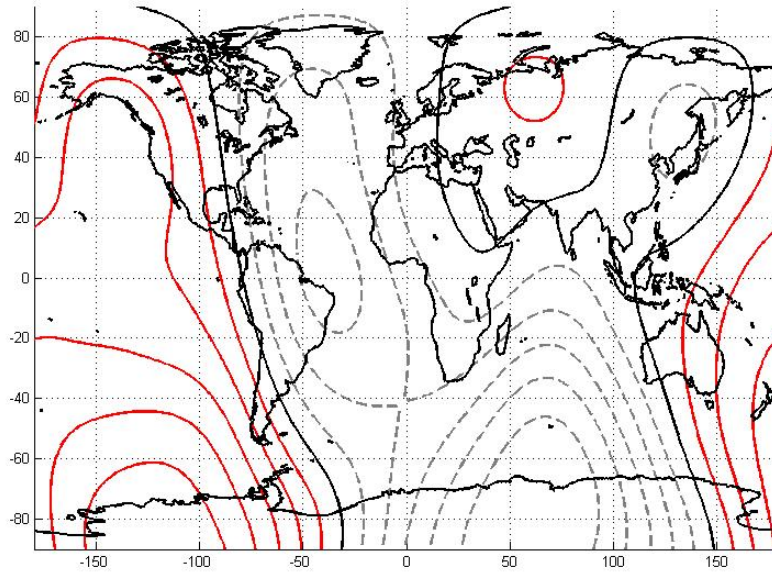


Figure 1.4: Contour plot of the component of the geomagnetic field in the $\hat{\theta}$ direction over latitude and longitude. The black contour represents zero. The dashed grey contours are values less than zero; the red contours are values greater than zero.

magnetic north). The dipole component of the field (and all other zero-order terms) contributes nothing to the $\hat{\theta}$ -component of the field.

1.2.2 Other Planetary Fields

Most of the planets in the Solar System have significant magnetic fields. Russell provides a survey of planetary magnetospheres.[8] Of the planets, six have appreciable internally generated magnetic fields (Mercury, Earth, Jupiter, Saturn, Uranus, and Neptune). Mars and Venus have such small and irregular fields that Lorentz propulsion is not a viable technique. Mercury's small magnetic field (about 1/3000th the strength of Earth's) and gravitational field make it another unlikely

Lorentz flyby target. The gas giants all have significant magnetic fields. Jupiter possesses by far the strongest magnetic field in the Solar System, with a magnetic moment about 18,000 times as strong as Earth's. Table 1.1 lists the relative magnetic field strength of each planet in the Solar System.

Table 1.1: Comparison of planetary magnetospheres throughout the Solar System.

Planet	Orbit Radius (AU)	Magnetic Moment[8] (compared to Earth)	Tilt of Dipole Component (°)[9]
Mercury	0.39	4×10^{-4}	14
Venus	0.72	~ 0	N/A
Earth	1	1	11.7
Mars	1.52	~ 0	N/A
Jupiter	5.20	1.8×10^4	9.6
Saturn	9.54	580	0.0
Uranus	19.2	50	58.6
Neptune	30.1	24	46.8

The six planets with intrinsic magnetic fields all have relatively strong dipole components. In most planets, the dipole component of the field is tilted at some angle. These angles are shown in Table 1.1. For the small tilt angles of Earth, Jupiter, and Saturn, equatorial orbits are reasonably well modeled with a non-tilted field. Chapter 2 details the effect of a tilted field on LAOs.

1.3 Equations of Motion

In this section, we derive several basic equations that describe the motion of a spacecraft in an LAO. The full equations of motion are derived using the simple non-tilted dipole magnetic field model. These simple equations of motion are followed by a more general treatment of LAOs using a Hamiltonian formulation. The section ends with a general treatment of the changes in orbital energy and angular momentum caused by the Lorentz force.

1.3.1 Equations of Motion in a Non-tilted Dipole Field

We describe the motion of a spacecraft in an LAO in the spherical coordinate frame shown earlier in Fig. 1.1. The acceleration of the spacecraft including two-body gravity and the Lorentz force (per unit mass) in these (inertially referenced) coordinates is given by

$$\mathbf{a} = \mathbf{F}/m = -\frac{\mu}{r^3}\mathbf{r} + \frac{q}{m}(\mathbf{v} - \omega_E\hat{\mathbf{n}} \times \mathbf{r}) \times \mathbf{B} \quad (1.9)$$

where $\frac{q}{m}$ is the charge-to-mass ratio of the satellite in Coulombs per kilogram (C/kg), and $\hat{\mathbf{n}}$ is a unit vector in the direction of the true north pole.

Expressing the Lorentz acceleration in the spherical, inertial frame yields

$$\mathbf{F}_L = \frac{q}{m} \frac{B_0}{r^3} \begin{bmatrix} -r\dot{\theta} \sin^2 \phi + \omega_E r \sin^2 \phi \\ 2r\dot{\theta} \sin \phi \cos \phi - 2\omega_E r \cos \phi \sin \phi \\ \dot{r} \sin \phi - 2r\dot{\phi} \cos \phi \end{bmatrix} \quad (1.10)$$

Combining the Lorentz term with gravity and the standard accelerations in spher-

ical coordinates gives the following three equations of motion:

$$\ddot{r} = r\dot{\theta}^2 \sin^2 \phi + r\dot{\phi}^2 - \frac{\mu}{r^2} - \frac{q}{m} \frac{B_0}{r^3} [r\dot{\theta} \sin^2 \phi - \omega_{ER} \sin^2 \phi] \quad (1.11)$$

$$\begin{aligned} r\ddot{\phi} &= -2\dot{r}\dot{\phi} + r\dot{\theta}^2 \sin \phi \cos \phi + \frac{q}{m} \frac{B_0}{r^3} 2[r\dot{\theta} \sin \phi \cos \phi \\ &\quad - \omega_{ER} \cos \phi \sin \phi] \end{aligned} \quad (1.12)$$

$$r\ddot{\theta} \sin \phi = -2\dot{r}\dot{\theta} \sin \phi - 2r\dot{\phi}\dot{\theta} \cos \phi + \frac{q}{m} \frac{B_0}{r^3} [\dot{r} \sin \phi - 2r\dot{\phi} \cos \phi] \quad (1.13)$$

Equations 1.11, 1.12, and 1.13 represent a sixth-order system that describes the motion of any charged satellite in a non-tilted dipole magnetic field.

1.3.2 LAOs in a Hamiltonian Formulation

The general motion of a charged particle in both magnetic and gravitational fields was described in a Hamiltonian framework by Schaffer and Burns in 1994.[7] This section replicates that work in terms of our preferred coordinates. Here, the Hamiltonian formulation is derived in a frame that rotates with the planet of interest. In such a frame, the system Hamiltonian, H , is constant regardless of whether the charge is constant.[7]

We begin the derivation of the Hamiltonian system by first describing the Lagrangian, L , where $L = T - U$, with T being the total kinetic energy in the rotating frame and U being the total potential energy. The kinetic energy of the spacecraft in the rotating frame in spherical coordinates is

$$T = \frac{1}{2} m \mathbf{v}^T \mathbf{v} = \frac{1}{2} m (\dot{r}^2 + r^2 \dot{\phi}^2 + r^2 \sin^2 \phi \dot{\theta}^2) + \frac{1}{2} m (\omega_{ER}^2 r^2 \sin^2 \phi + 2\omega_{ER} r^2 \sin^2 \phi \dot{\theta}) \quad (1.14)$$

Using two-body gravity, the gravitational potential energy is given by

$$U_g = m \frac{\mu}{r} \quad (1.15)$$

To find the magnetic potential energy, we must use the magnetic potential field \mathbf{A} defined in Section 1.2. Using the definition of \mathbf{A} , the magnetic potential energy is

$$U_m = -q(\mathbf{v} \cdot \mathbf{A}) = -q(r \sin \phi \dot{\theta} \mathbf{A} \cdot \hat{\theta} + r \dot{\phi} \mathbf{A} \cdot \hat{\phi}) \quad (1.16)$$

The total potential energy is the sum of the magnetic and gravitational terms, making the Lagrangian

$$L = \frac{1}{2}m(\dot{r}^2 + r^2\dot{\phi}^2 + r^2 \sin^2 \phi \dot{\theta}^2) + \frac{1}{2}m(\omega_E^2 r^2 \sin^2 \phi + 2\omega_E r^2 \sin^2 \phi \dot{\theta}) \quad (1.17)$$

$$-m\frac{\mu}{r} + q(\mathbf{v} \cdot \mathbf{A}) - q(r \sin \phi \dot{\theta}(\mathbf{A} \cdot \hat{\theta}) + r \dot{\phi}(\mathbf{A} \cdot \hat{\phi}))$$

With L , we can define the canonical coordinates and momenta of the Hamiltonian system. Choosing the three canonical coordinates as the three spherical coordinates, r , ϕ , and θ , the three conjugate momenta are

$$p_r = \frac{\partial L}{\partial \dot{r}} = m\dot{r} \quad (1.18)$$

$$p_\phi = \frac{\partial L}{\partial \dot{\phi}} = mr^2\dot{\phi} + qr(\mathbf{A} \cdot \hat{\phi}) \quad (1.19)$$

$$p_\theta = \frac{\partial L}{\partial \dot{\theta}} = mr^2 \sin^2 \phi (\dot{\theta} + \omega_E) + qr \sin \phi (\mathbf{A} \cdot \hat{\theta}) \quad (1.20)$$

The Hamiltonian can then be written as

$$H = \sum_{i=1}^3 p_i \dot{q}_i(p_i, q_i) \quad (1.21)$$

which yields the expression

$$H = \frac{1}{2m}(p_r)^2 + \frac{1}{2mr^2}(p_\phi - qr(\mathbf{A} \cdot \hat{\phi}))^2 \quad (1.22)$$

$$+ \frac{1}{2mr^2 \sin^2 \phi}(p_\theta - mr^2 \omega_E \sin^2 \phi - qr \sin \phi (\mathbf{A} \cdot \hat{\theta}))^2$$

$$+ m\frac{\mu}{r} - \frac{1}{2}mr^2 \omega_E^2 \sin^2 \phi$$

This Hamiltonian is generally applicable for any magnetic potential field \mathbf{A} .

Appendix B gives the canonical variables and Hamiltonian for various terms of the spherical harmonic model for \mathbf{A} up to order and degree 2. In this appendix, these quantities appear for isolated harmonics. That is to say, each Hamiltonian given in Appendix B elucidates the effect of a single isolated harmonic term. These Hamiltonians are not valid for the full system of many harmonics added together.

1.3.3 General Energy and Angular Momentum Change

General time rates of change of energy and angular momentum due to the Lorentz force are derived. With these derivatives, the time rates of change of various orbital elements can be found following the method of Burns.[10] The work-energy principle states

$$\dot{E} = \mathbf{v} \cdot \mathbf{F} \quad (1.23)$$

where E is the total energy of the system per unit mass, \mathbf{F} is the applied force per unit mass, and \mathbf{v} is the body's velocity. Including the Lorentz force gives

$$\dot{E} = \mathbf{v} \cdot \left(\frac{q}{m} \mathbf{v}_r \times \mathbf{B} \right) \quad (1.24)$$

Substituting for \mathbf{v}_r gives

$$\dot{E} = \mathbf{v} \cdot \left(\frac{q}{m} \mathbf{v} \times \mathbf{B} \right) - \mathbf{v} \cdot \left[\frac{q}{m} (\omega_E \hat{\mathbf{n}} \times \mathbf{r}) \times \mathbf{B} \right] \quad (1.25)$$

The $\mathbf{v} \cdot (\mathbf{v} \times \mathbf{B})$ term is zero, yielding

$$\dot{E} = \frac{q}{m} \mathbf{v} \cdot [\mathbf{B} \times (\omega_E \hat{\mathbf{n}} \times \mathbf{r})] \quad (1.26)$$

Equation 1.26 shows that only the rotation of the magnetic field allows the Lorentz force to do work on the satellite. A general magnetic force is conservative; thus the change in energy comes not from the magnetic field, but indirectly from the

rotation of the Earth. Equivalently, a moving magnetic field is associated with an electric field, and this induced electric field can do work on a satellite.

Applying the triple cross product identity to Eq. 1.26 yields

$$\dot{E} = \frac{q}{m}\omega_E [(\mathbf{v} \cdot \hat{\mathbf{n}})(\mathbf{B} \cdot \mathbf{r}) - (\mathbf{v} \cdot \mathbf{r})(\hat{\mathbf{n}} \cdot \mathbf{B})] \quad (1.27)$$

Equation 1.27 is general. It describes any orbit or magnetic field configuration.

Change in orbital angular momentum arises from the torques applied to the system by the Lorentz force, or

$$\dot{\mathbf{h}} = \mathbf{r} \times \mathbf{F}_L \quad (1.28)$$

where \mathbf{h} is the angular momentum per unit mass of the system. Substituting for \mathbf{F}_L and simplifying gives

$$\dot{\mathbf{h}} = \mathbf{r} \times \left(\frac{q}{m}\mathbf{v} \times \mathbf{B} \right) + \mathbf{r} \times \left(\mathbf{B} \times \left[\frac{q}{m}\omega_E \hat{\mathbf{n}} \times \mathbf{r} \right] \right) \quad (1.29)$$

Applying the triple cross product formula to both terms and simplifying further yields the following general expression:

$$\dot{\mathbf{h}} = \frac{q}{m} [(\mathbf{B} \cdot \mathbf{r})\mathbf{v} - (\mathbf{r} \cdot \mathbf{v})\mathbf{B} - \omega_E(\mathbf{B} \cdot \mathbf{r})(\hat{\mathbf{n}} \times \mathbf{r})] \quad (1.30)$$

Depending on the orbital and magnetic configurations, we may change both the magnitude and direction of the angular momentum vector. Changing the direction of this vector allows some measure of control over both the inclination and right ascension angle of the orbit.

1.4 Literature Review

The field of Lorentz Augmented orbits is a new area of research interest. The work of Hough[11] represents the only known previously published study of the

effect of the Lorentz force on the orbit of a charged, man-made spacecraft. Hough presented the effect of charging on the targeting accuracy of a ballistic missile (and found it to be negligible). LAO work draws on wide variety of previous scholarship and fields of study, including natural systems that exhibit Lorentz effects, general studies of spacecraft charging, plasma dynamics, formation flight actuators, and electrodynamic tether propulsion.

The concept of the Lorentz Augmented Orbit was first described by Peck[3] in 2005. This work was expanded to produce the material in Chapter 2, and published in 2007.[12]. Atchison, et al. looked at the prospect of capturing spacecraft at Jupiter using the Lorentz force.[13] Chapter 3 presents a complementary look at LAOs and planetary flybys, and draws from material published in 2007.[14] Chapters 4 and 5 are drawn from works published in 2008[15] and 2007[16], respectively.

1.4.1 Lorentz-Affected Orbits in Natural Systems

Magnetically active planets in the Solar System, including Earth, have an ionosphere, a region of plasma around the planet. This plasma, along with photoelectric excitation via the Sun, tends to impart some net electrostatic charge on any orbiting body. This charge causes the most perturbation to small dust grains. The Lorentz force acting on these small particles can be used to explain several natural planetary ring phenomena.

Axford and Mendis produced some early work on the motion of charged micrometeoroids.[17] Their work was based on the photometric changes of outer planet satellites observable on Earth that could be caused by charged particles, and included a study of equatorial charged particle dynamics in the Saturnian system.

Littlejohn in 1979 and 1982[18, 19] discusses perturbation solutions for the motion of charged particles. He uses a Hamiltonian formulation, but in noncanonical variables to avoid the use of the magnetic vector potential.

The Lorentz effect has been studied in further depth. Morfill produced a summary of electromagnetic effect on rings in 1983.[20] Burns, et al. in 1985 first discussed the role of Lorentz resonances in shaping planetary ring features.[21] Schaffer and Burns analyzed the dynamics of dust particles charged by the plasma environment around Jupiter[22, 7]. They show that the motions of these small charged grains can be greatly affected by Lorentz mechanics. This mechanism can be used to explain sparse, latitudinally thick rings found around Jupiter's main rings. Hamilton derives expressions for time-averaged perturbation equations of dust particles around Saturn,[23] some of which are also derived here. Colwell and Horanyi[24] and Colwell, et al.[25] described how interplanetary dust can be captured by Jupiter's magnetic field into stable orbits. Gustafson and Lederer described the effect of the Lorentz force from the Sun's magnetic field on interstellar dust particles.[26] This is by no means an exhaustive list of Lorentz-affected orbit research, but should provide an overview of the field.

1.4.2 Spacecraft Charging and Plasma Dynamics

Just as dust grains naturally achieve some nonzero charge around Jupiter, a spacecraft orbiting in a plasma environment will attain a static charge. Many Earth orbiting spacecraft, such as the SCATHA mission, have measured this effect.[27] Whipple[28] presents an overview of the natural charging that occurs in the Earth environment. Spacecraft in Earth orbit tend to naturally hold a negative charge, and this charging occurs with a small time constant (on the order

of milliseconds).[29] Garrett and Whittelsey[30] provided an updated survey of spacecraft charging issues in 2000.

If a satellite is to control its charge, it must exchange charge with the plasma environment in some way. One solution involves the use of ion or electron beams. Charging a spacecraft with particle beams has been extensively studied in conjunction with research in both missile defense and ionospheric physics. An overview of beam effects on satellites can be found in Lai[31].

An additional way to create a charge on a spacecraft is through the use of radioactive material. Certain materials undergo β -decay, which involves the release of particle containing two protons. Thus, as these protons are ejected from the material, it tends to gain a negative charge. Linder and Christian describe this process in more detail.[32]

The interaction between the spacecraft and the ambient plasma environment is complex and not completely understood. When a charged body moves through a plasma, it develops a sheath of plasma particles around it. This sheath is not composed of individual particles that travel with the body, but a local, relative density variation between the positive and negative species within the plasma. For more information on the formation and characteristics of this sheath, see Walker[33] or Parker[34].

A charged spacecraft will tend to be discharged by the ambient plasma. While this discharging forces the spacecraft to use power to maintain a charge, the plasma can also be used to help the satellite establish a large charge. This type of charging is similar to the tether current collection scheme proposed by Sanmartin[35]. A more in-depth description of this process is found in Choinière and Gilchrist[36]

and in Chapter 4.

1.4.3 Electromagnetic Propulsion Schemes

Many other propellantless propulsion systems have been proposed. The electrodynamic tether system is closely related to LAOs. Tethers force current through a long conductor.[2] The current in this tether moving with the satellite creates a Lorentz force. By using a current in a wire rather than a space charge on the spacecraft, a tether can produce forces in directions an LAO-capable spacecraft cannot. However, the direction of the tether must be controlled, while the Lorentz force in an LAO is attitude independent.

Tether research is useful to LAO investigations in the area of plasma interaction. Mariani, et al. examine the current collected by the actual in-space deployment of the TSS-1 tether.[37]. Fuhrhop et al. provide a theoretical and computational model of the current collected by a tether in space.[38]

LAO-based propulsion and tethers (along with other propellantless propulsion systems) differ in where they harvest energy from. LAO propulsion does work on a satellite by using the rotation of Earth's magnetic field. If in a perfect vacuum, an LAO system would require only enough power to charge up and discharge the spacecraft. A tether system is essentially a device for converting between electrical energy and kinetic energy using a magnetic field. Solar sails and magnetic sails harvest energy from the sun to perform propellantless maneuvers.[1]

Other studies have proposed various ways to use charged spacecraft and magnetic field interactions for many applications. King et al.[39] and Schaub[40] present the idea of Coulomb spacecraft formations (CSF). Satellites in a CSF

formation are electrostatically charged, and some measure of formation control is provided by the Coulomb forces between the various satellites. The CSF system faces many of the same system architecture challenges as LAO propulsion. However, due to plasma shielding, a CSF is impractical in LEO, while an LAO is more effective in LEO where the magnetic field strength is greater. The use of the Lorentz force for formation flight is discussed in more detail in Chapter 5.

1.4.4 Attitude Control Via the Lorentz Force

Orbit control is not the only use of the Lorentz force for a spacecraft. Attitude actuation is also a possibility by differential charging on the spacecraft body. A number of Russian researchers began studying the effect of the Lorentz force on spacecraft attitude motion in the late 1970s to early 1980s. In 1982, Beletskii[41] examined a spacecraft with an electrified conical shell (designed to protect the satellite from radiation). He used a tilted dipole geomagnetic model. This field produces a uniform precession of the satellite about an axis that lies fixed angle from the axis of Earth's rotation.

In 2002, Tikhonov[42] examined the effect of the Lorentz force on the attitude of a charged spacecraft in an equatorial, circular orbit under the influences of three different magnetic field models: a non-tilted dipole, a tilted dipole, and a quadrupole model. He found that the tilted dipole does not model torques on the satellite well. In fact, the non-tilted dipole may be more accurate for this situation. The quadrupole is significantly better than the either dipole model.

In 2003, Tikhonov[43] examined a satellite with a charged sheet for the purpose of attitude control. The spacecraft is in a near-circular, near-equatorial orbit

(the equatorial assumption can be relaxed). A semipassive stabilizing control is presented for a quadrupole magnetic model.

1.5 Dissertation Contributions and Overview

The main objective of this dissertation is to establish the theoretical basis for orbital maneuvers based on modulating charge on a spacecraft within a planetary magnetosphere, and then validate this theory via simulation of relevant examples motivated by mission applications. In doing so, principles observed in astronomy and planetary science are applied to spacecraft navigation problems. The key contributions of this dissertation are:

- Expressions for the change in orbital energy and angular momentum are developed. These expressions are valid for any magnetic field model or orbit.
- Discovery of new synchronous orbits using the Lorentz force. In particular:
 - A low-Earth, single-orbit repeat groundtrack trajectory, initially shown for polar, circular starting orbits. This orbit is developed for other inclinations and eccentricities, as well as being shown closed-loop stable under a tilted dipole model.
 - Orbits whose perigees are synchronous with the Earth.
 - Sun-synchronous orbits for any inclination, eccentricity, and semimajor axis.
- Enhancements to the gravity-assist maneuver using the Lorentz force, including

- Small changes to the ΔV of a flyby by rotation of the periapsis during the hyperbolic pass.
 - Reversible, temporary capture of spacecraft at the target planet
 - Arbitrary exit asymptote direction using a constant charge-to-mass ratio, allowing for the full range of geometrically possible ΔV values for a given orbit energy and angular momentum.
- A framework for developing bang-off control laws to perform general Lorentz maneuvers in any magnetic field. Specifically, a low-Earth inclination change controller is developed fully, and proved optimal under certain conditions.
 - The use of the Lorentz force to create arbitrarily shaped, planar spacecraft formations. The stability and controllability of such formations are developed.

The six chapters of this dissertation are as follows. Chapter 1 contains the introductory material, including the problem definition, basic orbit dynamics, and a review of relevant research. Chapter 2 explores the creation of new Earth- and Sun-synchronous orbits using the Lorentz force. Spacecraft with a constant charge are examined under a non-tilted dipole magnetic field model. A charge controller is then developed to regain synchronous behavior in the presence of a tilted dipole field. Chapter 3 examines how the Lorentz force can be made to extend the usefulness and flexibility of planetary flyby maneuvers. An algorithm is developed to allow for the temporary capture of a spacecraft at Jupiter, followed by an arbitrary exit direction. Chapter 4 develops a more general LAO control scheme based upon a realistic magnetic field model. A near-term achievable system architecture is presented, and an application is developed based upon an estimate of the system's charge-to-mass ratio. The effect of the Earth's plasmasphere on LAO power con-

sumption is also examined. Chapter 5 discusses the use of the Lorentz force in spacecraft formation flight. Relative orbit dynamics are developed, along with a sample formation maneuver. Finally, Chapter 6 concludes this work and discusses possible avenues of future research in Lorentz augmented orbits.

CHAPTER 2
NEW SYNCHRONOUS ORBITS USING THE GEOMAGNETIC
LORENTZ FORCE

2.1 Introduction

In a repeat groundtrack orbit, the sub-satellite point traces out a recurring pattern on the Earth in some integer number of orbital periods. Traditionally, these orbits are achieved by adjusting the period of a satellite such that it completes an integer number of revolutions in exactly an integer number of sidereal Earth days. Geostationary and geosynchronous orbits are perhaps the most familiar and useful examples. These orbits have a mean motion equal to the spin rate of the Earth. We shall refer to orbits that repeat their groundtrack every orbital period as GT-1 orbits. Thus all GEO orbits are in the GT-1 class. A more general class, the GT- x orbit, repeats its groundtrack every x revolutions. For example, satellites in the GPS constellation are in 12 sidereal hour orbits and can thus be considered GT-2 satellites. Many LEO imaging satellites designed for full-Earth coverage also use repeat-track orbits. Every 16 days, over the course of 233 orbits, Landsat 7 covers the full Earth, making it a GT-233 satellite.[44] Repeat-groundtrack Keplerian orbits are based on the number of Earth days that pass before the ground track is repeated. However, augmenting the orbit with the Lorentz force enables repeat-groundtrack orbits that are not tied to integer multiples of Earth's spin period.

Dedicated weather satellites and both government and commercial communications satellites are just a few of the numerous uses for GT-1 orbits. However GT-1 systems are currently limited to GEO orbits. The altitude of these satellites,

roughly 36000 km, requires high-power communications and impacts the aperture requirements for Earth-imaging satellites. An ideal arrangement would be a GT-1 orbit at a low Earth altitude. This chapter proposes just that: a low Earth, polar GT-1 orbit achieved with LAO propulsion. While such an orbit is not geostationary in the sense of an equatorial GEO satellite, it is geosynchronous. The groundtrack repeats every orbital period.

Using the equations of motion and perturbation equations presented in Chapter 1, we can analyze and characterize these new orbits. Described in Section 2.2 are methods for changing orbital energy, changing orbit angular momentum (both magnitude and direction), and arbitrary control of right ascension and argument of perigee for certain situations. This control allows for the creation of certain new Earth-synchronous orbits.

The scope of this chapter does not include many complexities of the LAO system. The non-tilted dipole geomagnetic field model is used until Section 2.3, when the tilted dipole model is examined. The implementation of an LAO-capable spacecraft is discussed only in Chapter 4, and what follows in this chapter assumes that a required charge on the satellite can be delivered, regardless of plasma environment or power constraints. This chapter focuses on the basic orbital dynamics of an LAO and presents dynamically interesting cases with applications inspired by these results.

2.2 Applications

Using the Lorentz force to achieve a mission objective is sometimes not an intuitive exercise. A charged spacecraft cannot control the direction of the force, only

magnitude and perhaps the sign, depending on the implementation architecture. The force is also perpendicular to the field-fixed velocity of the spacecraft. Were the magnetic field not rotating, no energy could be added to an LAO; but with the rotating field, the energy and angular momentum of the orbit can be changed in most cases. Also, with appropriate control of the charge on the satellite, controlling energy and momentum allows for regulation of most of the orbital elements of the spacecraft. Two specific cases are developed here: the polar circular orbit and the general equatorial orbit, both in a non-tilted dipole field. Additionally, Earth oblateness effects are examined.

2.2.1 Polar Circular Orbit, Non-tilted Dipole Field

We apply the general energy and momentum relationships in Eqs. 1.27 and 1.30 to two specific cases to develop some simple and interesting results.

Analytical Results

First, we examine a polar, circular orbit in a non-tilted dipole magnetic field. In this case, the following expressions hold:

$$\mathbf{v} \cdot \mathbf{r} = 0; \quad \mathbf{B} \cdot \mathbf{r} = 2 \frac{B_0}{r^2} \sin u; \quad \mathbf{v} \cdot \hat{\mathbf{n}} = v \cos u; \quad v = \sqrt{\frac{\mu}{r}} \quad (2.1)$$

where r is the radius of the orbit, and u is the argument of latitude of the satellite. The argument of latitude is the angular position of the satellite around the orbit measured from the right ascension of the vehicle in the equatorial plane. Substituting the equalities in Eq. 2.1, Eq. 1.27 becomes

$$\dot{E} = 2 \frac{q}{m} \omega_E B_0 \sqrt{\mu} r^{-5/2} \sin u \cos u \quad (2.2)$$

The expression in Eq. 2.2 is an odd, periodic function of u and, thus, contributes no secular change to the energy of the orbit. However, the radius of the orbit oscillates with a frequency of twice per orbit. Expressing the radius of the circular orbit as a function of energy, and using Eq. 2.2, gives an expression for the time rate of change of the radius of the orbit:

$$\dot{r} = 4 \frac{q}{m} \omega_E \frac{B_0}{\sqrt{\mu}} r^{-1/2} \sin u \cos u \quad (2.3)$$

For constant $\frac{q}{m}$, Eq. 2.3 is periodic over an orbit. The radial velocity (and thus eccentricity) remains small for a constant $\frac{q}{m}$, keeping the assumptions of a Keplerian, polar, circular orbit valid. The simulation results shown below back up this assumption, showing that deviations in eccentricity and inclination remain small. However, if we choose to control the charge as a function of the argument of latitude, a secular change in the radius (and eccentricity) of the orbit can be obtained.

Similarly, the angular momentum rate of a circular polar LAO is examined with Eq. 1.30, with an orthogonal coordinate system having the x -direction along the line of nodes, the y -direction aligned with the north pole, and the z -direction necessarily along the orbit angular momentum vector. With this coordinate system, the properties of a polar, circular orbit, and Eq. 1.30, the derivative of angular momentum becomes

$$\dot{\mathbf{h}} = 2 \frac{q}{m} \frac{B_0}{r^2} \begin{bmatrix} -v \sin^2 u \\ v \sin u \cos u \\ r \omega_E \sin u \cos u \end{bmatrix} \quad (2.4)$$

Equation 2.4 represents the time rate of change of the angular momentum vector due to the Lorentz force, for a circular, polar LAO.

We use the vector derivative in Eq. 2.4 to define several scalar derivatives

of interest, including the time rates of change of the inclination angle, the right ascension angle, and the magnitude of the angular momentum. First, the derivative of the scalar angular momentum magnitude is given by

$$\dot{h} = 2 \frac{q}{m} \frac{B_0}{r} \omega_E \sin u \cos u \quad (2.5)$$

Thus, the magnitude of the angular momentum vector changes in a purely periodic manner under a constant charge.

The inclination angle i is defined in terms of the angular momentum vector \mathbf{h} by

$$\hat{\mathbf{n}} \cdot \mathbf{h} = h \cos i \quad (2.6)$$

Differentiating Eq. 2.6 to find the time rate of change of i gives

$$\frac{di}{dt} = \frac{-2 \frac{q}{m} \frac{B_0}{r^2} \sin u \cos u [v - r \omega_E \cos i]}{rv \sin i} \quad (2.7)$$

where the notation $\frac{di}{dt}$ is used for clarity. Again, for constant charge, Eq. 2.7 is nonsecular, oscillating at a frequency of twice per orbit.

The line of nodes vector $\mathbf{\Omega}$ is defined by

$$\mathbf{\Omega} = \hat{\mathbf{n}} \times \mathbf{h} \quad (2.8)$$

and extends from the origin of the coordinate system through the point where the satellite ascends through the equatorial plane. Differentiating Eq. 2.8 gives

$$\dot{\mathbf{\Omega}} = \hat{\mathbf{n}} \times \dot{\mathbf{h}} \quad (2.9)$$

which simplifies to

$$\dot{\mathbf{\Omega}} = -\frac{2qB_0}{mr^2} v_c \sin^2 u \begin{bmatrix} 0 \\ 0 \\ 1 \end{bmatrix} + \frac{2q\omega_E B_0}{mr} \sin u \cos u \begin{bmatrix} 1 \\ 0 \\ 0 \end{bmatrix} \quad (2.10)$$

There are two terms in right hand side of Eq. 2.10: one along the direction of the node vector, and one normal to it. The length of the node vector is irrelevant here. The term normal to the node vector is more interesting. It is in the equatorial plane, and thus represents a change in the right ascension angle Ω . This term is an even function and produces a secular change. We can substitute into Eq. 2.10 the fact that the magnitude of the velocity in the circular orbit, v , is given by ri . Thus the normal component of the vector right ascension rate is

$$\dot{\Omega}_n = -\frac{2qB_0}{mr} \sin^2 ui \quad (2.11)$$

We can relate Eq. 2.11 to the actual angular right ascension rate, $\dot{\Omega}$, by

$$\dot{\Omega} = \frac{\dot{\Omega}_n}{\|\mathbf{\Omega}\|} \quad (2.12)$$

In the polar case, the magnitude of the node vector is simply the magnitude of the angular momentum vector, or

$$\|\mathbf{\Omega}\| = \|\mathbf{h}\| = r\sqrt{\frac{\mu}{r}} \quad (2.13)$$

because the angular momentum is perpendicular to the north direction. Equation 2.12 becomes

$$\dot{\Omega} = -2\frac{q}{m} \frac{B_0}{r^2} \sqrt{\frac{r}{\mu}} \sin^2 ui \quad (2.14)$$

Equation 2.14 represents the rate of change in right ascension angle as a function of argument of latitude. Equation 2.14 is an even, secular function. The RAAN of the orbit changes of the course of one orbit.

We can determine an average change in right ascension per orbit by integrating Eq. 2.14 around one complete orbit. The change in right ascension per orbit ($\Delta\Omega$) is given by

$$\Delta\Omega = -2\pi \frac{q}{m} \frac{B_0}{r^2} \sqrt{\frac{r}{\mu}} \quad (2.15)$$

Thus, for the circular polar orbit, non-tilted dipole case, we can set an arbitrary change in right ascension per orbit. Defining the average time derivative of right ascension as $\dot{\Omega}_{avg}$, equal to Eq. 2.15 divided by the orbital period, and inverting the result gives the following simple relationship between the charge-to-mass ratio $\frac{q}{m}$ and the average right ascension rate $\dot{\Omega}_{avg}$, circular orbit radius r , and magnetic field strength B_0 :

$$\frac{q}{m} = -\frac{\dot{\Omega}_{avg} r^3}{B_0} \quad (2.16)$$

We can now calculate the necessary charge-to-mass ratio for any desired right ascension rate.

Changing the right ascension of a polar orbit essentially amounts to changing longitude on the groundtrack of the satellite (see Fig. 2.1). Arbitrary right ascen-

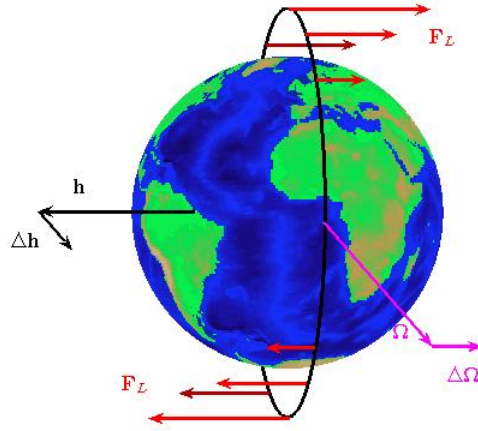


Figure 2.1: Graphical representation of the vectors involved in an LAO GT-1 orbit.

sion control can greatly increase the efficiency of a polar LEO imaging satellite. If full charge control is possible (both positive and negative charges) then the satellite can acquire a target faster, and then stay in the neighborhood of the target

longer. In fact, if an average right ascension rate equal to the rate of Earth's rotation is acquired, then a satellite can have a single-orbit repeat-groundtrack. The satellite would pass over exactly the same points on the Earth every orbit. Thus, the orbit becomes a LEO GT-1 orbit. This groundtrack would allow a satellite to pass over an imaging target every 90 minutes rather than at most twice a day for an uncontrolled LEO polar satellite.

Solving for the required charge-to-mass ratio for an LAO GT-1 yields

$$\left(\frac{q}{m}\right)_{GT-1} = -\frac{\omega_E r^3}{B_0} \quad (2.17)$$

When evaluated for a circular orbit with 400km altitude, Eq. 2.17 reveals that a $\frac{q}{m}$ of 2.831 C/kg is required for geosynchronous behavior.

Another possible application is a sun-synchronous LEO polar orbit at any altitude. The sun-synchronous condition is a right ascension rate of $\dot{\Omega}_{ss} = 2\pi$ rad/year. This rate yields a charge-to-mass ratio for maintaining a sun-synchronous orbit of

$$\left(\frac{q}{m}\right)_{ss} = -\frac{\dot{\Omega}_{ss} r_0^3}{B_0} \quad (2.18)$$

For example, a 400km orbit requires a ratio 0.0078 C/kg for sun synchronicity.

The non-periodic change in right ascension persists for orbits that are not necessarily polar or circular. By extending the process used to derive the polar case to a general orbit (still assuming a non-tilted dipole field), an expression analogous to Eq. 2.16 is found for a general orbit:

$$\frac{q}{m} = \frac{\dot{\Omega}_{avg} a^3}{B_0} (1 - e^2)^{3/2} \frac{1}{\omega_E \sqrt{\frac{a^3}{\mu}} (1 - e^2)^2 \cos i \frac{e^2 - [(1 - e^2)^{1/2} - 1]^2 \cos 2\omega}{e^2} - 1} \quad (2.19)$$

Equation 2.19 is valid for any elliptical orbit under the influence of a non-tilted dipole.

Alternate Derivation of GT-1 Behavior

The GT-1 behavior derived above can also be found using the Hamiltonian formulation of the LAO problem found in Section 1.3.2. The magnetic vector potential for a dipole field is

$$\mathbf{A} = \frac{B_0}{r^2} (\hat{\mathbf{N}} \times \hat{\mathbf{r}}) \quad (2.20)$$

For a non-tilted dipole, $\hat{\mathbf{N}}$ is aligned with $\hat{\mathbf{n}}$, giving $\hat{\mathbf{N}} = \cos \phi \hat{\mathbf{r}} - \sin \phi \hat{\phi}$. Substituting into Eq. 2.20 gives a vector potential of

$$\mathbf{A} = \frac{B_0}{r^2} \begin{bmatrix} 0 \\ 0 \\ \sin \phi \end{bmatrix} \quad (2.21)$$

Using this potential in the Hamiltonian of Eq. 1.22 in a coordinate frame rotating with the planet gives:

$$\begin{aligned} H = & \frac{1}{2m}(p_r)^2 + \frac{1}{2mr^2}(p_\phi)^2 + \frac{1}{2mr^2 \sin^2 \phi} (p_\theta - mr^2 \omega_E \sin^2 \phi - q \frac{B_0}{r} \sin^2 \phi)^2 \\ & + m\Phi_{gr} - \frac{1}{2}mr^2 \omega_E^2 \sin^2 \phi \end{aligned} \quad (2.22)$$

with canonical variables r , ϕ , and θ and conjugate momenta

$$p_r = m\dot{r} \quad (2.23)$$

$$p_\theta = mr^2 \sin^2 \phi (\dot{\theta} + \omega_E) + q \frac{B_0}{r} \sin^2 \phi \quad (2.24)$$

$$p_\phi = mr^2 \dot{\phi} \quad (2.25)$$

Using Hamilton's equation to get the rate of longitudinal movement gives

$$\dot{\theta} = \frac{\partial H}{\partial p_\theta} = \frac{p_\theta}{mr^2 \sin^2 \phi} - \omega_E - \frac{q}{m} \frac{B_0}{r^3} \quad (2.26)$$

For a polar orbiting satellite, p_θ is zero. For GT-1 behavior, $\dot{\theta}$ should be equal to zero (in the rotating system). Setting $\dot{\theta}$ to zero and solving for $\frac{q}{m}$ gives

$$\left(\frac{q}{m}\right)_{GT-1} = -\frac{\omega_E r^3}{B_0} \quad (2.27)$$

which exactly recovers Eq. 2.17.

Numerical Simulation

A numerical simulation is developed to test several of the previous analytical results. The simulation is a Runge-Kutta (4,5) integration of the sixth-order system defined by Eqs. 1.11-1.13, performed by Matlab. The simulation is valid for any orbit for a charged satellite in a non-tilted dipole field. Table 2.1 shows the set of physical parameters common to all simulations.

Table 2.1: Physical parameters common to all simulations.

Parameter	Value
ω_E	7.272e-5 rad/s
μ	3.986e14 m ³ /s ²
B_0	-8.000e15 Wb-m

The polar, circular orbit is integrated from the initial conditions in Table 2.2. The charge-to-mass ratio of 2.83 c/KG is chosen based on Eq. 2.17. Figure 2.2 shows the resulting orbital path. This path is plotted in a frame that rotates with the Earth so as to highlight the GT-1 nature of the orbit. The orbit is shown to scale with the image of the Earth. Figure 2.2 shows a slight deviation from a perfect GT-1 orbit. This discrepancy is explained by Fig. 2.3. This figure compares the forces acting on the satellite over one orbital period. The magnitudes of both gravity and the Lorentz force are shown. In this GT-1 polar scenario, the Lorentz force is quite significant with respect to gravity, which causes large orbital element changes, violating the osculating-element assumption. A large Lorentz force causes

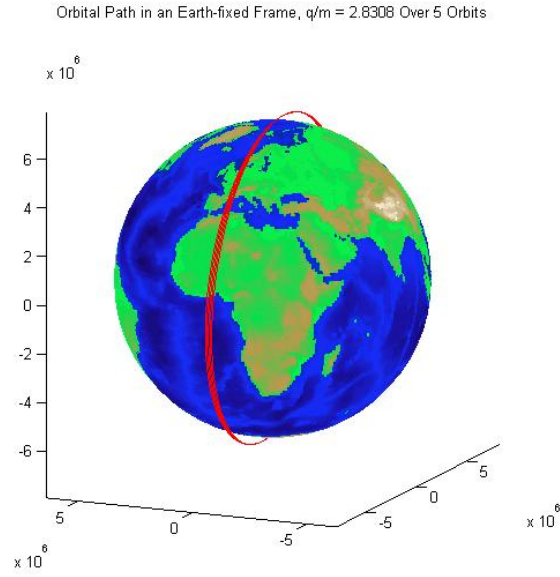


Figure 2.2: Track of a GT-1 LAO orbit in a frame rotating with Earth with $\frac{q}{m} = 2.83$ C/kg.

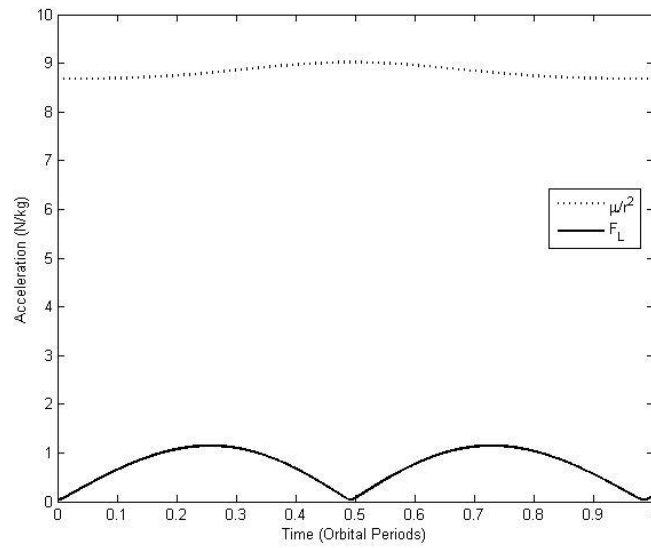


Figure 2.3: Comparison of gravitational and Lorentz acceleration magnitudes for a GT-1 LAO orbit with $\frac{q}{m} = 2.83$ C/kg.

the orbital eccentricity to be non-zero, creates wobbles in the inclination, and keeps the orbital speed from being constant. These perturbations on the orbit cause slight inaccuracies in the expressions derived in Section 2.2.1 related to a polar circular orbit.

Table 2.2: Initial conditions for polar, circular orbit.

Property	Value
Altitude	400 km
$\frac{q}{m}$	2.831 C/kg
Integration Time	5 orbits

However, the small difference in calculated and desired right ascension angles is due only to wind up of small errors in predicted right ascension rate over time. The top plot of Fig. 2.4 shows both the numerically calculated and the analytically derived right ascension angle rates. The analytical results are based on the expression in Eq. 2.14; the numerical result is based upon changes in the angular momentum vector of the orbit determined from the state of the system at any given time. As expected, the right ascension rate is zero as the satellite crosses the equator, and large and positive as it crosses the poles. The average values of the curves in Fig. 2.4 is greater than zero, causing a secular increase in the right ascension of the orbit. These two curves match nearly exactly, with small, but persistent, errors. The rate error is shown in the bottom plot of Fig. 2.4. The size of the errors is an order of magnitude smaller than the rates. In practice, closed-loop control of the charge might be used to trim the errors that arise due to unmodeled dynamics in the open-loop system. The closed-loop case is addressed later in Section 2.3.3.

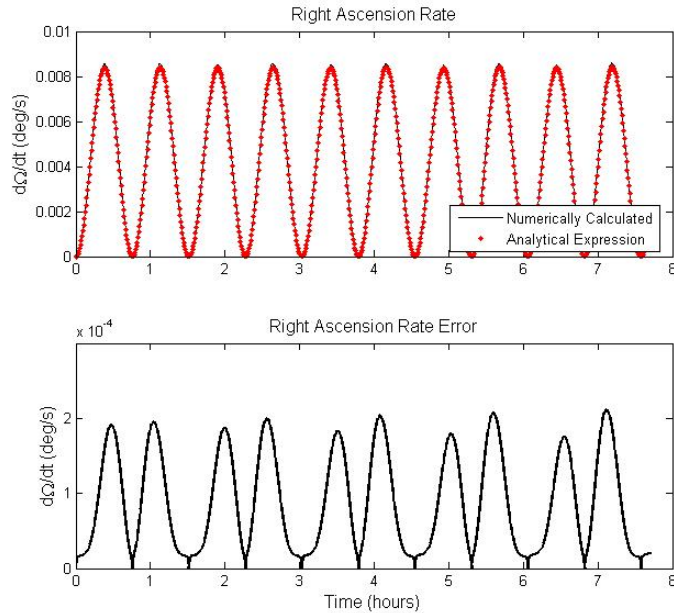


Figure 2.4: Time rate of change in right ascension for a GT-1 LAO orbit with $\frac{q}{m} = 2.83$ C/kg. The top plot shows both analytical and numerical calculations of the right ascension. The bottom plot shows the error between these two curves.

Finally, Fig. 2.5 shows the time rate of change of orbital energy throughout the simulation. The solid line represents the numerically calculated energy rate based on the state vector at each time, and the dotted line represents the derived expression shown in Eq. 2.2. These two curves match closely. However, the energy rate is centered around zero, and thus there is no secular change in the orbital energy.

2.2.2 Equatorial Orbit, Non-tilted Dipole Field

A second simple case to consider is an equatorial orbit in a non-tilted dipole field. The true equator and the magnetic equator are aligned in this situation, and

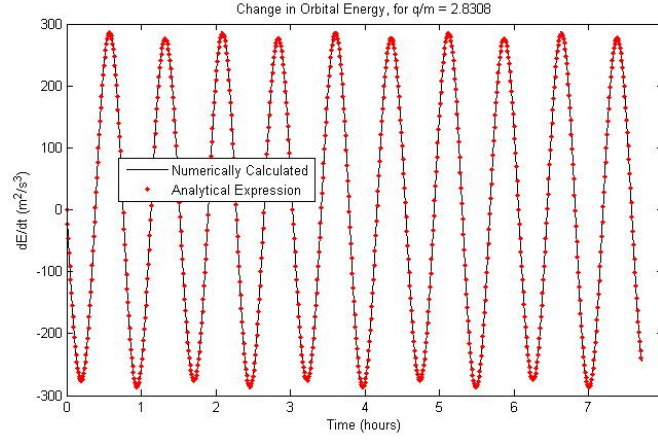


Figure 2.5: Time rate of change of orbital energy for a GT-1 LAO orbit with $\frac{q}{m} = 2.83$ C/kg.

magnetic field is perpendicular to these planes. The eccentricity can be non-zero in this case.

Analytical Results

In the equatorial, eccentric orbit case, the following relationships hold:

$$\mathbf{v} \cdot \hat{\mathbf{n}} = 0; \mathbf{B} \cdot \hat{\mathbf{n}} = -\frac{B_0}{r^3}; \mathbf{r} \cdot \mathbf{v} = \sqrt{\mu a(1 - e^2)} \frac{e \sin \nu}{1 + e \cos \nu} \quad (2.28)$$

where a is the orbit semimajor axis, e is the orbital eccentricity, and ν is the true anomaly. With Eq. 2.28, and the standard conic section equation for an elliptical orbit,

$$r = \frac{a(1 - e^2)}{1 + e \cos \nu} \quad (2.29)$$

Eq. 1.27 becomes

$$\dot{E} = \frac{q}{m} \omega_E B_0 \sqrt{\mu} [a(1 - e^2)]^{-5/2} e \sin \nu (1 + e \cos \nu)^2 \quad (2.30)$$

Note the dependence on the eccentricity e . The Lorentz force can not add energy to a circular, equatorial orbit. Equation 2.30 leads to a time rate of change of

semimajor axis of

$$\dot{a} = 2\frac{q}{m}ea^2\omega_E\frac{B_0}{\sqrt{\mu}}[a(1-e^2)]^{-5/2}\sin\nu(1+e\cos\nu)^2 \quad (2.31)$$

Again, the rate in Eq. 2.31 is nonsecular, but with proper modulation of $\frac{q}{m}$, the size of the equatorial orbit can be controlled using the Lorentz force.

Using the specifics of an equatorial orbit in Eq. 1.30 gives a time rate of change of vector angular momentum of

$$\dot{\mathbf{h}} = -\frac{q}{m}(\mathbf{r} \cdot \mathbf{v})\frac{B_0}{r^3}\hat{\mathbf{h}} \quad (2.32)$$

where $\hat{\mathbf{h}}$ is a unit vector in the \mathbf{h} direction. As the rate in Eq. 2.32 only has a component in the direction of \mathbf{h} , it represents only a change in the scalar magnitude of \mathbf{h} . This scalar momentum change is expressed as

$$\dot{h} = \frac{q}{m}B_0\sqrt{\mu}[a(1-e^2)]^{-5/2}e\sin\nu(1+e\cos\nu)^2 \quad (2.33)$$

which is another periodic function with no secular terms. Here, the direction of h cannot be controlled, which means the inclination and right ascension angle cannot be changed.

Following Burns[10] and using Eqs. 2.30 and 2.33, an expression for the time rate of change of orbital eccentricity under the Lorentz force in a equatorial orbit is

$$\dot{e} = -\frac{q}{m}B_0\frac{\sin\nu(1+e\cos\nu)^2}{[a(1-e^2)]^{3/2}}\left[\frac{1}{a^{3/2}(1-e^2)^{1/2}} - \frac{\omega_E}{\sqrt{\mu}}\right] \quad (2.34)$$

which is periodic in true anomaly. If one starts with an initially circular orbit, the eccentricity of the orbit should be changed to facilitate the control of energy.

Also from Burns[10], we develop an expression for the argument of perigee rate using Eqs. 2.30 and 2.33. Simplification gives

$$\dot{\omega} = \frac{q}{m}B_0\left[\frac{2}{[a(1-e^2)]^{3/2}} + \frac{2e\cos\nu}{[a(1-e^2)]^{3/2}} + \frac{\cos\nu}{a^{3/2}e(1-e^2)^{1/2}} - \frac{\omega_E\cos\nu}{e\sqrt{\mu}}\right]\dot{\nu} \quad (2.35)$$

where the standard time rate of change of true anomaly for a Keplerian orbit has been used. The first term in brackets of Eq. 2.35 gives rise to a secular change in the argument of perigee for a constant charge-to-mass ratio. This secular perigee change has many interesting, if somewhat esoteric, applications. Perigee control allows for the cancelation of various natural perturbations on the argument of perigee, such as J2 effects and lunar and solar tides. Another use may be to create a Molniya-type orbit at zero inclination (and most likely other inclinations). Building on the same ideas as the GT-1 LAO orbits discussed previously, perigee control also allows for matching Earth's rotation rate. The line of apsides of such a synchronous orbit would remain at a constant longitude on Earth's surface. Thus, LAO-based propulsion creates possibilities for other kinds of synchronous orbits rather than just GT- x orbits.

To evaluate this concept of precessing the line of apsides, we seek an expression for the $\frac{q}{m}$ necessary to generate a certain average perigee rate. Integrating Eq. 2.35 around one orbit gives an expression for the change in argument of perigee per orbit $\Delta\omega$:

$$\Delta\omega = \frac{4\pi \frac{q}{m} B_0}{\sqrt{\mu} [a(1 - e^2)]^{3/2}} \quad (2.36)$$

For a certain desired rate of change in the argument of perigee $\dot{\omega}_{des}$ we require that $\Delta\omega/\Delta t = \dot{\omega}_{des}$, where we set Δt to be one orbital period. Setting the resulting expression for $\Delta\omega$ equal to Eq. 2.36 and solving for $\frac{q}{m}$ gives a required charge-to-mass ratio for some desired rate of perigee change:

$$\frac{q}{m} = \frac{\dot{\omega}_{des} a^3 (1 - e^2)^{3/2}}{2B_0} \quad (2.37)$$

Equation 2.37 has similar dependencies as Eq. 2.16, the charge-to-mass ratio required for a particular right ascension rate for a polar circle. However, in the equatorial case, the eccentricity plays an important role in the magnitude of charge

required. A higher eccentricity corresponds to a higher velocity at perigee for a given orbit size, which makes a more effective use of the Lorentz force, allowing for a smaller charge-to-mass ratio. Equation 2.37 applies for any desired rate of change for argument of perigee, including mitigating oblateness and third-body effects as well as introducing synchronous behavior. However, larger rates introduce inaccuracy in the $\frac{q}{m}$ predicted by this osculating-elements approach. The derivation of Eq. 2.37 assumes that all the other orbital elements are changing slowly or are not explicit functions of ν , and this may not be the case with a large charge-to-mass ratio.

The secular change in argument of perigee under a constant charge also arises in non-equatorial orbits. Following the same method as for the equatorial case, but generalized for any elliptical orbit, yields an expression for the charge-to-mass ratio required for a desired perigee rate:

$$\frac{q}{m} = \frac{\dot{\omega}_{des} a^3 (1 - e^2)^{3/2}}{B_0 \cos i} \left[3 - \omega_E \sqrt{\frac{a^3}{\mu}} (1 - e^2)^2 \cos i \frac{e^2 - [(1 - e^2)^{1/2} - 1]^2 \cos 2\omega}{e^2} \right]^{-1} \quad (2.38)$$

A subtlety in the derivation of Eq. 2.38 arises from the coupled changes in right ascension and argument of perigee in an inclined orbit, hence the similarities between Eq. 2.38 and Eq. 2.19.

Equation 2.38 gives the time rate of change of perigee relative to an inertial coordinate system. This rate is the superposition of two different rates: the rate of change of argument of perigee within the orbit plane, and the change in perigee due to the fact that the right ascension, and thus orbital plane itself, is changing. In order to create the ω -synchronous orbit, the rate of in-plane perigee change must be equal to the rotation rate of the Earth. Subtracting off the rates due to

right ascension rate of change gives

$$\frac{q}{m} = \frac{\omega_E a^3 (1 - e^2)^{3/2}}{2B_0 \cos i} \quad (2.39)$$

which differs only by a factor of $1/\cos i$ from Eq. 2.37. Again, Eq. 2.39 is only valid for situations where desired rate of perigee change is based on a relationship with the rotating Earth, rather than some absolute inertial rate.

Numerical Simulation

The equatorial, eccentric, constant charge simulation is initialized with the values shown in Table 2.3, using the same model as in the case of the polar orbit. The

Table 2.3: Initial conditions for equatorial, constant charge integration.

Property	Value
Perigee Altitude	400 km
Apogee Altitude	1500 km
Eccentricity	0.075
Semimajor Axis	7328 km
$\frac{q}{m}$	-1.774 C/kg
Integration Time	1 day

chosen value of $\frac{q}{m}$ is designed to produce an Earth-synchronous motion of the perigee of the orbit. The value is calculated from Eq. 2.37 with a desired rotation rate designed to match the Earth's rotation, or $\dot{\omega}_{des} = \omega_E$.

Figure 2.6 shows the orbital path of the satellite over one day. Again, the orbit is to scale with the depiction of the Earth as viewed from above the North Pole. The orbital path is shown in a coordinate system rotating with the Earth.

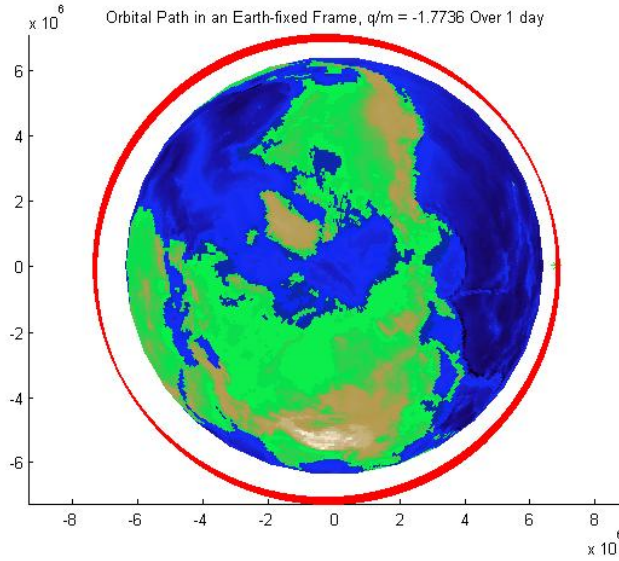


Figure 2.6: Earth-fixed orbital path of an equatorial, constant charge LAO satellite with $\frac{q}{m} = -1.77$ C/kg, calculated for synchronous perigee movement.

The rotating frame view in Fig. 2.6 shows that the charge-to-mass ratio used in the simulation was not large enough to perfectly cancel the Earth's rotation with perigee motion. If the correct charge were used, the rotating frame view would show only a single curve. The top plot of Fig. 2.7 shows the numerically calculated and analytically derived arguments of perigee for this case. The numerical values are represented by the solid line. The dotted line represents the analytical values, calculated by numerically integrating Eq. 2.35. While these two curves match quite precisely, we see that the perigee angle does not reach 360° after one day as intended. Fig. 2.7 gives confidence in the result for time rate of change of perigee expressed in Eq. 2.35, but shows that accuracy is lost in integrating this data to obtain Eq. 2.37. The perigee error, the difference between the numerical and analytical curves, is shown in the bottom plot of Fig. 2.7. The error is

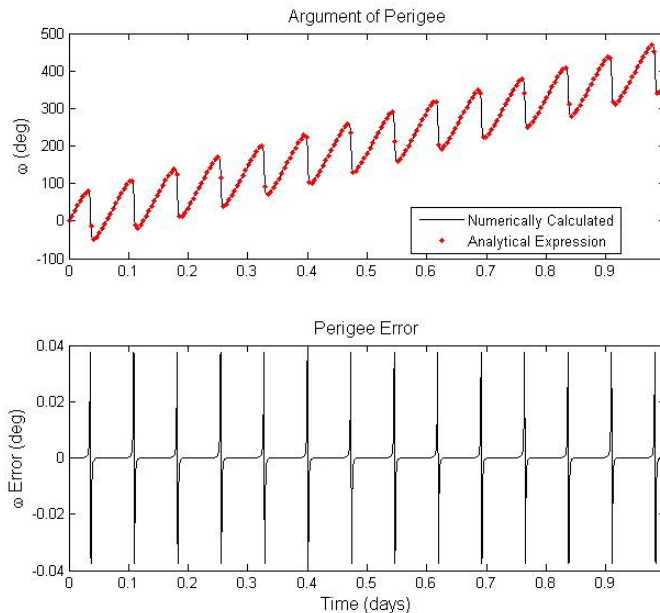


Figure 2.7: Argument of perigee angle of an equatorial, constant charge LAO satellite with $\frac{q}{m} = -1.77$ C/kg. The top plot shows both analytical and numerical calculations of the argument of perigee. The bottom plot shows the error between these two curves.

significantly smaller than the perigee values. In the integration of Eq. 2.35, we assumed that the semimajor axis and eccentricity were changing slowly enough to be independent of true anomaly. The charge-to-mass ratios are large enough in this case to make that a poor assumption. However, for smaller desired perigee rate, like mitigating J2 effects, Eq. 2.37 is quite accurate. Creating the Earth-synchronous effect is certainly possible; it just requires a larger $\frac{q}{m}$ than predicted. Creating a closed-loop control system to adjust $\frac{q}{m}$ can account for this variation, in addition to correcting for imperfections in the magnetic field model, plasma variations, etc. Equation 2.37 represents a starting point for system design and closed-loop control.

The results demonstrate that a constant charge, equatorial LAO satellite can

have an arbitrary time rate of change of argument of perigee. The required charge-to-mass ratio for a desired rate depends solely on the initial orbit configuration and the magnitude of the desired change. The orbital energy and eccentricity also change in a predictable manner, but with no secular variations.

The simulations, both in this section and previously in Section 2.2.1 have shown excellent agreement between the derived equations of motion and the analytical expressions for the orbital changes in an LAO. We see that useful and desirable changes can be made to orbits using this system. Although only simulations of polar and equatorial orbits are presented here, an arbitrarily inclined orbit will just combine the properties of these two results in some way. Furthermore, the approximation of osculating elements yields convenient expressions that provide insight into the behaviors for only small inaccuracy.

2.2.3 Mitigation of Earth Oblateness Effects

The non-sphericity of the Earth causes secular changes in both the right ascension and argument of perigee of a spacecraft, herein referred to as J2 effects.[44] The generally accepted secular time rates of change due to J2 are

$$\dot{\Omega}_{J_2} = -3/2 \frac{J_2 R_E^2 \sqrt{\mu}}{a^{7/2}} \frac{\cos i}{(1 - e^2)^2} \quad (2.40)$$

$$\dot{\omega}_{J_2} = 3/4 \frac{J_2 R_E^2 \sqrt{\mu}}{a^{7/2}} \frac{4 - 5 \sin^2 i}{(1 - e^2)^2} \quad (2.41)$$

It is trivial to use Lorentz propulsion to cancel the effect of J2 on either the right ascension angle or the argument of perigee. The rate calculated with Eq. 2.40 or Eq. 2.41 can simply be substituted into Eq. 2.19 or Eq. 2.38, respectively. For example, in an equatorial orbit with perigee at 400 km altitude and apogee at

1500 km, J2 causes the argument of perigee to change by about 12.4°/day. The charge-to-mass ratio required to overcome this perturbation is about 0.042 C/kg.

There exist orbits where a constant charge LAO can cancel the secular changes in both Ω and ω . These orbits can only exist below the J2 critical angle of $i \approx 63.4^\circ$ or above the critical solution of $i \approx 116.6^\circ$. Additionally, the effect of the Lorentz force must be equivalent to the J2 effects in both the right ascension and the argument of perigee. This condition is true when the orbit in question satisfies the following expression:

$$\frac{3 - K}{1 - K} = \frac{4 - 5\sin^2 i}{2\cos^2 i} \quad (2.42)$$

where K is given by

$$K = \omega_E \sqrt{\frac{a^3}{\mu}} (1 - e^2)^2 \cos i \frac{e^2 - [(1 - e^2)^{1/2} - 1]^2 \cos 2\omega}{e^2} \quad (2.43)$$

While Eq. 2.42 does not easily yield simple relationships among the orbital elements, a minimum semimajor axis for this condition can be found. Under the most optimistic assumptions, namely $e = 0$, the expression in Eq. 2.42 can be satisfied only if the polynomial

$$3 \frac{w_E}{n} \cos^3 i + \cos^2 i - \frac{w_E}{n} \cos i + 1 = 0 \quad (2.44)$$

where n is the mean motion, has a valid solution. These solutions exist only when $w_E/n > 1$. Thus the semimajor axis must exceed GEO altitude in order to fully cancel J2 effects with a constant charge. At these altitudes, the J2 and LAO effects would generally not be the dominant perturbative forces on the satellite.

2.2.4 Tether/LAO Comparison for GT-1 Behavior

Electrodynamic tethers are an alternate propellantless electromagnetic propulsion system. Under certain tether dynamics assumptions, a tether system can outperform an LAO system for some applications. Here, we discuss the use of a tether to produce the LAO GT-1 synchronous orbits developed in Section 2.2.1.

In order for a tether to show polar GT-1 behavior, the tether current (and tether) must be in the along-track direction of the satellite. Although the flexible-body dynamics of a tether along the velocity direction of the spacecraft are non-trivial, here only the electrodynamic considerations are addressed. With an along-track electrodynamic tether, the Lorentz force experienced by the tether is equivalent to the Lorentz force on an LAO-capable satellite. These two terms can be equated as

$$qv \times \mathbf{B} = L\mathbf{J} \times \mathbf{B} \quad (2.45)$$

where the left side of the equation represents an LAO, and the right a tether, with L being the length of the tether and \mathbf{J} the current through it. As the tether current, \mathbf{J} , is in the same direction as the LAO satellite velocity, it follows that

$$qv = LJ \quad (2.46)$$

Comparing the relevant accelerations gives[45]

$$\frac{q}{m}v = \frac{LI}{m + \lambda L} \quad (2.47)$$

where λ is the mass per unit length of the tether and I is the current through the tether. Solving for the length of tether required to approximate an LAO satellite of charge q and mass m gives

$$L = \frac{qv}{I - \frac{q}{m}v\lambda} \quad (2.48)$$

As the tether length cannot be negative, the denominator of this equation must be positive, giving rise to a minimum required tether current of

$$I = \frac{q}{m}v\lambda \quad (2.49)$$

For a polar GT-1 LAO satellite at an altitude of 400 km with a charge to mass ratio of 2.83 C/kg, and the aluminum tether presented in Forward, et al.[45], the absolute minimum current required for a tether to reproduce GT-1 behavior is 43.4 A. However, at this current an infinitely long tether is required. For a more reasonable tether length of 20 km and a spacecraft base mass of 10 kg, a 55 A current is required.

One slight correction to the above analysis is the self capacitance of the tether. As a voltage is applied to the long wire, it builds up a charge, causing it to act like an LAO spacecraft. Using $4\pi\epsilon_0L$ as the capacitance of a wire, a correction to the current limit given in Eq. 2.49 is applied as

$$I = \frac{q}{m}v\lambda - 4\pi\epsilon_0V_t \quad (2.50)$$

where V_t is the tether potential. The resistance of the tether is relatively small, creating driving voltages on the order of 1 to 100 kV. These voltages reduce the minimum current of Eq. 2.49 by only 0.1 to 10 μ A.

2.3 Effects of a Tilted Dipole Magnetic Field

The previous analysis assumes the geomagnetic field to be a dipole whose magnetic north pole is aligned with the Earth's geographic north pole. While this assumption allows for several clean analytical results to be calculated, a more accurate model of the geomagnetic field is a dipole field whose north pole axis is tilted with respect

to true north. The actual geomagnetic north pole sits in northern Canada, tilted roughly 10° from geographic north.

2.3.1 Tilted Dipole and GT-1 Behavior

Using the tilted dipole model described in Section 1.2, Eq. 1.27, yields a new energy rate of change relationship based on a tilted dipole:

$$\begin{aligned} \dot{E} = & \frac{q}{m} \omega_E B_0 \sqrt{\mu} \frac{[1 + e \cos(u - \omega)]^2}{[a(1 - e^2)]^{5/2}} \left\langle 2 \sin i (\cos u + e \cos \omega) \right. \\ & \times \{ \cos(\Omega_m - \Omega) \sin \alpha \cos u + \sin(\Omega_m - \Omega) \cos i \sin \alpha \sin u + \sin i \cos \alpha \sin u \} \\ & - e \sin(u - \omega) \left[3 \sin u \sin i \{ \cos(\Omega_m - \Omega) \sin \alpha \cos u \right. \\ & \left. \left. + \sin(\Omega_m - \Omega) \cos i \sin \alpha \sin u + \sin i \cos \alpha \sin u \} - \cos \alpha \right] \right\rangle \quad (2.51) \end{aligned}$$

where, again, α represents the angle between the magnetic north pole and geographic north pole, and Ω_m represents the longitude of the magnetic north as measured from the inertial x -axis. Equation 2.51 is for a general elliptical orbit in a dipole field with any tilt. Equation 2.51 includes the non-tilted dipole case and encompasses the expressions in Eqs. 2.2 and 2.30. A similar expression can be derived for the angular momentum rate, which is not presented here for the sake of brevity. However, this angular momentum expression can be used to derive a relationship for the time rate of change of right ascension angle under a tilted dipole field, given by

$$\begin{aligned} \dot{\Omega} = & \frac{q}{m} \frac{B_0}{\sin i} \frac{[1 + e \cos(u - \omega)]^2}{[a(1 - e^2)]^3} \left\{ \cos \phi_m [-2 \sin u - 2e \sin \omega - 3e \sin(u - \omega) \cos u] \right. \\ & + e \sin(u - \omega) [\sin \alpha \cos(\Omega_m - \Omega)] \\ & \left. - \frac{2\omega_E}{\sqrt{\mu}} \frac{[a(1 - e^2)]^{3/2}}{[1 + e \cos(u - \omega)]} \cos \phi_m \cos i \sin u \right\} \quad (2.52) \end{aligned}$$

where ϕ_m is the satellite's magnetic colatitude:

$$\begin{aligned} \cos \phi_m = & \cos(\Omega_m - \Omega) \sin \alpha \cos u \\ & + \sin(\Omega_m - \Omega) \cos i \sin \alpha \sin u + \sin i \cos \alpha \sin u \end{aligned} \quad (2.53)$$

The effects of adding a tilt angle to the dipole field are numerically simulated based on a generalization of the non-tilted dipole integrations. The results of two simulations comparing the non-tilted dipole and the tilted dipole are shown in Fig. 2.8. This figure shows two integrations, both beginning with same initial

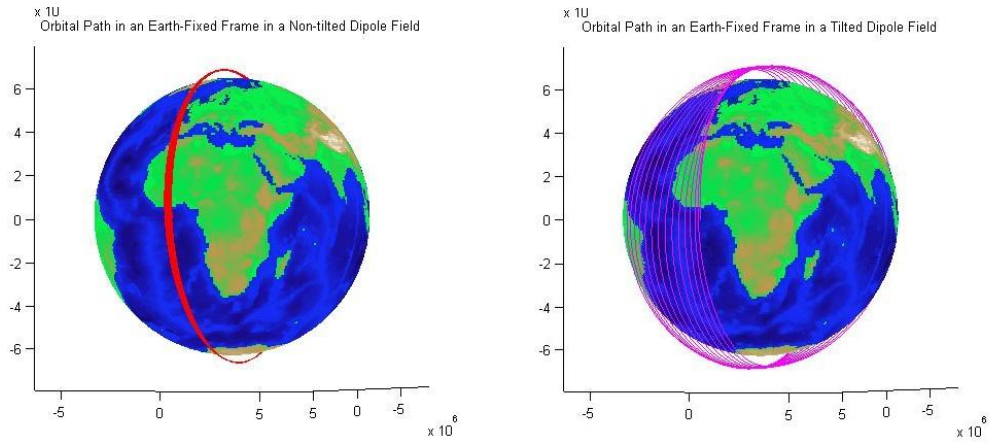


Figure 2.8: Comparison between two integrations with the same initial conditions. The left plot uses a non-tilted dipole field; the right used a dipole field tilted to 10° .

conditions, namely a 400 km altitude polar circle with a charge-to-mass ratio calculated to give GT-1 behavior. The results are plotted in an Earth-fixed coordinate system. The left plot shows the integration in a non-tilted dipole field, giving the familiar GT-1 orbit. The right plot displays the result of a simulation including a dipole field tilted at angle of 10° . This orbit is quickly driven away from GT-1 behavior. Each simulation lasts for a period of one day.

The cause of this deviation is found in the terms in Eq. 2.51 arising from the tilted dipole. In particular, the term of the form

$$\dot{E} \propto \cos(\Omega_m - \Omega) \sin \alpha \sin i \cos^2 u \quad (2.54)$$

causes a secular drift in the energy of the orbit away from its initial value. Initially the quantity $\cos(\Omega')$ is constant, where Ω' is defined as the quantity $\Omega_m - \Omega$, as this condition embodies the LAO GT-1 behavior. A term similar to Eq. 2.54 also arises in the rate of angular momentum expression. Thus, E and \mathbf{h} drift away from their nominal values, causing the spacecraft charge-to-mass ratio to be unsuitable for GT-1 behavior. As the orbit moves away from the GT-1 behavior, Ω' is no longer constant, and the spacecraft settles into a periodic motion that does not resemble GT-1.

The expression in Eq. 2.54 should go to zero when $\Omega' = \pm 90^\circ$. Figure 2.9 shows numerical simulations for both of these initial orbit longitudes. The two plots in Fig. 2.9 represent the orbital energy of the spacecraft throughout the simulation. The left plot shows $\Omega' = -90^\circ$, while the right displays $\Omega' = +90^\circ$. In the -90° case, the orbital energy remains nearly constant, and the spacecraft remains close to the intended GT-1 region. However, in the $+90^\circ$ case, the energy varies widely, and the satellite does not maintain GT-1. This behavior can be attributed to the sign changes that $\cos(\Omega')$ makes around $\pm 90^\circ$. At -90° , the sign of the cosine function switches in such a way to push the orbital energy back towards its nominal value. At $+90^\circ$, the opposite happens. Essentially, $\Omega' = -90^\circ$ is a stable equilibrium and $\Omega' = +90^\circ$ is an unstable equilibrium.

Solutions near $\Omega' = -90^\circ$ remain bounded, but periodic, in Ω' . The error in Ω' increases as the initial value of Ω' gets further from -90° , until the system becomes unstable at $\Omega' = 0^\circ$ or 180° . For the LAO GT-1 concept to be a viable application,

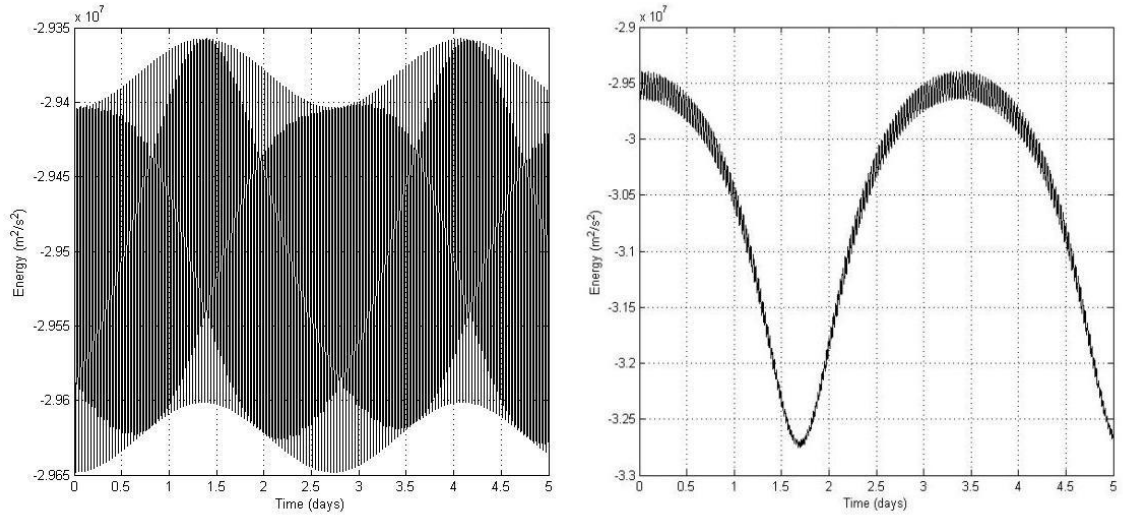


Figure 2.9: The orbital energy of two tilted dipole integrations with $\frac{q}{m} = -1.77$ C/kg, set to give GT-1 behavior. The left plot is for $\Omega' = -90^\circ$. The right shows an initial angle of $\Omega' = +90^\circ$.

a nearly constant arbitrary value of Ω' should be maintainable. However, due to symmetry of the polar orbit, a range of only 180° of Ω' allows for full longitudinal coverage. Thus, only the bounded-error cases of $180^\circ < \Omega' \leq 360^\circ$ must be considered. The next section describes how one might modulate the charge as part of a feedback-control scheme to compensate for this error in the open-loop dynamics.

2.3.2 Recovery of GT-1 Using a Non-constant Charge

To recover GT-1 behavior under the influences of a tilted dipole magnetic field, a scheme of charge modulation is developed. Again, the goal is to find a time-varying charge-to-mass ratio that forces a tilted dipole LAO to track these non-tilted solutions. First, the non-tilted field solution is further developed analytically. These analytical solutions provide a desired path to track in the tilted dipole case.

Rewriting Eqs. 2.2 and 2.14 using the charge-to-mass ratio in Eq. 2.17 gives

$$\dot{E}_D = -\omega_E \sqrt{a\mu} \sin 2u \quad (2.55)$$

$$\dot{\Omega}_D = \omega_E - \omega_E \cos 2u \quad (2.56)$$

where the subscript D refers to a desired quantity.

The rates of energy and right ascension change must be matched with the desired rates. Equations 2.51 and 2.52 are used, with the eccentricity set to zero. Simulations show that the eccentricity of an initially circular orbit remains small even as a GT-1 orbit is attempted. This simplification gives

$$\dot{E} = \frac{q}{m} AL + \frac{q}{m} AL \cos 2u + \frac{q}{m} AM \sin 2u \quad (2.57)$$

$$\dot{\Omega} = \frac{q}{m} CM - \frac{q}{m} CM \cos 2u + \frac{q}{m} CL \sin 2u \quad (2.58)$$

with the following definitions:

$$A = \omega_E B_0 \sqrt{\mu} a^{-5/2} \sin i \quad (2.59)$$

$$C = -\frac{B_0}{a^3 \sin i} \left(1 + \frac{\omega_E}{\sqrt{\mu}} a^{3/2} \cos i \right) \quad (2.60)$$

$$L = \cos(\Omega_m - \Omega) \sin \alpha \quad (2.61)$$

$$M = \sin(\Omega_m - \Omega) \cos i \sin \alpha + \sin i \cos \alpha \quad (2.62)$$

Noting how Eqs. 2.57 and 2.58 depend on the argument of latitude u , we define a charge-to-mass ratio with the same frequency dependencies:

$$\frac{q}{m} = k_1 + k_2 \sin 2u + k_3 \cos 2u \quad (2.63)$$

Thus, $\frac{q}{m}$ has a constant baseline with a sinusoidal curve superimposed.

Substituting the charge-to-mass in Eq. 2.63 into Eqs. 2.57 and 2.58 yields

$$\begin{aligned} \dot{E} &= (k_1 AL + \frac{1}{2} k_2 AM + \frac{1}{2} k_3 AL) + (k_1 AM + k_2 AL) \sin 2u \\ &\quad + (k_1 AL + k_3 AL) \cos 2u + (\frac{1}{2} k_2 AL + \frac{1}{2} k_3 AM) \sin 4u \\ &\quad + (-\frac{1}{2} k_2 AM + \frac{1}{2} k_3 AL) \cos 4u \end{aligned} \quad (2.64)$$

$$\begin{aligned}
\dot{\Omega} = & (k_1 CM + \frac{1}{2}k_2 CL - \frac{1}{2}k_3 CM) + (k_1 CL - k_2 CM) \sin 2u \\
& + (k_1 CL + k_3 CM) \cos 2u + (-\frac{1}{2}k_2 CM + \frac{1}{2}k_3 CL) \sin 4u \\
& + (-\frac{1}{2}k_2 CL - \frac{1}{2}k_3 CM) \cos 4u
\end{aligned} \tag{2.65}$$

These two expressions, Eqs. 2.64 and 2.65, are set equal to the desired rates of change given in Eqs. 2.55 and 2.56, respectively. For these equalities to always hold true, each frequency component in both the energy and right ascension expressions must equate to its counterpart in the desired track equation. Between the two different expressions, there are 10 different conditions (i.e., 2 each for the $\sin 2u$, $\cos 2u$, $\sin 4u$, $\cos 4u$, and constant terms) to be satisfied.

As there are 10 linear equations for only 3 unknowns (k_1 , k_2 , and k_3), the system is overdetermined. The system can be solved with a least-squares regression; however, not all can be satisfied simultaneously, resulting in an imperfect solution. Instead, we choose to solve a full-rank, square subspace of the 10 equations. Three equations concisely capture the desired behavior. The most important conditions are the constant term of $\dot{\Omega}$ to ensure GT-1 behavior and the constant and first sine term of the \dot{E} to keep the orbit near its nominal state. Thus, the linear system that is solved for each coefficient is given by

$$\begin{bmatrix} AM & \frac{1}{2}AM & \frac{1}{2}AL \\ AM & AL & 0 \\ CM & \frac{1}{2}CL & -\frac{1}{2}CM \end{bmatrix} \begin{bmatrix} k_1 \\ k_2 \\ k_3 \end{bmatrix} = \begin{bmatrix} 0 \\ -\omega_E^2 \sqrt{a\mu} \\ \omega_E \end{bmatrix} \tag{2.66}$$

The solution of Eq. 2.66 is substituted into Eq. 2.63 to obtain a value of $\frac{q}{m}$ at a given point in the orbit.

If A , C , L , and M are treated as constants, which assumes Ω changes exactly with the rotation of the Earth and the other orbital elements are constant, the system in Eq. 2.66 can be solved analytically. Carrying out this solution yields the

desired coefficients for defining the charge-to-mass ratio as

$$\begin{aligned}
k1 &= \frac{\omega_E (\omega_E \sqrt{a\mu} CM^2 + \omega_E \sqrt{a\mu} CL^2 + 2AL^2)}{ACM(3L^2 - M^2)} \\
k2 &= \frac{-2(A + 2\omega_E \sqrt{a\mu} C) \omega_E L}{ACM(3L^2 - M^2)} \\
k3 &= \frac{-2\omega_E (2AL^2 - AM^2 + \omega_E \sqrt{a\mu} CL^2 - \omega_E \sqrt{a\mu} CM^2)}{ACM(3L^2 - M^2)} \quad (2.67)
\end{aligned}$$

In principle, the coefficients in Eq. 2.63 will reproduce GT-1 behavior under a tilted dipole magnetic field. However, this scheme is open loop and the resulting system is not guaranteed to be stable.

Figure 2.10 shows the results of a simulation using the charge-to-mass ratio calculated by Eqs. 2.63 and 2.67. All simulations in this section begin at a time at which Earth-centered and inertial longitudes are equal. The magnetic north pole is placed at its physical location ($\alpha = 10^\circ$ and $\Omega_m = -114^\circ$). In Fig. 2.10, the top plot shows the error in right ascension angle in degrees over 15 days. The lower plot shows the error in specific energy in m^2/s^2 over the same time period. The desired average right ascension for this simulation is 0° , with the desired average energy corresponding to a 400 km altitude circular orbit. Using the solution of Eq. 2.67 and the parameters of this simulation, $\frac{q}{m}$ varies from about 2.5 C/kg to 3.3 C/kg.

For comparison, Fig. 2.11 shows the results of a simulation under the same initial conditions using a constant charge-to-mass ratio ($\frac{q}{m} = 2.93$). The same two plots are shown. The comparison of these two figures shows that the charge-varying scheme greatly reduces the errors in right ascension and energy. For a constant charge-to-mass ratio, the maximum right ascension error is 51.68° . Under the open-loop varying scheme, the maximum error is only 4.76° . However, the error in the varying charge does not asymptotically approach zero or fall into a periodic

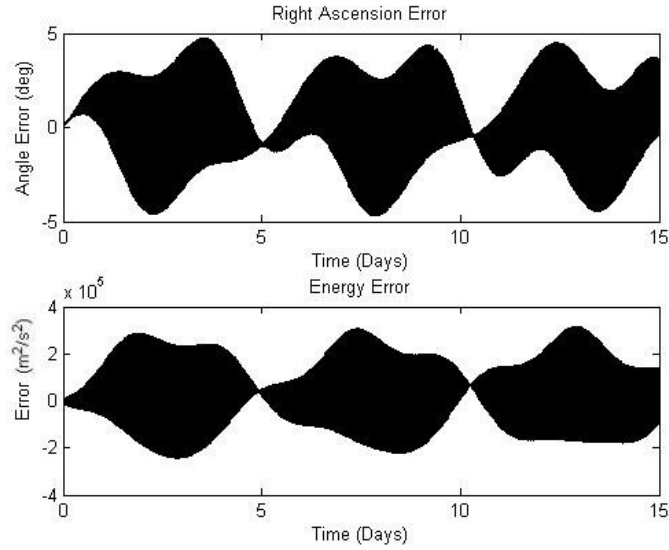


Figure 2.10: Right ascension and energy error over 15 days for a spacecraft using the variable charge-to-mass scheme defined in Eqs. 2.63 and 2.67. The desired average right ascension is 0° . The orbit is initially a 400 km altitude circle. The geomagnetic field is tilted to 10° .

motion, so its stability is not guaranteed. To enforce a guarantee, feedback control is introduced.

2.3.3 Feedback Control for $\frac{q}{m}$

While the open-loop solution generally reproduces GT-1 behavior over short time scales, the resulting system is open-loop and is prone to instabilities due to imperfect modeling of the magnetic field. To remedy this situation, feedback is introduced to the expression defining $\frac{q}{m}$:

$$\frac{q}{m} = k_1 + k_2 \sin 2u + k_3 \cos 2u + k_4(\Omega - \Omega_D) + k_5(E - E_D) \quad (2.68)$$

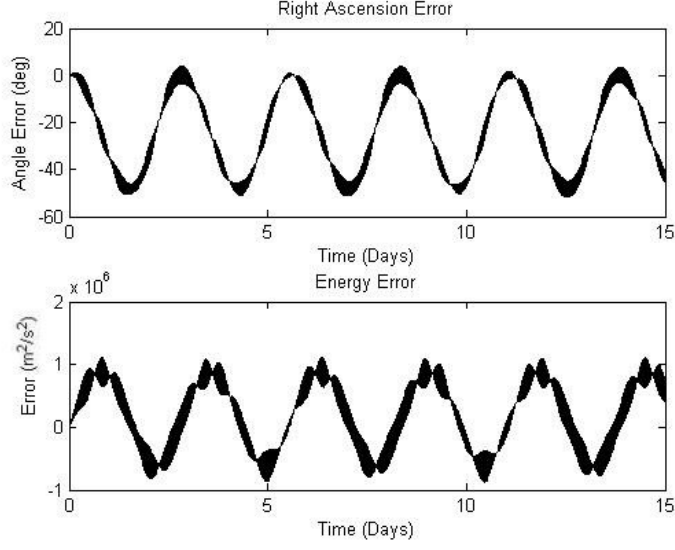


Figure 2.11: Right ascension and energy error over 15 days for a spacecraft under a constant charge. The desired average right ascension is 0° . The orbit is initially a 400 km altitude circle. The geomagnetic field is tilted to 10° .

where k_1 , k_2 , and k_3 are as given in Eq. 2.67, and Ω_D and E_D are defined by integrating Eqs. 2.56 and 2.55, respectively. Thus, k_4 and k_5 are feedback gains and the Ω and E terms are errors to be zeroed. The definition of $\frac{q}{m}$ in Eq. 2.68 is substituted into Eqs. 2.58 and 2.57. The terms involving k_1 , k_2 , and k_3 are assumed to satisfy the 10 equation system defined by Eqs. 2.65 and 2.64. This assumption is not explicitly true, as k_1 , k_2 , and k_3 are only chosen to satisfy Eq. 2.66, but the resulting error can be treated as a small unmodeled disturbance. Applying this assumption gives

$$\begin{aligned} \dot{\Omega} = & \dot{\Omega}_D + (CM - CM \cos 2u + CL \sin 2u)(k_4(\Omega - \Omega_D) \\ & + k_5(E - E_D)) \end{aligned} \quad (2.69)$$

$$\begin{aligned} \dot{E} = & \dot{E}_D + (AL + AL \cos 2u + AM \sin 2u)(k_4(\Omega - \Omega_D) \\ & + k_5(E - E_D)) \end{aligned} \quad (2.70)$$

Combining Eqs. 2.69 and 2.70 into a state-space system yields

$$\begin{aligned} \begin{bmatrix} \dot{\Omega} - \dot{\Omega}_D \\ \dot{E} - \dot{E}_D \end{bmatrix} &= \begin{bmatrix} k_4 C(M - M \cos 2u + L \sin 2u) & k_5 C(M - M \cos 2u + L \sin 2u) \\ k_4 A(L + L \cos 2u + M \sin 2u) & k_5 A(L + L \cos 2u + M \sin 2u) \end{bmatrix} \\ &\quad \times \begin{bmatrix} \Omega - \Omega_D \\ E - E_D \end{bmatrix} \end{aligned} \tag{2.71}$$

Equation 2.71 represents a closed-loop, linear, time-varying (LTV) system. Describing the stability of an LTV system is not as simple or straightforward as the time-invariant case. The following section gives a review of LTV stability criteria.

Stability of LTV Systems

Given an LTV state matrix, $A(t)$, the eigenvalues of the state matrix being in the left-half plane is neither a sufficient nor necessary condition of stability. Many examples exist of LTV systems with constant, negative, real eigenvalues that exhibit unstable behavior. Willems[46] and DeCarlo[47] give an overview of LTV stability analysis techniques. The conceptually simplest techniques involve the state transition matrix, $\Phi(t, t_0)$. The system is stable if and only if the condition

$$\|\Phi(t, t_0)\| < M(t_0) \tag{2.72}$$

where M is some bound that may depend on t_0 , and $\|(\cdot)\|$ represents any valid matrix norm.[46] If a bound M can be found that does not depend on t_0 , the system is said to be uniformly stable. This technique, of course, relies on knowledge of the state transition matrix.

Lyapunov stability can also be defined for LTV systems. The system is Lyapunov stable if there exist $P(t)$, a positive definite, continuous, differentiable, and bounded matrix, and $Q(t)$, a positive definite, continuous, and bounded matrix, which satisfy

$$\dot{P}(t) + P(t)A(t) + A^T(t)P(t) = -Q(t) \quad (2.73)$$

P and Q are guaranteed to exist for any stable $A(t)$, but are nontrivial to calculate. For an LTI system the Lyapunov equation reduces to a simple algebraic equation. In the LTV case, we are left with a second differential equation, the solution of which generally requires knowledge of the state transition matrix.

Other techniques based on the state transition matrix (STM) exist. If the STM is periodic, Floquet theory can be used to predict system stability. See Willems for a full description.[46] If the state matrix changes sufficiently slowly in time, the state matrix having negative real parts for each eigenvalue can show stability. Rosenbrock puts explicit bounds on the rate of change of the state matrix.[48] Effectively, these bounds require that the system approaches equilibrium "fast" compared to the changes in $A(t)$. For our $A(t)$ above, these bounds do not exist.

More advanced techniques make use of the logarithmic norm of a matrix. The logarithmic norm of a matrix, sometimes called the measure of a matrix, is a "norm-like" quantity defined with respect to some particular matrix norm $\|(\cdot)\|$ as[49]

$$\mu(A) \equiv \lim_{\theta \rightarrow 0} \frac{\|I + \theta A\| - 1}{\theta} \quad (2.74)$$

A particular logarithmic norm is said to be induced by a particular matrix norm. A good introduction to the logarithmic norm is found in Desoer[49], along with expressions for the logarithmic norms induced by the 1-, 2-, and ∞ -norms. Surveys of logarithmic norm literature are given in Strom[50] and Soderlind[51].

The logarithmic norm establishes the following sufficient (but not necessary) condition for the stability of an LTV system:[52]

$$\|x_0\| \exp \left[- \int_{t_0}^t \mu(-A(s)) ds \right] \leq \|x(t)\| \leq \|x_0\| \exp \left[\int_{t_0}^t \mu(A(s)) ds \right] \quad (2.75)$$

(The logarithmic norm can take on negative values.) This condition essentially implies that the integral of the logarithmic norm of the state matrix is bounded, then the state is bounded. Willems[46] gives Wazewski's inequality, which is based on the logarithmic norm induced by the 2-norm. The system is stable if the inequality

$$\lim_{t \rightarrow \infty} \int_{t_0}^t \lambda_{max}(s) ds \leq M(t_0) \quad (2.76)$$

holds, where λ_{max} is the largest eigenvalue of the quantity $(A(t) + A^T(t))$. Mori[52] gives a similar condition based on the 1-norm induced matrix measure. These can be useful, but since they are not necessary conditions, any given matrix $A(t)$ can fail these inequalities and still be stable.

A Stabilizing Controller

We do not develop specific bounds in the method of Rosenbrock, but use the eigenvalues of the state matrix as a guide to selecting a controller, which will later be shown numerically to be stable based on the state transition matrix. Solving for the eigenvalues yields the following condition on the gains k_4 and k_5 :

$$k_5 < -k_4 \frac{C(M - M \cos 2u + L \sin 2u)}{A(L + L \cos 2u + M \sin 2u)} \quad (2.77)$$

Gains that meet the criterion in Eq. 2.77 give the system a negative real eigenvalue. The second eigenvalue of the system is always zero. Using Eq. 2.77 as a guideline,

a stabilizing controller is found to be

$$\begin{aligned}
k_4 &= -0.5 \\
k_5 &= \frac{-k_4 K + (k_4 - 0.05)\|K\|}{A(L + L \cos 2u + M \sin 2u)} \\
K &= C(M - M \cos 2u + L \sin 2u)
\end{aligned} \tag{2.78}$$

where the symbol $\|(\cdot)\|$ refers to absolute value. The gain k_5 is not constant. This set of gains results in stable errors in energy and right ascension over at least 180° of desired average right ascension angle in simulation, implying that any Earth-fixed longitude can be tracked in GT-1 fashion with bounded, finite error.

The results of the controller in Eq. 2.78 are explored numerically. Figure 2.12 shows right ascension and energy error under the same conditions as the simulations shown in Figs. 2.10 and 2.11. The feedback control scheme uses about the same range of $\frac{q}{m}$ values as the open loop scheme. The maximum right ascension errors of the feedback case is 4.12° , less than the open loop error of 4.76° . Additionally, the error in the feedback case falls into a periodic motion, and is stable for all time.

The plots shown in Fig. 2.13 are intended to demonstrate the improvement in stability of the feedback control scheme over the open loop variable $\frac{q}{m}$ case. Figure 2.13(a) shows the results of an open loop simulation similar to those done previously, but with a desired average right ascension angle of 70° . This orbit deviates widely from the desired path. The system in this case is unstable. Figure 2.13(b) shows the same simulation using the feedback controller. The controller is able to stabilize the system, and results in bounded error. Despite the large error bounds, the underlying system is stable.

Figure 2.14 further elucidates the stable, periodic nature of the feedback solution. This figure shows the right ascension and energy error under feedback

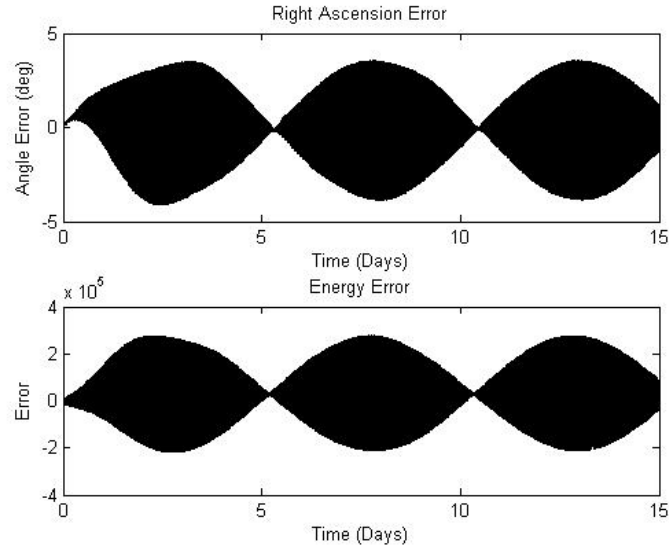
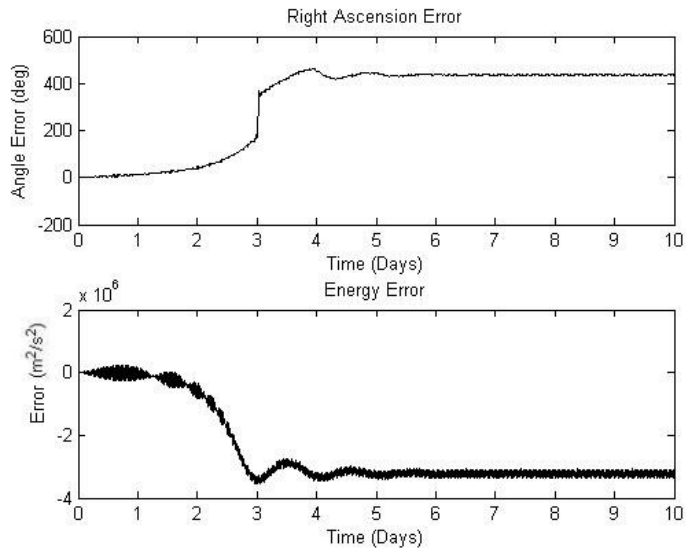


Figure 2.12: Right ascension and energy error over 15 days for a spacecraft using the feedback control scheme defined in Eq. 2.68. The desired average right ascension is 0° . The orbit is initially a 400 km altitude circle. The geomagnetic field is tilted to 10° .

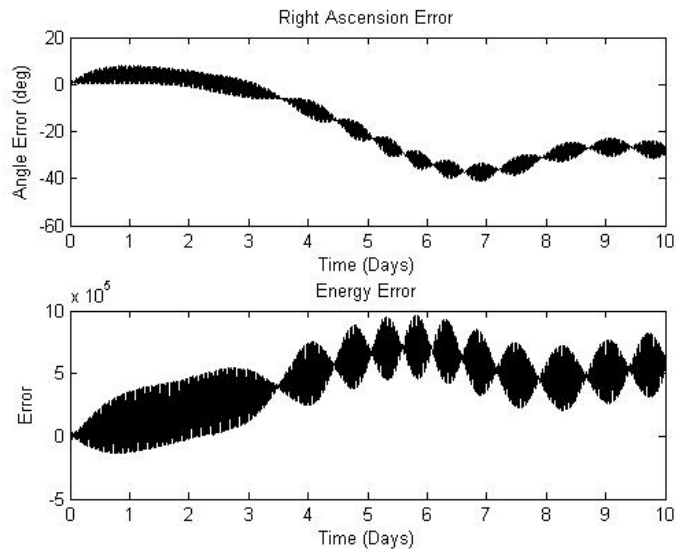
control, for a circular, 400 km orbit with desired average right ascension of 45° . This simulation is carried out for 75 days, and the periodic nature of the error is well displayed.

To show numerically that the controller in Eq. 2.78 does indeed stabilize the system in Eq. 2.71, we use the result that an LTV system is stable if and only if the norm of its state transition matrix is bounded for all time.[46] We numerically solve for the state transition matrix $\Phi(t, 0)$ for the system simulated in Fig. 2.14. Given the time history of this simulation, the system matrix of Eq. 2.71 can be found as a function of time. Two linearly independent initial conditions, x_{01} and x_{02} are then integrated using the system matrix. With the two resulting time histories, $x_1(t)$ and $x_2(t)$, the state transition matrix is given by

$$\Phi(t, 0) = [x_1(t) \quad x_2(t)][x_{01} \quad x_{02}]^{-1} \quad (2.79)$$



(a) Open loop scheme



(b) Feedback scheme

Figure 2.13: Right ascension and energy error over 15 days for a spacecraft using the open loop scheme and the feedback controller. The desired average right ascension is 70° . The orbit is initially a 400 km altitude circle. The geomagnetic field is tilted to 10° .

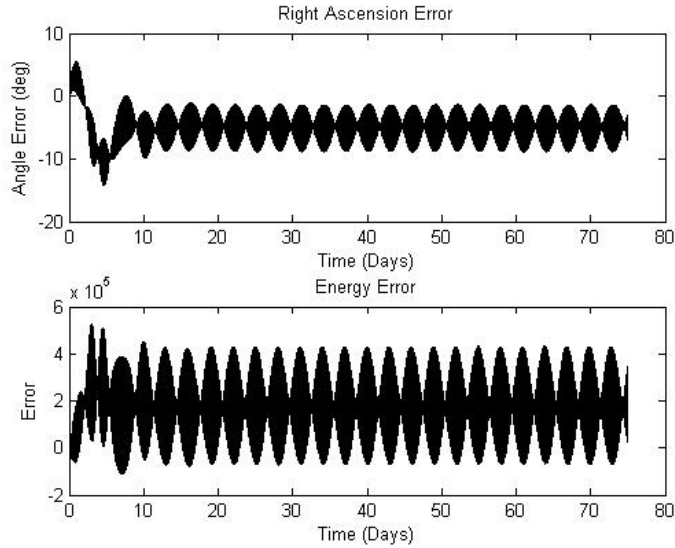


Figure 2.14: Right ascension and energy error over 75 days for a spacecraft using the feedback control scheme defined in Eq. 2.68. The desired average right ascension is 45° . The orbit is initially a 400 km altitude circle. The geomagnetic field is tilted to 10° .

Figure 2.15 shows the matrix induced 2-norm of the state transition matrix. As the norm is bounded, the system is stable. However, the result in Fig. 2.15 does not give uniform stability of the system, nor does it prove that the system stable over a range of desired right ascension values. The norm of $\Phi(t, 0)$ approaching 0 as time increases leads to the conclusion that Eq. 2.71 is asymptotically stable, but the error plots in Fig. 2.14 plainly show errors approaching some non-zero value. In Fig. 2.14, the linear system in Eq. 2.71 is not being simulated, but the full nonlinear system of Eqs. 1.11-1.13 augmented to include the tilted dipole field. Assumptions made in deriving Eq. 2.71 cause it to be not entirely accurate.

However, we show numerically that the full nonlinear solution still approaches a stable and periodic non-zero error. Figure 2.16 is used to more rigorously show the periodicity of the right ascension error in Fig. 2.14. At first glance, the long-term

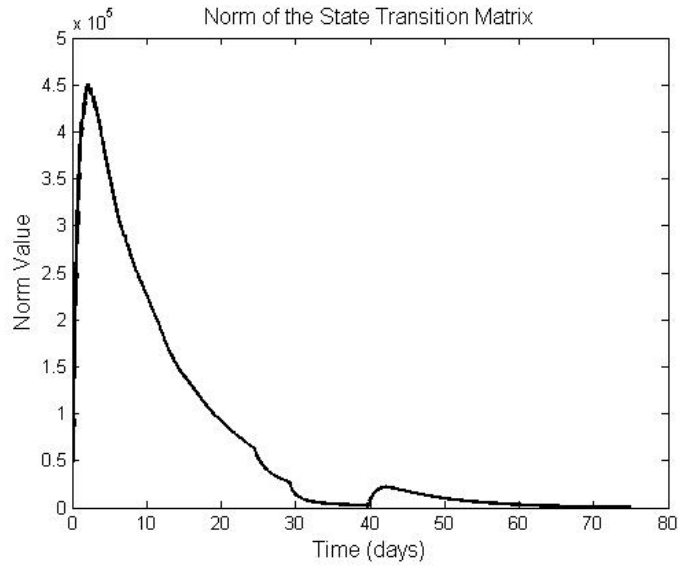


Figure 2.15: Matrix norm of the state transition matrix of the system in Eq. 2.71 using data from the simulation shown in Fig. 2.14.

behavior of the error appears to be a periodic beat of two similar frequencies. To test this hypothesis, the error data is fast Fourier transformed. The power spectral density of this transform is calculated and shows two distinct peaks. One peak occurs at a frequency near twice per orbit; the other occurs at slightly less than twice per orbit. The data is numerically resampled at the beat frequency of the two frequency peaks. The long term average right ascension error is subtracted from the resampled data, and the resulting curve is plotted in Fig. 2.16. As the transient response damps out, this curve goes to zero, indicating good agreement with the periodic, beating assumption.

The feedback controller presented in Eq. 2.68 using the gains in Eq. 2.78 stabilizes GT-1 behavior under the influence of tilted geomagnetic field. This controller consists of proportional feedback based on a linearized model and does not guarantee asymptotic convergence. However, the controller does bound the error in right ascension and energy. Numerical analysis shows that the system is stabilized

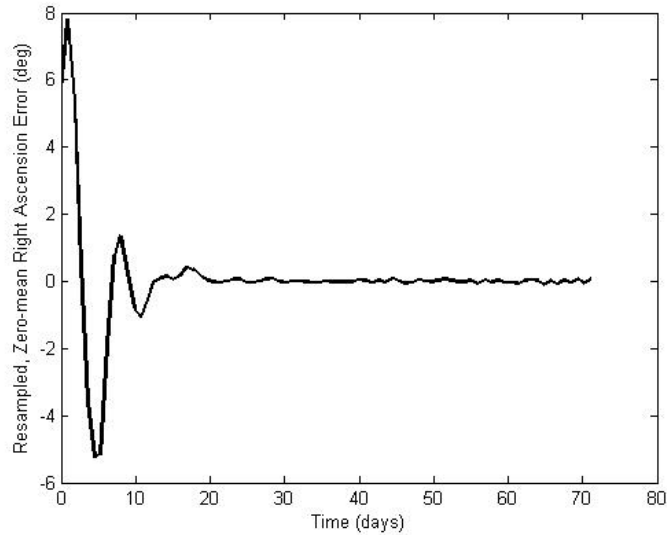


Figure 2.16: Resampled right ascension error over 75 days for the simulation displayed in Fig. 2.14. The actual right ascension error is Fourier transformed. The power spectral density of this transform is used to find the two main frequencies present, and the error is numerically resampled at the difference between these frequencies. The long-term average error is also subtracted off to create a zero-mean system.

for a full range of desired average right ascensions and initial orbit altitudes.

2.4 Chapter Conclusions

LAOs are based on simple physical principles but can be used to accomplish a variety of complex orbital behaviors. The resulting changes in orbital elements due to the Lorentz force can be used to develop novel applications. These new applications include polar, single-orbit repeat-groundtrack (GT-1) satellites. A successfully implemented GT-1 LAO orbit would greatly outperform today's imaging satellites. These orbits can exist at any altitude, not just the traditional geosyn-

chronous height. We have derived from first principles a simple expression for the charge required to achieve such an orbit. This expression is verified numerically and allows for mission designs to be evaluated. Also numerically confirmed is the existence of equatorial orbits with arbitrary control over the location of perigee. Again, a simple expression for the charge required is shown from first principles. These orbits can create an Earth-synchronous orbit whose perigee and apogee lie at constant longitudes.

The presence of a tilt in the Earth's magnetic field greatly complicates GT-1 behavior. The GT-1 orbit in this case is not stable for constant charge. However, modulating the charge as a means of feedback control is shown to stabilize a GT-1 LAO.

CHAPTER 3
**GRAVITY-ASSIST MANEUVERS AUGMENTED BY THE
LORENTZ FORCE**

In this chapter, the effects of the Lorentz force on gravity-assist maneuvers is examined. We consider a charged spacecraft that performs a hyperbolic flyby of a planet with a non-negligible magnetosphere. If the charge on the satellite is modulated, the usefulness and effectiveness of the flyby can be extended in several ways with no expenditure of propellant. Both analytical and simulation results are presented for satellites in equatorial orbits within dipole magnetic fields. The spacecraft's exit asymptote from the flyby target's sphere of influence can be changed to an arbitrary direction. The spacecraft can also be captured at the target planet, or the assist maneuver can be timed with more flexibility than a gravity-only flyby.

3.1 Introduction

This chapter addresses the use of LAOs as a way to increase the flexibility and effectiveness of gravity-assist maneuvers. The methods used to analyze LAOs consist mainly of perturbations to Keplerian orbits, following the work in Chapter 2. The next section provides an extension to these perturbation equations, a note on Solar System magnetic fields, and an overview of flyby trajectories, followed by a study of the extension of flybys to include LAO dynamics. Adding the Lorentz force to hyperbolic trajectories creates several novel applications including arbitrary exit angle from the planet frame, propellantless capture, and flexible flyby timing.

3.1.1 Perturbation Equations

Recalling Eqs. 1.27 and 1.30:

$$\dot{E} = \frac{q}{m} \omega_E [(\mathbf{v} \cdot \hat{\mathbf{n}})(\mathbf{B} \cdot \mathbf{r}) - (\mathbf{v} \cdot \mathbf{r})(\hat{\mathbf{n}} \cdot \mathbf{B})] \quad (1.27)$$

$$\dot{\mathbf{h}} = \frac{q}{m} (\mathbf{B} \cdot \mathbf{r}) \mathbf{v} - \frac{q}{m} (\mathbf{r} \cdot \mathbf{v}) \mathbf{B} - \frac{q}{m} \omega_E (\mathbf{B} \cdot \mathbf{r}) (\hat{\mathbf{n}} \times \mathbf{r}) \quad (1.30)$$

we have expressions for the change in energy and angular momentum of the orbit, where, throughout this chapter, we use ω_E to refer to the rotation rate of any planet of interest. But the combination of energy change and angular momentum change does not complete a full set of independent derivatives describing changes in the orbit. To fully describe changes in the orbit, we use the eccentricity vector, \mathbf{e} . The eccentricity vector is defined as

$$\mathbf{e} = \frac{\mathbf{v} \times \mathbf{h}}{\mu} - \hat{\mathbf{r}} \quad (3.1)$$

where $\hat{\mathbf{r}}$ is a unit vector in the radial direction. Geometrically, the eccentricity vector points from the center of the central planet towards the periapsis of the orbit. The magnitude of \mathbf{e} is equal to the orbital eccentricity, e . The time rate of change of \mathbf{e} due to the Lorentz force is

$$\begin{aligned} \dot{\mathbf{e}} = & -\frac{q}{m} \frac{1}{\mu} \omega_E (\mathbf{B} \cdot \hat{\mathbf{n}}) (\mathbf{r} \cdot \mathbf{v}) \mathbf{r} + \frac{q}{m} \frac{1}{\mu} [\omega_E (\mathbf{B} \cdot \hat{\mathbf{n}}) r^2 - (\mathbf{r} \times \mathbf{v}) \cdot \mathbf{B}] \mathbf{v} \quad (3.2) \\ & - \frac{q}{m} \frac{1}{\mu} (\mathbf{r} \cdot \mathbf{v}) (\mathbf{v} \times \mathbf{B}) \end{aligned}$$

Equations 1.27, 1.30, and 3.2 provide the information necessary to determine changes in five of the six orbital elements. Change in the semimajor axis, a , are calculated using the change in energy. Change to the orbital inclination, i , and right ascension of the ascending node, Ω , are found based on changes in the direction the angular momentum vector. Change in the eccentricity, e , and the longitude of periapsis, Π , can be gleaned from the change in the magnitude and

direction of the eccentricity vector, respectively. The time rate of change of the true anomaly is derived independently in Section 3.2.2.

3.1.2 Planetary Magnetic Fields

LAOs require a planetary magnetic field to work. The stronger a planet's magnetic field is, the more effective the Lorentz force can be. An overview of the magnetic fields available in the Solar System appears in Chapter 1. The six planets with intrinsic magnetic fields all have relatively strong dipole components. This chapter models all magnetic fields as non-tilted dipoles. The large tilt-angle fields of Neptune and Uranus are not considered here.

Jupiter and Earth are the most attractive targets for Lorentz augmentation of flyby maneuvers. Both planets are used for gravity-assists for interplanetary missions. This chapter focuses on Jupiter flybys, but the analysis is valid at Earth and Saturn as well. Although Saturn is not convenient for gravitational flybys, its environment is well suited to LAOs. The small tilt of its dipole component allows for a simpler and more effective controller to be implemented. And, while Jupiter has a plasmasphere constantly being filled with charge-eroding ions from volcanic Io, Saturn has a more benign radiation environment with no heavily volcanic moons and constant absorption of charged particles by the massive ring system.

3.1.3 Gravity-Assist Maneuvers

The gravity assist or flyby is a powerful tool in facilitating interplanetary missions. A gravity-assist maneuver uses the gravity well of a planet to alter the heliocentric

orbit of a spacecraft. Interplanetary satellites have made extensive use of flybys since the Mariner 10 mission first used a flyby of Venus on its way to Mercury. In the simplest (but still reasonably accurate) analysis of a flyby maneuver, the hyperbolic trajectory of the spacecraft about the target planet is assumed to take a small amount of time compared to the planet's heliocentric orbit. This chapter also assumes all orbits are coplanar and all planetary paths are circular. The sphere of influence approximation is also used. Schaub and Junkins[53] offer a more in-depth treatment of flybys and spheres of influence.

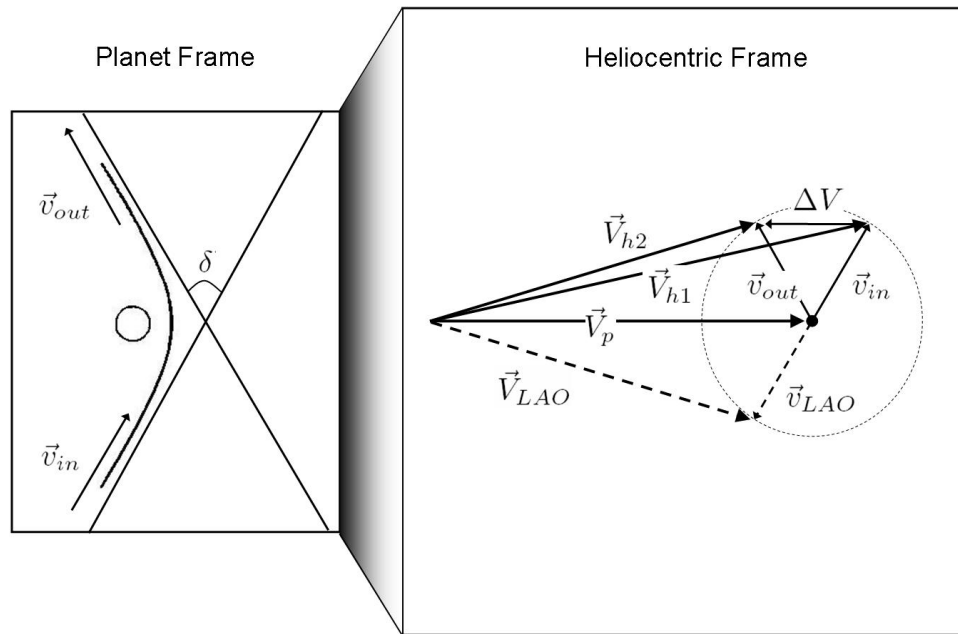


Figure 3.1: Flyby trajectory vector definitions. The dotted vectors in the heliocentric view indicate a possible LAO trajectory resulting in a significantly larger ΔV .

A gravity-assist maneuver uses the gravitational attraction of a target planet to rotate a portion of the heliocentric spacecraft velocity. In a heliocentric frame, the planet has velocity \mathbf{V}_p and the spacecraft has initial heliocentric velocity \mathbf{V}_{h1} . In a frame moving with the planet, the spacecraft has a velocity with respect to the planet of $\mathbf{v}_{in} = \mathbf{V}_{h1} - \mathbf{V}_p$ with a magnitude of v_∞ . Figure 3.1 depicts these

quantities. The velocity \mathbf{v}_{in} and a periapsis distance, r_p , fix the planetocentric hyperbolic orbit. The periapsis distance is a free variable to be set by mission design. The eccentricity of this orbit gives the turning angle of the hyperbola, δ , through the relation $\sin(\delta/2) = 1/e$.^[53] The outbound planetocentric velocity of the spacecraft, \mathbf{v}_{out} , is equal to the inbound velocity, \mathbf{v}_{in} , turned through the angle δ and having the same magnitude, v_∞ . The final heliocentric spacecraft velocity is then $\mathbf{V}_{h2} = \mathbf{v}_{out} + \mathbf{V}_p$. Thus, the spacecraft sees a heliocentric change in velocity of

$$\Delta V = 2v_\infty \sin(\delta/2) \quad (3.3)$$

The main goal of this work is to use the Lorentz force to rotate \mathbf{v}_{out} through an arbitrary angle γ , giving the mission designer much more freedom in obtaining a desired ΔV .

Flybys can also be used to create multi-body periodic orbits, such as the Aldrin cyler.^[54] In the Aldrin orbit, repeated flybys of Earth and Mars are used to create a trajectory that cycles between the two planets, using much less propellant than single-use spacecraft making the same number of rendezvous. The Lorentz force can be used to make small adjustments to these flybys, further reducing the amount of propellant used by a cyler.

A final quantity of interest is the time of flight in the planetary frame. A mission plan requires an accurate assessment of the maneuver's duration. Time of flight in a hyperbolic orbit can be found from the hyperbolic anomaly, F . In terms of the true anomaly, ν , the hyperbolic anomaly is^[53]

$$F = \cosh^{-1} \left(\frac{e + \cos \nu}{1 + e \cos \nu} \right) \quad (3.4)$$

The hyperbolic anomaly can be related the mean anomaly, M , by^[53]

$$M = e \sinh F - F \quad (3.5)$$

Like Kepler's equation for eccentric anomaly, Eq. 3.5 cannot be solved in closed form. However, in certain special cases, the time of flight between two points in the orbit can be calculated. One such case is the time to travel between two symmetric points in the orbit (i.e., two points the same angular distance from periapsis). In this case, the resulting time of flight, Δt , is

$$\Delta t = 1/n(2e \sinh F - 2F) \quad (3.6)$$

where n is the mean motion of the satellite, and F is taken to be the positive of the two symmetric hyperbolic anomalies. For a hyperbolic orbit, n is defined as $\sqrt{\mu/(-a)^3}$, because the semimajor axis is negative.

3.2 Applications

This section discusses two types of Lorentz-augmented flyby: changes during a single hyperbolic pass and longer-duration maneuvers that involve a temporary capture at Jupiter. Both analytical and numerical techniques are used to study the costs and benefits of LAO maneuvers.

3.2.1 Single-Orbit Lorentz Modifications

On a single hyperbolic pass, the Lorentz force can change the orbit in several ways. For a constant charge applied throughout the orbit, both the semimajor axis and eccentricity of the orbit undergo transient changes but exhibit no net change over the course of the orbit. However, Π , the longitude of periapsis, undergoes a secular change throughout the orbit. Because only equatorial orbits are considered in this chapter, longitude of periapsis, Π , is used to locate perijove rather than the

more traditional argument of periapsis, ω . Their difference is simple: longitude of periapsis is measured from an inertially fixed x -axis, while argument of periapsis is measured from the line of nodes, which is undefined in an equatorial orbit. This change in the location of periapsis affects the asymptotic direction of the outbound leg of the hyperbola (without changing the magnitude of its velocity) and thus affects the outbound heliocentric velocity. If the charge on the satellite is modulated during the course of the orbit the semimajor axis, eccentricity, and periapsis location can all be changed, affecting both the magnitude and direction of the outbound velocity.

We derive perturbation equations based on an osculating-element assumption. The perturbation equations are based on the general derivatives in Eqs. 1.27, 1.30, and 3.2, following the methods of Burns[10] and the earlier work of Chapters 1 and 2. The magnetic field of Jupiter is modeled as an axis-aligned dipole. A dipole model for the Jovian field is accurate enough for our purposes in a region from approximately 5 to 40 Jovian radii[13]. The strong temporal components and ring currents in the Jovian field are not considered here. The Jovian dipole component is not axis-aligned[9], but the tilt provides relatively small perturbations to orbits restricted to the equatorial plane. Here the small in-plane components of the magnetic field are ignored.

Relating changes in semimajor axis to changes in energy by taking the derivative of $E = -\mu/(2a)$ gives an expression for changes in semimajor axis due to the Lorentz force:

$$\dot{a} = 2 \frac{q}{m} B_0 \frac{\omega_E}{\sqrt{\mu}} \frac{a^2 e}{[a(1 - e^2)]^{5/2}} \sin \nu (1 + e \cos \nu)^2 \quad (3.7)$$

Equation 3.2 is used to develop two further perturbation equations. The change

in orbital eccentricity is

$$\dot{e} = \frac{q}{m} B_0 \left[\frac{\omega_E}{\sqrt{\mu}} - \frac{1 - e^2}{[a(1 - e^2)]^{3/2}} \right] \frac{\sin \nu}{[a(1 - e^2)]^{3/2}} (1 + e \cos \nu)^2 \quad (3.8)$$

Directional changes in the eccentricity vector within the plane of the orbit directly correspond to changes in the location of periapsis. Solving for this angular change gives the time rate of change of longitude of periapsis as

$$\dot{\Pi} = \frac{q}{m} B_0 \left[\left(\frac{e^2 + 1}{[a(1 - e^2)]^{3/2}} - \frac{\omega_E}{\sqrt{\mu}} \right) \cos \nu + \frac{2e}{[a(1 - e^2)]^{3/2}} \right] \frac{(1 + e \cos \nu)^2}{e[a(1 - e^2)]^{3/2}} \quad (3.9)$$

While Eqs. 3.7 and 3.8 are periodic over true anomaly ν , Eq. 3.9 has a term that increases in a secular way. For a constant charge over several orbits, the semimajor axis and eccentricity repeat periodically, while the longitude of periapsis changes monotonically.

We use an osculating-element assumption to derive an expression for the average change in longitude of periapsis per orbit under the influence of a constant charge. The time rate of change of true anomaly is assumed to have its Keplerian value of

$$\dot{\nu} = \frac{\sqrt{\mu}(1 + e \cos \nu)^2}{[a(1 - e^2)]^{3/2}} \quad (3.10)$$

Substituting this relationship into Eq. 3.9, integrating through one orbit, and solving for $\frac{q}{m}$ gives

$$\frac{q}{m} = \Delta \Pi \frac{\sqrt{\mu}}{B_0} e \left[2 \left(\frac{e^2 + 1}{[a(1 - e^2)]^{3/2}} - \frac{\omega_E}{\sqrt{\mu}} \right) \sin \nu_\infty + \frac{4e}{[a(1 - e^2)]^{3/2}} \nu_\infty \right]^{-1} \quad (3.11)$$

where ν_∞ is the true anomaly at infinity, given by $\cos \nu_\infty = -1/e$ for a hyperbolic orbit. Equation 3.11 is used to predict the charge-to-mass ratio required to obtain a particular change in the orbit.

Figure 3.2 shows the result of using Eq. 3.11 to model a rotation of an orbit. This simulation uses a two-body approximation with Jupiter as the sole source of

gravity. All simulations in this chapter use two-body gravity with initial conditions that place the spacecraft at the edge of Jupiter’s sphere of influence (SOI). The radius of Jupiter’s SOI is[53]

$$R_{SOI} = \left(\frac{M_J}{M_S} \right)^{2/5} R_{S-J} \quad (3.12)$$

where M_J and M_S represent the masses of Jupiter and the Sun, respectively, and R_{S-J} is the average distance between the two. By this definition, Jupiter’s sphere of influence is about 48 million km in radius. While the SOI concept is not strictly correct, it is used here to facilitate a straightforward discussion of the orbital dynamics. Each simulation begins with the spacecraft on a Hohmann transfer orbit between Earth and Jupiter. At Jupiter, the spacecraft’s velocity is parallel to the planet’s. The Jovicentric orbit is fully defined by specifying the radius of perijove.

For the simulation displayed in Fig. 3.2, the perijove of the initial Keplerian hyperbola is 4 Jovian radii. This orbit (with $\frac{q}{m} = 0$ C/kg) is shown as solid black line in the figure. Equation 3.11 is then used to calculate the charge-to-mass ratio that results in a rotation of the hyperbolic exit asymptote of -30° . The resulting $\frac{q}{m}$ is about -5.6 C/kg. The path of this spacecraft is shown as a dashed line in the figure.

Also shown in Fig. 3.2 is the path of a satellite with a $\frac{q}{m}$ of -7.46 C/kg, represented by the dot-dash line. This value of charge-to-mass ratio is calculated numerically to give exactly the requested -30° rotation. A simple numerical scheme is used for this calculation. An initial guess of $\frac{q}{m}$ is obtained from Eq. 3.11. This value is used in a full numerical integration of the coupled perturbation equations, instead of the osculating approximation that led to Eq. 3.11. A simple Newton-Raphson solver is then employed over repeated integrations to find the value of $\frac{q}{m}$

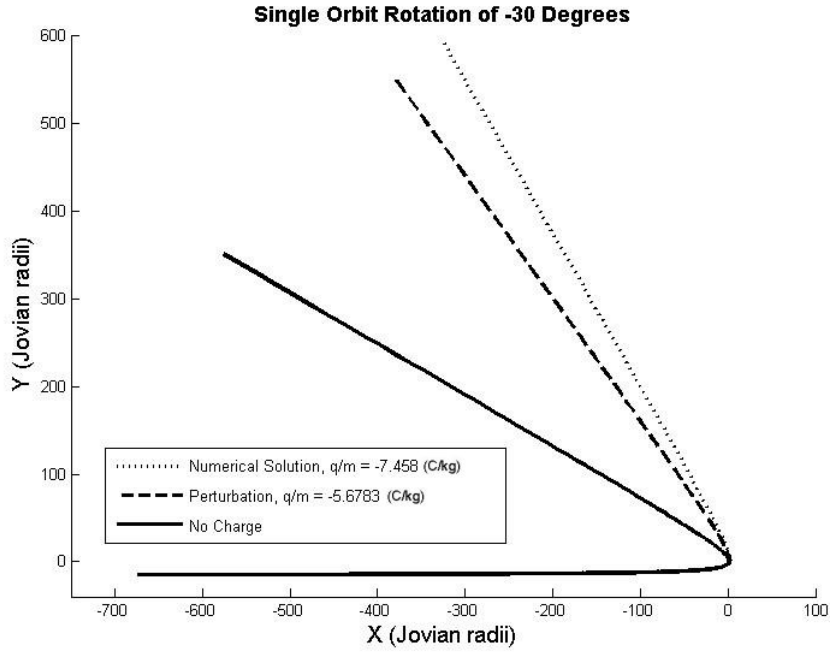


Figure 3.2: Hyperbolic orbit for single-orbit rotation of periapsis, showing the Keplerian orbit, the numerically calculated solution, and the perturbation solution for charge-to-mass ratio.

that accurately gives the desired orbit rotation.

Figure 3.2 clearly shows that results obtained using Eq. 3.11 are inaccurate. This solution gives an error of about 6° over a rotation of only 30° . As the size of the rotation increases, both the charge required and the perturbation error increase. One source of this error is the nature of a hyperbolic orbit. For most of the orbit, a satellite is far from the central body and moving relatively slowly. However, around periapsis, the satellite is close to planet and moves extremely fast, making the Lorentz force much larger. This effect is demonstrated in Fig. 3.2. The inbound leg of each orbit shown is nearly identical. Only near perijove do

the effects of the Lorentz force become apparent. The orbits of the LAO satellites undergo large changes in a short amount of time, undermining the accuracy of perturbation and osculating-element assumptions in performing integrations such as those used to obtain Eq. 3.11.

Small changes are easy to effect in a single hyperbolic pass. However, as the desired change to an orbit grows, the necessary charge required becomes prohibitively large. If a large enough change in exit angle is desired, the $\frac{q}{m}$ necessary causes the osculating orbit assumption to break down in the presence of non-Keplerian orbit dynamics. Large changes are more easily and accurately brought about by slowly, repeatedly tweaking the orbit after temporarily capturing the satellite, as shown in the following sections.

One additional degree of freedom can be exploited in the single-pass modification: the charge-to-mass ratio does not need to be constant. With a variable charge-to-mass ratio the orbital energy, eccentricity, and exit angle can all be controlled to some extent. This type of maneuver is not expressly studied here, but, as in the case of pure rotation, the charge required to make significant orbit changes becomes prohibitively large.

3.2.2 Lorentz Augmented Capture

A readily apparent application of LAOs is the capture of a spacecraft at a target planet. Atchison, et al.[13] provide a detailed look at Lorentz Augmented Capture at Jupiter. They discuss the possibility of capturing satellites from many different entry orbits with charge-to-mass ratios as low as 0.005 C/kg. These captures are effected using a simple bang-bang charge controller. The capture maneuver is

allowed to take up to five years over a large number of Jovian orbits. Atchison uses a conservative definition of capture that forces the satellite into a near-circular orbit at a reasonable distance from Jupiter.

This chapter takes a slightly different approach to capture, as our main goal is to shape gravity-assist maneuvers, not facilitate planetary capture. However, we derive here expressions related to capturing a spacecraft in single Jovian orbit. With a single-orbit capture, a satellite can temporarily stay in the neighborhood of Jupiter, allowing for adjustments in the timing and exit conditions of a flyby maneuver. Any spacecraft captured in a single orbit can also escape in single orbit, with a charge of the same magnitude.

The quantity p , often called the orbit parameter or semi-latus rectum, can be used to simplify some the LAO analysis. The semi-latus rectum is fundamentally connected to the magnitude of the angular momentum of the orbit, as in

$$p = h^2/\mu = a(1 - e^2) \quad (3.13)$$

In the same way as changes in the semimajor axis represent only changes in the orbital energy, changes in p reflect only changes in the angular momentum. Taking the derivative of Eq. 3.13 with respect to time yields

$$\dot{p} = \dot{a}(1 - e^2) - 2ae\dot{e} \quad (3.14)$$

Adapting this definition to an LAO by using Eqs. 3.7 and 3.8, gives

$$\dot{p} = 2\frac{q}{m}B_0\frac{e}{p^2}\sin\nu(1 + e\cos\nu)^2 \quad (3.15)$$

Equation 3.15, along with

$$\dot{e} = \frac{q}{m}B_0\left[\frac{\omega_E}{\sqrt{\mu}} - \frac{1 - e^2}{p^{3/2}}\right]\sin\nu\frac{(1 + e\cos\nu)^2}{p^{3/2}} \quad (3.16)$$

$$\dot{\Pi} = \frac{q}{m} B_0 \left[\frac{1}{e} \left(\frac{e^2 + 1}{p^{3/2}} - \frac{\omega_E}{\sqrt{\mu}} \right) \cos \nu + \frac{2}{p^{3/2}} \right] \frac{(1 + e \cos \nu)^2}{p^{3/2}} \quad (3.17)$$

represents a new set of relevant LAO perturbation equations cast in terms of true anomaly, eccentricity, and semi-latus rectum.

Adding to this set of perturbation equations is the Keplerian rate of change of true anomaly, recast with respect to p :

$$\dot{\nu} = \frac{\sqrt{\mu}(1 + e \cos \nu)^2}{p^{3/2}} \quad (3.18)$$

Equation 3.18 is substituted into the expression for time rate of change of orbit parameter given in Eq. 3.15, with the result

$$p^{1/2} \dot{p} = 2 \frac{q}{m} \frac{B_0}{\sqrt{\mu}} e \sin \nu \dot{\nu} \quad (3.19)$$

Following the above procedure of integrating the perturbation equations about an orbit gives an integral of

$$\int_{p_0}^{p_1} p^{1/2} dp = 2 \frac{q}{m} \frac{B_0}{\sqrt{\mu}} e \int_0^\pi \sin \nu d\nu \quad (3.20)$$

The limits of integration for true anomaly are $\nu = 0$ to $\nu = \pi$. These limits correspond to a spacecraft that enters the Jovian SOI with no charge and remains free of charge until it reaches perijove. Once at perijove, the satellite turns on its charging mechanism. From perijove onwards, a negative charge on the satellite decreases p . The semi-latus rectum decreases until the orbit passes through unity eccentricity and becomes elliptical. We look only at cases in which the charge-to-mass ratio is sufficient to create an ellipse in one half orbit. The spacecraft is captured in only half an orbit, and the problem is symmetric with respect to the line of nodes. These facts allow the capture to be reversed in only half an orbit as well. If the charge is on from apojoive of the captured orbit until perijove, the

parameter and eccentricity return to exactly the same values as the initial Jovian hyperbolic orbit.

Figures 3.3 and 3.4 demonstrate these principles through simulation. Figure 3.3 shows the capture of a satellite by Lorentz propulsion. The left plot shows the spacecraft's trajectory through Jovian space. The satellite is initially on the Earth-Jupiter Hohmann ellipse, with a perijove of 1.05 Jovian radii. The right plot of Fig. 3.3 displays both the true anomaly of the satellite and its charge-to-mass ratio on one set of axes. The charge is initially zero on the hyperbolic entry and is then increased to -1.098 C/kg as the satellite passes through perijove. This charge causes energy to be removed from the satellite's orbit. The charge then remains constant through the resulting elliptical orbit. The trajectory plot also clearly shows the rotation of the longitude of periapsis caused by the constant charge. Figure 3.4 shows the eventual escape of the same spacecraft. The charge is initially at the negative value of -1.098 C/kg. Then, as the satellite passes perijove, the charge is set to zero, allowing the vehicle to resume its initial hyperbolic orbit (albeit rotated through some angle).

Solving the integral in Eq. 3.20 gives a relationship between a charge applied from perijove to apojove and the final semi-latus rectum:

$$\frac{q}{m} = \frac{1}{6} \frac{(p_1^{3/2} - p_0^{3/2})\sqrt{\mu}}{B_0 e_0} \quad (3.21)$$

where p_0 is the parameter of the initial hyperbolic orbit and p_1 represents the final elliptical orbit. Unlike the semimajor axis, p varies smoothly through the transition between hyperbolic, parabolic, and elliptical orbits.

Using the parameter p instead of semimajor axis simplifies many of the perturbation equations. However, the semimajor axis is often the quantity of most interest in capture problems. Defining a not only sets the size of the orbit, but

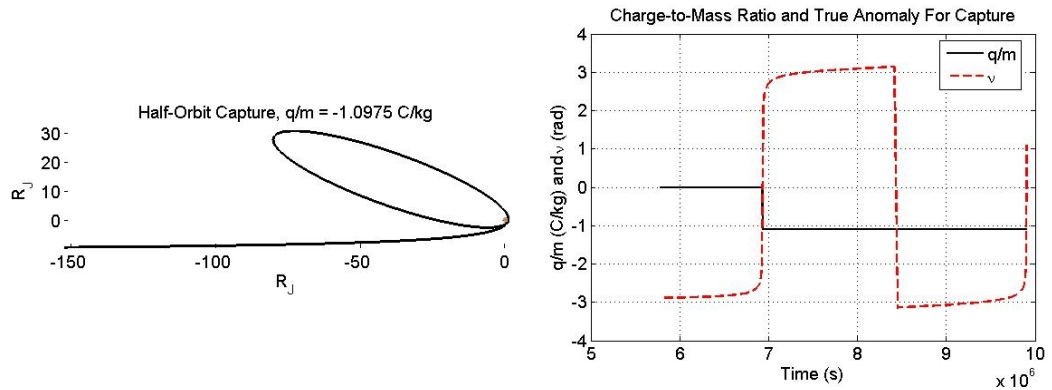


Figure 3.3: Capture of an LAO spacecraft in one half-orbit. The left figure displays the orbital track of the satellite. The right figure shows both the true anomaly of the spacecraft and the spacecraft charge. The charge is turned on as the spacecraft passes through perijove and remains on as it is captured.

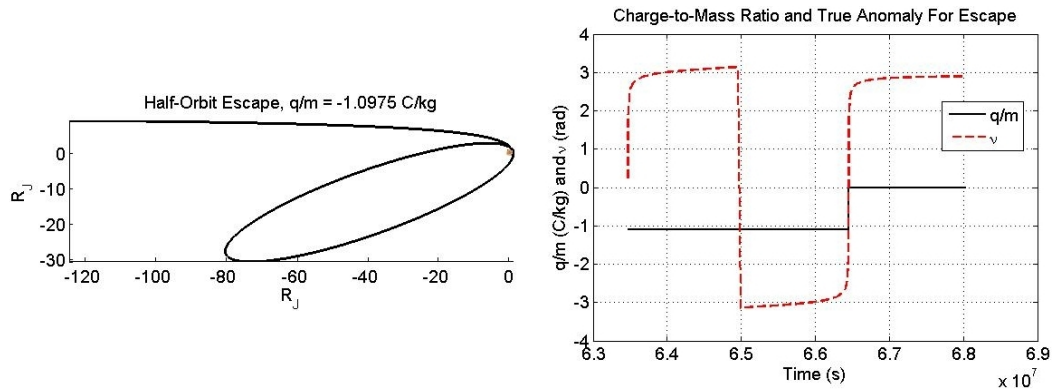


Figure 3.4: Escape of an LAO spacecraft in one half-orbit. The left figure displays the orbital track of the satellite. The right figure shows both the true anomaly of the spacecraft and the spacecraft charge. The charge is initially on and is then turned off as the spacecraft passes through perijove.

also its period. Knowing the period of the captured orbit becomes important as we attempt to shape a flyby.

We can find how the energy (and thus the semimajor axis) change as p changes. While a particular parameter p can correspond to many different values of semimajor axis and eccentricity, the Lorentz force only changes the quantities in a specific, related way. The particular nature of the Lorentz force causes the spacecraft to follow only certain trajectories in the state-space plane defined by p and E . We use our perturbation equations to solve for these $p - E$ trajectories based on the satellite's initial orbit. First, recall the LAO perturbation to energy, recast in terms of p :

$$\dot{E} = \frac{q}{m} \omega_E B_0 \frac{e}{p} \sin \nu \dot{\nu} \quad (3.22)$$

Recognizing and equating the similar terms in Eq. 3.22 and the derivative of p given in Eq. 3.15 yields an equation relating changes in semi-latus rectum to changes in orbital energy:

$$\dot{p} = \frac{2}{\omega_E \sqrt{\mu}} p^{1/2} \dot{E} \quad (3.23)$$

Equation 3.23 defines a certain trajectory in $p-E$ space; it is a separable differential equation and can be solved. Energy is used rather than semimajor axis because, like p , E varies smoothly across the hyperbolic-elliptical transition. Separating and integrating gives

$$p_1 = \left[\frac{1}{\omega_E \sqrt{\mu}} (E_1 - E_0) + p_0^{1/2} \right]^2 \quad (3.24)$$

where E_0 and E_1 refer to the initial hyperbolic and final elliptical orbits respectively. Semimajor axis can now be substituted for orbital energy, giving

$$p_1 = \left[\frac{-\sqrt{\mu}}{2\omega_E} \left(\frac{1}{a_1} - \frac{1}{a_0} \right) + p_0^{1/2} \right]^2 \quad (3.25)$$

where the 0 and 1 subscripts are as above. Equation 3.25 now allows us to specify a final semimajor axis, a_1 , for the captured orbit. Specifying a_1 in turn defines the

final desired semi-latus rectum p_1 . This parameter value is then used in Eq. 3.21, which gives a $\frac{q}{m}$ that results in the desired final orbit size.

3.2.3 Flyby Shaping Using a Temporary Jovian Capture

Two methods are examined for augmenting a gravity-assist maneuver with a temporary capture at Jupiter. In the first case, a captured satellite simply waits in a stable parking orbit for a specified time period. During the wait, the orbital motion of Jupiter causes the exit heliocentric of the spacecraft to be different than otherwise possible. The second method involves active specification of the outbound orbit. The spacecraft is captured and then uses a constant charge to change its perijove location. This perijove rotation enables an arbitrary exit direction from the planet and much more flexibility in designing the heliocentric Δv achieved by the satellite.

The simplest application of a temporary LAO capture at Jupiter is a timing maneuver. A spacecraft enters the Jovian SOI on a hyperbolic trajectory and is captured by turning on its charge-building mechanism at perijove as described above. As the satellite reaches the apojove of its new elliptical orbit, the excess charge is removed. The spacecraft is in a stable elliptical orbit. With zero net charge on the satellite, this elliptical orbit remains unchanged.

The goal of such a capture is to create more favorable timing for a flyby maneuver. This wait at Jupiter can extend or create new launch windows or create a more favorable geometry for reaching potential targets. A satellite can leave Earth when Jupiter is in a favorable position for rendezvous, and then hold at Jupiter until the best time for leaving Jupiter for the eventual target. This method could

potentially open many new mission windows, as instead of waiting for a relatively rare alignment of Earth-Jupiter-Target, the spacecraft can be launched at any Earth-Jupiter alignment (which occurs every 1.093 years)[53]. When the mission calls for the spacecraft to leave the vicinity of Jupiter, a charge of the same magnitude as the capture maneuver is turned on at apojove of the ellipse. By perijove, the satellite has regained energy such that it is in its original hyperbolic orbit. The charge is turned off and the spacecraft escapes. The maneuver can be timed easily by choosing an elliptical orbit whose period is an integer divisor of the desired waiting time.

In addition to merely timing a flyby, a temporary capture at Jupiter can provide greater freedom in designing a gravity assist. Instead of waiting in a static ellipse during the timing maneuver, the Lorentz force is used to evolve the ellipse. By correctly choosing the magnitude of a constant charge, an arbitrary exit angle from Jupiter's SOI is achieved. Obtaining an arbitrary exit allows for the full range of ΔV possibilities of the flyby to be used. In Fig. 3.1, the dotted lines show a possible LAO trajectory where the maximum magnitude of ΔV , without changing the magnitude of v_{out} , is obtained. The change in velocity can range anywhere from $\Delta V = 0$ to $\Delta V = 2v_{\infty}$.

One way to accomplish an arbitrary exit angle is to use a large enough charge that the spacecraft goes from the hyperbolic entrance trajectory all the way to a circular orbit. This effect is achieved 'instantaneously' at perijove of the hyperbola. As the satellite is in an equatorial orbit, moving purely tangentially to Jupiter, the Lorentz force on it is purely radial in direction. This radial force can cancel or augment the gravitational force such that satellite continues to move in circular orbit until the charge is turned off. Once the charge is turned off, the satellite

resumes its previous hyperbolic orbit, escaping the system. Peck[3] gives a more in-depth discussion of this type of maneuver.

While the straight-to-circle maneuver is simple, the magnitude of charge-to-mass ratios it requires is infeasible. A method requiring less charge to complete the same maneuver is a temporary capture into an elliptical orbit, followed by successive changes in longitude of perijove. As perijove rotates, the exit asymptote of the escape hyperbola rotates as well. A careful choice of the capture ellipse properties allows a constant charge to be found that both captures the satellite and rotates the exit angle through a desired value in an integer number of orbits. This process is depicted in Fig. 3.5, which shows the four stages of the capture and precess scenario: First, the spacecraft enters the Jovian SOI on a hyperbolic trajectory with zero charge until perijove. Second, the increased charge causes the capture of the satellite into a closed orbit. Third, the constant charge on the satellite causes the captured orbit to precess. Fourth, the charge is removed at a subsequent perijove, enable the spacecraft to escape once again.

To solve for this required charge-to-mass ratio, we define an angle γ as the angle between the incoming asymptote of the hyperbola and the desired outgoing asymptote. This angle is between the actual asymptotes, not the v_{in} and v_{out} velocity vectors. Thus, a value of $\gamma = 2\pi$ represents an outgoing hyperbolic leg that is exactly antiparallel to the incoming orbit. This value of γ maximizes the magnitude of the ΔV for the flyby maneuver. An angle of $\gamma = \pi$ represents the minimum magnitude of ΔV , with the satellite exiting along a path exactly parallel to its inbound trajectory, causing the overall change in velocity to be zero.

With a given γ , it is not possible in general to specify the exact amount of time in which the arbitrary exit angle maneuver happens. Forcing both a constant

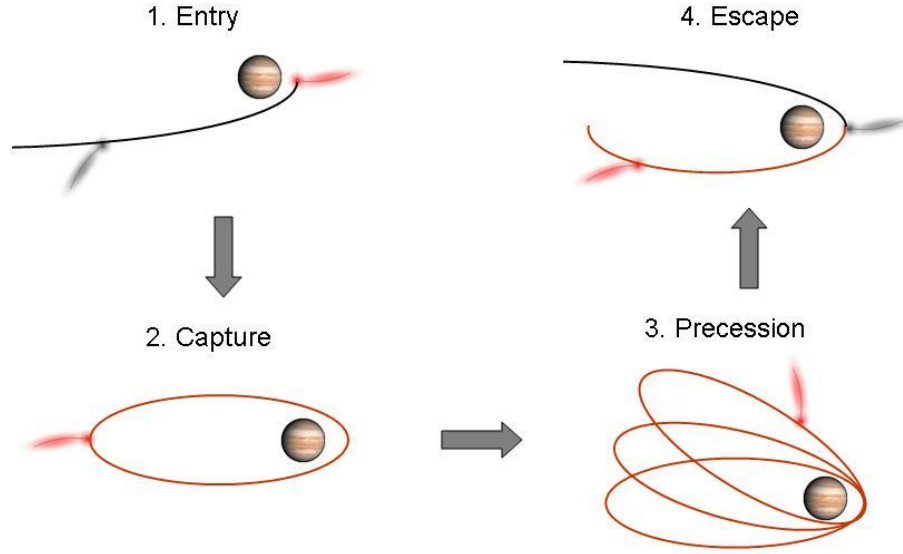


Figure 3.5: The four stages of the capture and precess scenario.

charge and an integer number of orbits for the rotation places too many constraints on the problem. In the solution presented here a maximum time for the maneuver to happen, t_{max} , is specified and then the solution closest to that amount of time is solved for. In general, the longer the maneuver, the higher the number of orbits, N , and the lower the charge-to-mass ratio required. To find the best solution, a initial guess of N is used to find a solution that is iterated to find the largest permissible N .

To complete a rotation through γ in N orbits, an average change in longitude of periapsis of

$$\dot{\Pi}_{avg} = \frac{\gamma - (\pi - \delta)}{N \cdot 2\pi \sqrt{\frac{a_1^3}{\mu}}} \quad (3.26)$$

is required, where a_1 is semimajor axis of the capture ellipse. This periapsis change rate is used in

$$\frac{q}{m} = \frac{\dot{\Pi}_{des} a^{3/2} p^{3/2}}{2B_0} \quad (3.27)$$

which is the perturbation solution charge-to-mass ratio required for an average rate of change of periapsis through an elliptical orbit. However, a_1 is currently unknown, but we can equate the expressions for charge-to-mass ratio for both capture and rotation as

$$\left(\frac{q}{m}\right)_{\Delta\Pi} = \left(\frac{q}{m}\right)_{\Delta p} \quad (3.28)$$

where $\left(\frac{q}{m}\right)_{\Delta\Pi}$ is taken from Eq. 3.27 and $\left(\frac{q}{m}\right)_{\Delta p}$ is from Eq. 3.21. Combining these two expressions and using Eq. 3.25 gives

$$\left(\dot{\Pi}_{des}a_1^{3/2} - \frac{\sqrt{\mu}}{3e_0}\right) \left[\frac{-\sqrt{\mu}}{2\omega_E} \left(\frac{1}{a_1} - \frac{1}{a_0}\right) + p_0^{1/2}\right]^3 + \frac{\sqrt{\mu}}{3e_0}p_0^{3/2} = 0 \quad (3.29)$$

where $\dot{\Pi}_{des}$ is given in Eq. 3.26. For a given γ and N , Eq. 3.29 gives the perturbation solution to the temporary capture with arbitrary rotation problem. Solving this equation for a_1 gives the size of the capture ellipse, which sets the $\frac{q}{m}$ required. The specified charge is turned on at perijove of the initial hyperbola. The spacecraft is then captured to an ellipse. As the constant charge remains on, the elliptical orbit rotates. After exactly N orbits the charge is removed allowing the spacecraft to reenter its initial hyperbolic orbit. However, this orbit has been rotated such that the exit asymptote of the hyperbola is an angle γ away from the inbound half of the orbit.

An algorithm for the solving the maximum time problem presented above is as follows:

1. Define maximum maneuver time t_{max}
2. Define outgoing angle γ
3. Set $N = 1$
4. Solve Eq. 3.29 to find a_1 and thus the required $\frac{q}{m}$
5. Return to Step 3 and increment N until $N \cdot 2\pi\sqrt{\frac{a_1^3}{\mu}} > t_{max}$

This algorithm represents the perturbation solution for this problem. But, as discussed above, perturbation methods have several inaccuracies that especially apparent under hyperbolic LAOs. In the case of the temporary capture, arbitrary exit problem, these perturbation errors compound through both inaccurate capture and inaccurate rotation expressions that propagate through several orbits, leading to large errors over the course of the maneuver. These errors make the perturbation solution impractical. So, we develop a numerical solution that uses the perturbation solution as an initial guess.

A numerical solution of the arbitrary exit problem requires a set of equations for the change in orbital elements due to the Lorentz force is required. While Eqs. 3.15, 3.16, and 3.17 are quite accurate, the assumptions made in order to analytically manipulate them introduce errors. These three equations can be numerically integrated with respect to true anomaly for an accurate depiction of an LAO. However, the Lorentz force causes changes in the true anomaly, ν . These changes are especially important in a hyperbolic or high-eccentricity elliptical orbits. In these orbits, the true anomaly changes slowly away from periapsis and then rapidly near periapsis. In these periods of rapid changes, small errors in the assumed Keplerian time rate of change of true anomaly result in large errors in the actual angle. Here we derive a perturbation expression for the rate of true anomaly change. This expression, when combined with the set of other perturbation solutions, creates a much more accurate system describing the effects of the Lorentz forces on a satellite.

An expression for true anomaly is obtained from the standard equation for radius of a conic section orbit:

$$\cos \nu = \frac{1}{e} \left(\frac{p}{r} - 1 \right) \quad (3.30)$$

In the absence of all perturbative forces, the derivative of Eq. 3.30 yields the standard derivative of true anomaly given in Eq. 3.10, where p and e are constants, and \dot{r} is known from conservation of angular momentum. Once the perturbation force is taken into account, \dot{p} and \dot{e} are no longer zero, and the derivative of Eq. 3.30 is

$$\sin \nu \dot{\nu} = \frac{p}{er^2} \dot{r} - \frac{\dot{p}}{er} + \frac{1}{e^2} \left(\frac{p}{r} - 1 \right) \dot{e} \quad (3.31)$$

Equation 3.31 is valid for any perturbation, not solely the Lorentz force. For an LAO specifically, \dot{p} and \dot{e} are replaced by Eqs. 3.15 and 3.16, respectively. For an instantaneous application of the Lorentz force, \dot{r} does not change from its Keplerian value. Combining these expressions gives the time rate of change of true anomaly for a charged spacecraft:

$$\dot{\nu} = \left[\sqrt{\mu} - 2 \frac{q}{m} B_0 \frac{(1 + e \cos \nu)}{p^{3/2}} + \frac{q}{m} B_0 \left(\frac{\omega_E}{\sqrt{\mu}} - \frac{1 - e^2}{p^{3/2}} \right) \frac{\cos \nu}{e} \right] \frac{(1 + e \cos \nu)^2}{p^{3/2}} \quad (3.32)$$

The first term in brackets represents the Keplerian secular increase in ν . The second and third terms represent the fact that the true anomaly changes when semi-latus rectum and orbital eccentricity change.

With Eqs. 3.15, 3.16, and 3.17, Eq. 3.32 completes a full set of accurate differential equations for the temporary capture problem. (As the problem is restricted to the equatorial plane, inclination and right ascension can be ignored.) With this set of equations a numerical algorithm is developed to solve the problem. This algorithm is mainly an extension of the perturbation method of above and is as follows:

1. Define maximum maneuver time t_{max}
2. Define outgoing angle γ

3. Set $N = 1$
4. Solve Eq. 3.29 to find an initial guess for a_1
5. Solve (by repeated numerical integrations) for the $\frac{q}{m}$ that gives exactly a_1 (at apojoive) for the captured ellipse
6. Check (numerically) what rate of longitude of periapsis change this $\frac{q}{m}$ gives. If this rate is not equal to the desired rate, go to Step 4 and adjust the guess for a_1 until $\dot{\Pi}_{actual} - \dot{\Pi}_{des} = 0$
7. Return to Step 3 and increment N until $N \cdot 2\pi \sqrt{\frac{a_1^3}{\mu}} > t_{max}$

This algorithm solves the arbitrary exit angle by temporary capture problem quite accurately. Figure 3.6 shows an orbital trajectory solved for using this algorithm, with $\gamma = 2\pi$ and $N = 20$. This simulation uses all the same initial conditions as those above. The spacecraft enters Jupiter's sphere of influence on a Hohmann trajectory from Earth with a perijove of 1.05 Jovian radii. The charge on the satellite is zero until it reaches perijove of the initial hyperbolic orbit. The spacecraft's charge is then brought up to -1.098 C/kg, and held constant. This charge captures the satellite and then rotates the resulting ellipse through 20 full orbits. After exactly 20 orbits the charge is removed, allowing the spacecraft to return to a hyperbola, exiting the Jovian SOI in exactly the opposite direction as its entrance. This time history of charge-to-mass ratio is shown in Fig. 3.7.

Figure 3.8 shows the orbital eccentricity of the spacecraft throughout the maneuver. This figure reveals the nature of the captured orbit. Shown on the figure is a dotted line representing an eccentricity of 1, which separates elliptical from hyperbolic orbits. Initially, the spacecraft is in a hyperbolic orbit, with eccentricity greater than one. When the charge is turned on, e begins dropping sharply. Before the spacecraft can leave the Jovian SOI, the eccentricity drops below 1, showing

that the satellite is now in a captured, elliptical orbit. As the spacecraft passes through apojoive, e begins to increase again until, at perijove, it has reached its initial hyperbolic value. In an osculating sense, the satellite is in a hyperbolic orbit at perijove, but, as long as the charge remains on, the spacecraft continues on a non-Keplerian, but closed, orbit. After the prescribed number of orbits, the charge is returned to zero. The osculating orbit becomes the true orbit, and the satellite escapes.

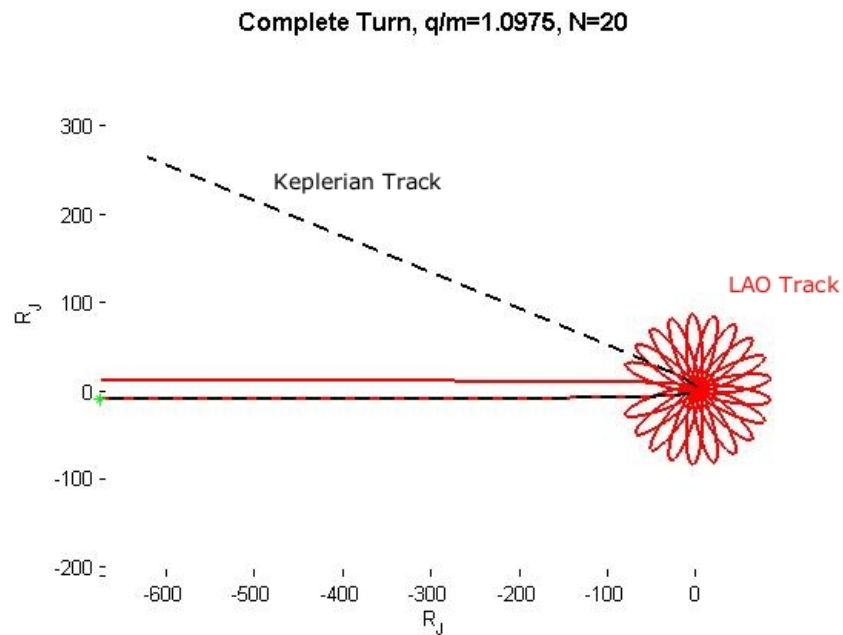


Figure 3.6: Arbitrary exit flyby trajectory. The chosen exit angle is 2π , or exactly opposite of the entrance angle. The number of elliptical orbits is 20 and the charge-to-mass ratio is -1.098 C/kg.

The above simulation depicts about 849 days. The initial hyperbolic orbit with no temporary capture would last 321 days from entrance of Jupiter’s SOI to exit. Thus the maneuver itself adds 528 days to the Jovian flyby. In essence, time is traded for a more effective flyby using a smaller charge. While the single-pass method adds no time to the flyby, it uses a $\frac{q}{m}$ of -7.5 C/kg to rotate the orbit 30° .

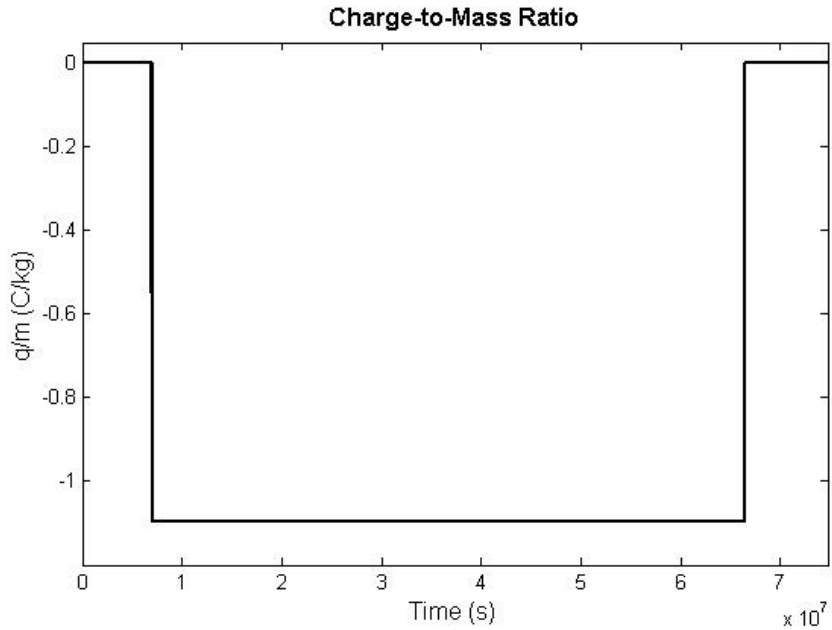


Figure 3.7: Arbitrary exit flyby charge-to-mass ratio. $\frac{q}{m}$ is initially 0 and then increases to -1.098 C/kg at the first perijove. The charge remains constant through all 20 orbits and goes to 0 at the final perijove.

The temporary capture adds 528 days, but can rotate orbit through a full 360° for only -1.01 C/kg. Generally the smallest $\frac{q}{m}$ values that allow for temporary capture are on the order of -1 C/kg (with maneuver time increasing greatly for small decreases in charge). Although the temporary capture method can add significant time to a flyby maneuver, this time may actually be beneficial to the mission, allowing for extended launch windows and additional science opportunities. This method is a powerful way to add flexibility and effectiveness to a flyby using a simple on-off charge on the satellite. More advanced charge modulation could extend the method even further.

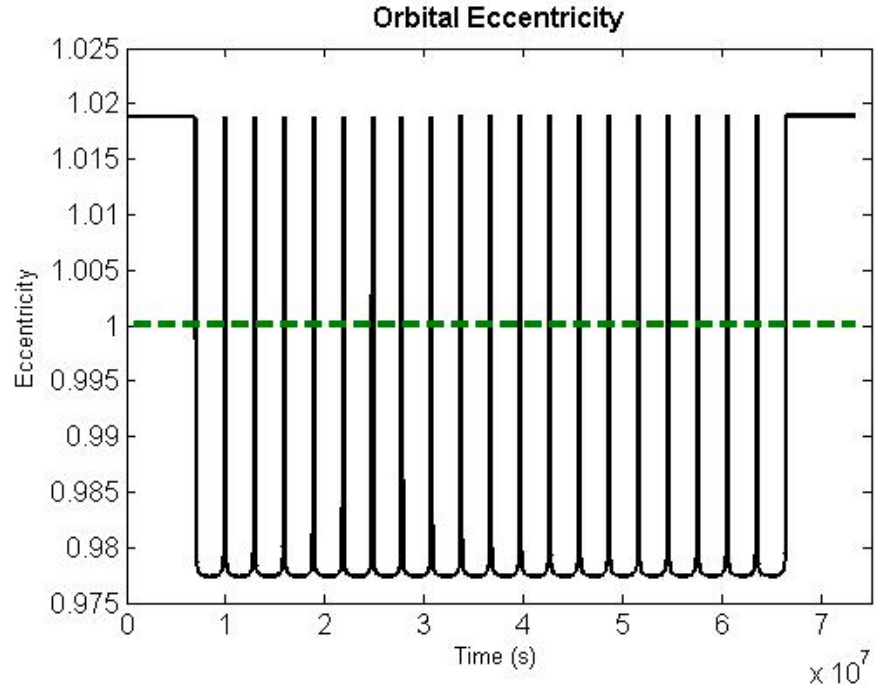


Figure 3.8: Arbitrary exit flyby orbital eccentricity. The eccentricity is initially hyperbolic, but is reduced to an elliptical value. Through each orbit e oscillates between values above one and below one, until the final escape.

3.3 Chapter Conclusions

The Lorentz force can have valuable and significant effects on gravity-assist maneuvers without the expenditure of propellant. Either with a single pass or with a temporary capture at the flyby target, LAO-based propulsion can greatly change the exit characteristics and timing of a flyby. The effective ΔV of a gravity assist can be maximized (or minimized). Temporary capture allows for the duration of a maneuver to be arbitrarily extended, opening up longer and more flexible mission windows. These effects are derived analytically to provide insight, although solutions developed by integrating perturbation equations with an osculating element assumption prove to be quantitatively inaccurate.

CHAPTER 4

A GENERAL BANG-OFF CONTROL METHOD FOR LORENTZ AUGMENTED ORBITS

4.1 Introduction

Earlier chapters presented the dynamics of LAOs under simplified conditions, including greatly simplified magnetic field models. This chapter expands that analysis to include spherical-harmonic magnetic fields of arbitrary complexity.

This chapter generalizes earlier perturbation equations for easier analysis in spherical coordinates. The spherical harmonic magnetic field model is then used to partition the space of latitude and longitude for easier control synthesis. A discussion of implementing an LAO-capable spacecraft ensues, followed by a look at the maneuver limitations introduced by the Lorentz force. A compelling mission enabled by the LAO concept is presented. The effects of ionospheric conditions on performance and power usage are considered.

4.1.1 Lorentz Perturbations in Spherical Coordinates

We have previously shown that the change in orbital energy, E , of a charged spacecraft affected by an arbitrary magnetic field is given by

$$\dot{E} = \frac{q}{m} \omega_E [(\mathbf{v} \cdot \hat{\mathbf{n}})(\mathbf{B} \cdot \mathbf{r}) - (\mathbf{v} \cdot \mathbf{r})(\hat{\mathbf{n}} \cdot \mathbf{B})] \quad (1.27)$$

To describe this position, \mathbf{r} , and velocity, \mathbf{v} , we use an Earth-centered, inertial reference frame with spherical coordinates: radius r , colatitude ϕ , and azimuth

angle θ , as shown in Fig. 1.1. In these coordinates, Eq. 1.27 can be expressed as

$$\dot{E} = \frac{q}{m} \omega_E \left[(r\mathbf{v} \cdot \hat{\mathbf{n}} - \cos \phi \mathbf{r} \cdot \mathbf{v})(\mathbf{B} \cdot \hat{\mathbf{r}}) + \sin \phi (\mathbf{r} \cdot \mathbf{v})(\mathbf{B} \cdot \hat{\phi}) \right] \quad (4.1)$$

The $\hat{\mathbf{r}}$ and $\hat{\phi}$ unit vectors are shown in Fig. 1.1.

The change in vector angular momentum was also previously found from perturbation methods:

$$\dot{\mathbf{h}} = \frac{q}{m} (\mathbf{B} \cdot \mathbf{r}) \mathbf{v} - \frac{q}{m} (\mathbf{r} \cdot \mathbf{v}) \mathbf{B} - \frac{q}{m} \omega_E (\mathbf{B} \cdot \mathbf{r}) (\hat{\mathbf{n}} \times \mathbf{r}) \quad (1.30)$$

In the spherical coordinates, the change in inclination can be written as

$$\begin{aligned} \frac{di}{dt} = & \frac{-1}{h\omega_E \sin i} \dot{E} + \frac{q}{m} \frac{\cos i}{h^2 \sin i} \left[\omega_E r^2 (r\mathbf{v} \cdot \hat{\mathbf{n}} - \cos \phi \mathbf{r} \cdot \mathbf{v})(\mathbf{B} \cdot \hat{\mathbf{r}}) \right. \\ & \left. + \frac{h \cos i}{\sin \phi} (\mathbf{r} \cdot \mathbf{v})(\mathbf{B} \cdot \hat{\phi}) + h \sin i \cos(\theta - \Omega) (\mathbf{r} \cdot \mathbf{v})(\mathbf{B} \cdot \hat{\theta}) \right] \end{aligned} \quad (4.2)$$

The first term in Eq. 4.2 shows that changes in inclination are coupled to changes in orbital energy, especially for orbits that are near circular (where $\mathbf{r} \cdot \mathbf{v}$ goes to zero) or polar (where $\cos i$ goes to zero). This coupling does not rise from some fundamental relationship between energy change and inclination change, but rather from the particulars of the Lorentz force. The energy change is driven by the radial component of the magnetic field and the apparent velocity induced by the rotation of the field. The inclination change is generally driven by the radial component of the magnetic field and the in-track velocity of the spacecraft. These velocities, magnetic field components, and perturbation equations happen to line up such that they depend upon the same dynamic quantities in the same relationships.

An expression for the change in eccentricity, e , is

$$\dot{e} = \left[\frac{a}{\mu} (1 - e^2) \right]^{1/2} \left\{ (\mathbf{F}_{\mathbf{L}} \cdot \hat{\mathbf{r}}) \sin \nu + [\mathbf{F}_{\mathbf{L}} \cdot (\hat{\mathbf{h}} \times \hat{\mathbf{r}})] \left(\cos \nu + \frac{e + \cos \nu}{1 + e \cos \nu} \right) \right\} \quad (4.3)$$

This expression makes use of the Lorentz force, $\mathbf{F}_{\mathbf{L}}$, explicitly. The Lorentz force is not broken into spherical harmonics here for the sake of brevity.

Equations 4.1, 1.30, 4.2, and 4.3 are greatly simplified if we restrict our discussion to circular (or near circular) orbits, where the term $(\mathbf{r} \cdot \mathbf{v})$ vanishes. Applying this simplification to Eq. 4.1 yields

$$\dot{E} = \frac{q}{m} \omega_E \sqrt{\frac{\mu}{r^3}} \sin i \cos u (\mathbf{B} \cdot \hat{\mathbf{r}}) \quad (4.4)$$

The argument of latitude is defined as the angle from the point of right ascension of the ascending node (RAAN) to the spacecraft's position, measured around the orbit. Only the radial component of the magnetic field affects the orbital energy of a circular LAO. If the same simplification is applied to Eq. 1.30, we find that the change in scalar angular momentum is simply a multiple of the change in energy:

$$\dot{h} = \sqrt{\frac{r^3}{\mu}} \dot{E} \quad (4.5)$$

The inclination change in a circular orbit follows the same pattern:

$$\frac{di}{dt} = \frac{\frac{\omega_E r^2}{h} \cos i - 1}{h \omega_E \sin i} \dot{E} \quad (4.6)$$

Equation 4.6 implies that, in circular orbits, orbital energy and inclination are not independently controllable with the Lorentz force. For every increase in energy, there is a corresponding decrease in inclination. (This fact also holds true for any polar orbit, eccentric or not.) This correlation limits the maneuvers that can be performed with LAO-based propulsion.

The circular-orbit assumption simplifies Eq. 4.3, resulting in

$$\begin{aligned} \dot{e} = & \frac{q}{m} \frac{h}{\mu} \left\{ 2 \frac{\omega_E}{h} \sqrt{\frac{a}{\mu}} r^2 \sin i \cos(\theta - \Omega) \sin \phi \cos \nu (\mathbf{B} \cdot \hat{\mathbf{r}}) \right. \\ & + \sin \nu \left(\omega_E r \sin \phi - \frac{h \cos i}{r \sin \phi} \right) (\mathbf{B} \cdot \hat{\phi}) \\ & \left. - \frac{h}{r} \sin i \cos(\theta - \Omega) \sin \nu (\mathbf{B} \cdot \hat{\theta}) \right\} \quad (4.7) \end{aligned}$$

The change in eccentricity depends on all three components of the magnetic field, making for more complicated analysis. Each term in Eq. 4.7 involves the true anomaly, ν . This relationship shows the importance of radial velocity, which is also explicitly related to ν . Changes in eccentricity are driven by small deviations from the circular-orbit assumption.

4.1.2 Partitioning The Geomagnetic Field

In this chapter, earlier assumptions about the structure of the Earth's magnetic field are relaxed. The simple non-tilted and tilted dipole models fail to account for the fact that terms higher in degree than the dipole are significant components of the field. Here, a full spherical harmonic model is used: the International Geomagnetic Reference Field,[5] in particular, the IGRF95 (or IGRF-7) model. All simulations in this chapter use coefficients up to 10th degree and order.

The effect of the Lorentz force on an orbit is conveniently broken up into the components of the magnetic field in spherical-coordinate unit vectors: the radial direction $\hat{\mathbf{r}}$, the colatitude direction $\hat{\phi}$, and the azimuthal direction $\hat{\theta}$, as seen in Section 4.1.1. The magnetic field, \mathbf{B} , is studied as the three components $(\mathbf{B} \cdot \hat{\mathbf{r}})$, $(\mathbf{B} \cdot \hat{\phi})$, and $(\mathbf{B} \cdot \hat{\theta})$. Contour plots and descriptions of these three components are given in Section 1.2.

The three orthogonal components of the field can be used to divide the space of latitude and longitude into eight distinct zones. The zones are defined by whether each component is positive or negative and are bounded by the zero contours depicted in Figs. 1.2, 1.3, and 1.4. The zones are numbered I-VIII and depicted graphically in Fig. 4.1 with properties shown in Table 4.1. Figure 4.1 shows each

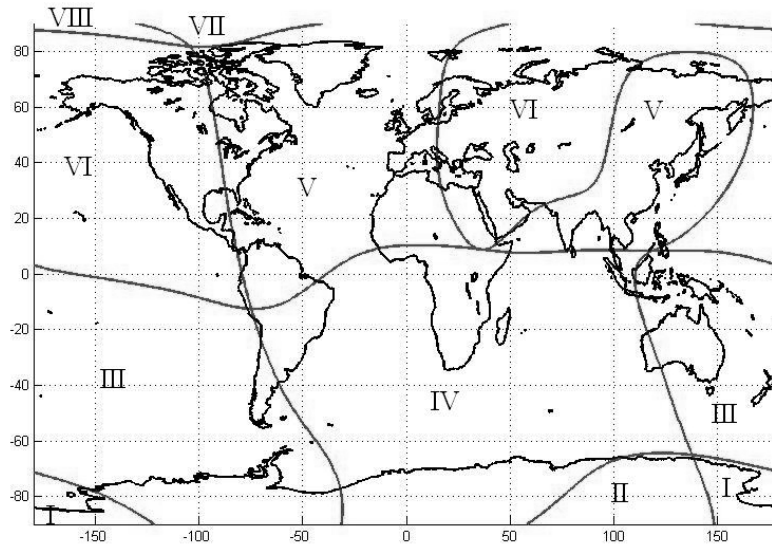


Figure 4.1: Eight distinct zones of the geomagnetic field, numbered I-VIII.

of the zones superimposed on a map of the Earth. Because of distortion due to the map projection, Zones I, II, VII, and VIII are shown larger than their actual sizes. In a three-dimensional view, they appear in a small region near each pole. The large southward swing of the zero-declination contour over eastern Africa actually crosses the magnetic equator, causing zones III and V to have non-contiguous regions. Table 4.1 lists the differences among the zones. A '+' in the table refers to a quantity greater than zero, while a '-' denotes less than zero.

In each zone, the geomagnetic field has a certain sign for a particular component of the field. Each zone creates different effects on the orbit of a charged satellite. We use these differences to create a control sequence to perform a desired maneuver. The zones are defined with respect to Earth-fixed latitude and longitude as the geomagnetic field rotates with the Earth. Figures 1.2-1.4 are for a representative altitude (600 km) because the relative strength of each order of field terms depends on altitude. While the actual zone boundaries depend on altitude, they are easily

Table 4.1: Zone Properties

Zone	$(\mathbf{B} \cdot \hat{\mathbf{r}})$	$(\mathbf{B} \cdot \hat{\phi})$	$(\mathbf{B} \cdot \hat{\theta})$
I	+	+	+
II	+	+	-
III	+	-	+
IV	+	-	-
V	-	-	-
VI	-	-	+
VII	-	+	-
VIII	-	+	+

calculated at any particular location by the simple sign definitions shown in Table 4.1.

4.2 Space Vehicle Design

This section offers a brief overview of possible architectures for LAO capable spacecraft, following the work of Streetman and Peck[15]. It considers three competing, interrelated parameters: capacitance, power, and space-vehicle mass. There are also issues of implementation, such as deployability of the capacitor, technology readiness of the power system, thermal implications of high power, and interactions among various subsystems (notably attitude control). These issues are minimized here. For the present, maximizing the $\frac{q}{m}$ metric is taken to be the only goal of LAO space vehicle design. Furthermore, we consider this metric only in terms of a constant-mass spacecraft. Six hundred kilograms is chosen as a somewhat arbitrary

constraint for this mass optimization. The mass is given some contingency.

4.2.1 Capacitance

High $\frac{q}{m}$ implies high charge, which requires high capacitance. Known technologies for self-capacitance store charge on the surface of a conductor with no sharp local features or high curvature. So, a successful design realizes high surface area to volume in flat structures or long, thin ones. Such a capacitor likely encounters a limit associated with the minimum thickness of thin films or the minimum feasible diameter of long filaments. That limit ultimately leads to a minimum mass for the capacitor. The capacitor is also designed to exploit plasma interactions. Based on work by Choinière and Gilchrist[36], we have baselined a cylindrical capacitor constructed of a sparse wire mesh. This stocking-like arrangement of appropriately spaced thin wires develops a plasma sheath due to ionospheric interactions that raises the capacitance of the cylinder well above what it would be in a pure vacuum. We emphasize that such self capacitance is not available from off-the-shelf electronics components, which merely hold equal amounts of positive and negative charge.

In this model, the capacitance C is taken to be that of a solid cylinder of the stocking’s radius R but with a concentric shell (due to the plasma sheath) equal to the thickness of an individual wire’s sheath r_s :

$$C = \frac{2\pi\epsilon_0 L}{\log \frac{R+r_s}{R}} \quad (4.8)$$

where ϵ_0 is the permittivity of free space. The sheath radius increases with potential and is calculated as described by Choinière and Gilchrist[36]. In the architecture described in Section 4.2.2, R takes on values of tens to hundreds of

meters. The sheath thickness r_s depends on the temperature and density of the plasma and on capacitor potential, ranging from millimeters to meters in earth orbit. We space these wires so that one wire is a sheath's thickness away from its neighbor. This spacing ensures overlap between individual wires' sheaths but keeps the structure sparse. Occasional structural elements, such as thin conductive bands, would be necessary to maintain the spacing along the capacitor because of Coulomb repulsion that acts among the wires. This repulsion would also serve as a useful means for deploying the capacitor without heavy trusses or actuators. A schematic of this design is shown in Figure 4.2.

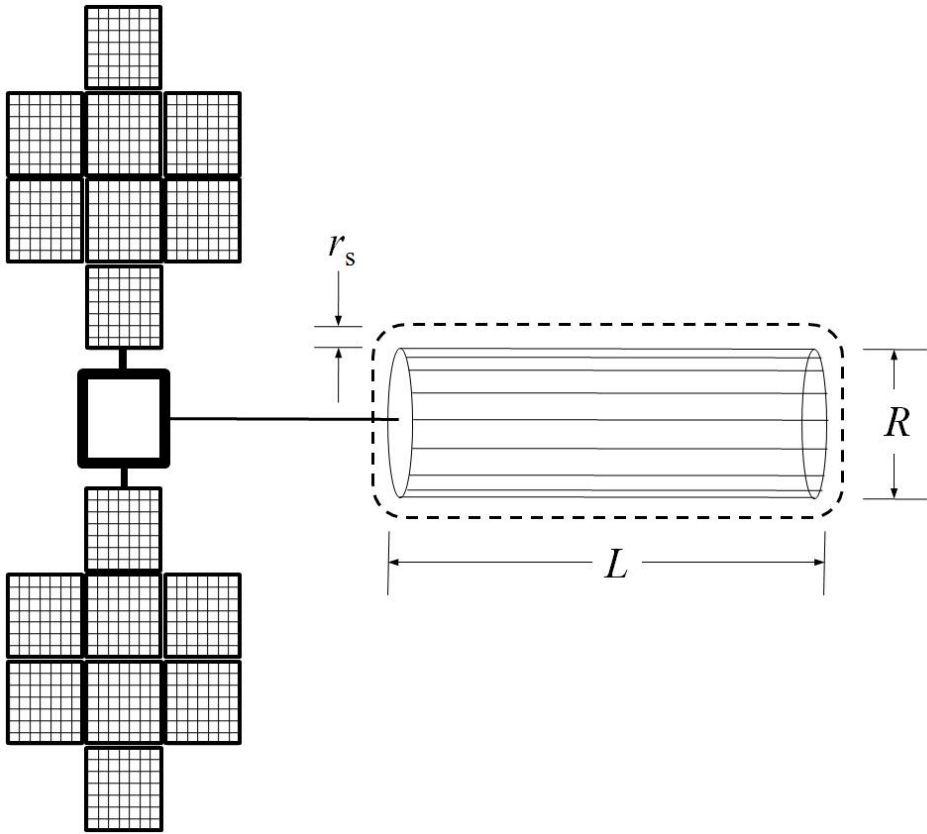


Figure 4.2: LAO spacecraft with cylindrical stocking capacitor. The dotted line surrounding the capacitor suggests the effective boundary of the plasma sheath.

4.2.2 Power

We consider two fundamentally different approaches to the power subsystem. The classical approach depends on solar power. Energy from solar panels is used directly to power the capacitor, countering the plasma currents, or is stored in batteries or some sort of efficient ultracapacitor to be used in a periodic-charging scheme. Some assumptions about the specific power (W/kg) must be made. Although the power density of current systems is about 40 W/kg[44], a farther-term power density of 130 W/kg, is used here, consistent with DARPA's FAST program.[55]

In the case of this solar-power approach, the charge is maintained by modifying the current collection scheme proposed by Sanmartin, et al[35]. A power supply on board the spacecraft establishes a potential between two conductive surfaces exposed to the plasma environment. The positive end attracts the highly mobile electrons, while the negative end attracts the far less mobile ions (such as O^+). The substantial imbalance in electron and ion currents leads the negative end to accumulate a nonzero charge while the positive end is almost electrically grounded in the plasma. So, with the wire capacitor on the negative end, the spacecraft would achieve a net charge roughly equal to the product of the capacitance of the wires and the potential across the power supply.[36] This charge is accomplished without the use of particle beams.

A more unusual approach exploits alpha-particle emission from an appropriate radioactive isotope[32], such as Po 210. These emissions are not converted to electrical power thermionically as in a radioisotope thermoelectric generator (RTG) or via fission in a nuclear reactor; instead, the isotope is spread thinly enough on the capacitor's surface that up to half of the emitted alpha particles carry charge away from the spacecraft. The electrical current of these particles is proportional

to their charge (2 positive fundamental charges), their kinetic energy (roughly 5.3×10^6 eV), and the isotope's decay rate. If the maximum potential can be achieved despite currents from the surrounding ionospheric plasma, this approach offers as much as 42 kW/kg of Po 210 after 1 year of alpha decay. Maintaining this charge requires no power supply. The spatially distributed nature of the current from the thin film suggests that the current does not approach any sort of beam-density limit due to space charge.

We focus on the prospects for the solar-panel approach because launching an isotope is likely to encounter a variety of technical and non-technical roadblocks. In all cases, the capacitor maintains negative charge. The ion currents are then given by the Orbit Motion Limited (OML) estimate[36]. We use the International Reference Ionosphere (IRI)[56] to provide the necessary plasma number density and temperature. We also account for the photoelectric current emitted from the surface of the conductive capacitor. In the case of the solar-panel approach, all of this power is subject to resistive losses as the power supply drives current through the many, thin wires. Assuming that the current is uniform to all parts of the capacitor, we average the losses along the length of wire that the current has to travel.

4.2.3 Space Vehicle Mass

The charge-to-mass ratio depends on the mass of the entire space vehicle. We model this mass coarsely, as the sum of discrete components with interrelated dependencies. Table 4.2 summarizes this mass model.

An example of the power calculation is shown in Table 4.3. Table 4.4 uses this

Table 4.2: Space Vehicle Mass Model

Subsystem or Component	Value	Units
Payload	50	kg
Bus (w/ payload power)	3.33	(kg bus) / (kg payload)
LAO Solar Power	130	W/kg of orbit-average power
LAO Isotope Power	42	kW/kg of Polonium after 1 year of decay
Power Mass Contingency	14	kg
Capacitor	$2700\pi R^2 n L$	kg for n aluminum wires of length L and radius R
Capacitor Mass Contingency	$1.1m$	kg, where m is the sum of the wires' masses

power calculation to arrive at the 600 kg space-vehicle mass requirement.

4.2.4 Performance Estimates

Figure 4.3 summarize the results of these calculations for a 600kg spacecraft that charges for 50% of the time over a 600km orbit. Figure 4.3 shows the FAST power design, which yields $\frac{q}{m} = 0.0070$ C/kg for a 20km stocking at 7kV potential. The efficiency (force per power) increases with lower potential. For example, the optimal value of 5 C in a 600km polar orbit produces about 2.3N, for 1.6×10^{-5} N/W when the capacitor is charged. However, at only 1kV, the resulting 3.1C represents 2×10^{-5} N/W. So, if the speed of the maneuver is unimportant, lower-

Table 4.3: Example of Power Calculation for A Spacecraft in a 600km Altitude LEO Circular Orbit at an Inclination of 28.5°

Parameter	Value	Units
Wire Material	Aluminum	
Wire Radius	5.00×10^{-6}	m
% Overlap Sheath Diameter	0%	
Length of Stocking (L)	20	km
Stocking Radius as a % of Stocking Length	5.00%	
Stocking Mass Sandbag	3	kg
Intermediate Calculation	Value	Units
Material Resistivity at 20°C	2.82×10^{-8}	Ω
Radius of Stocking (R)	1	km
Material Density of Wire	2700	kg/m ³
Sheath Thickness	1.764	m
Resistance per Wire	7.198	M Ω
Number of Wires	7142	
Mass of Stocking	30.36	kg
Mass of Capacitor	33.40	kg
Average Cylinder-as-body Capacitance (C)	6.00×10^{-4}	F
Result	Value	Units
Average Body Charge-to-Mass Ratio	-0.0070	C/kg
Exposed Wire Area	2548	m ²
Photoelectron Current	0.122	A
Orbit-Average Power Required (~50% duty cycle)	53.54	kW

Table 4.4: Example of Mass Calculation

Parameter	Value	Units
Potential	-7000	V
Orbit-Average Power for LAO	46.28	kW
LAO Power System Mass Dependency	130	W/kg
LAO Power System Mass	466	kg
Power System Mass Contingency	14	kg
Payload	20	kg
Bus Mass (including any propellant)	100	kg
Total Space Vehicle Mass	600	kg

potential designs may be better. As the capacitor potential increases beyond the optimum for $\frac{q}{m}$, more mass of the fixed 600kg must be devoted to the power subsystem, which comes at the expense of capacitor mass. The accuracy of these performance measures depends on the accuracy of the simplified sheath model and should eventually be verified by a more complex 2-D algorithm such as that developed by Choinière and Gilchrist[36].

4.3 LAO Maneuvers and Limitations

4.3.1 Maneuver Limitations

A Lorentz Augmented orbit cannot experience arbitrary changes for all initial orbital elements. In certain regimes, as evidenced by Eq. 4.6, changes in orbital elements are tightly coupled. This coupling stems from the basic physics of the

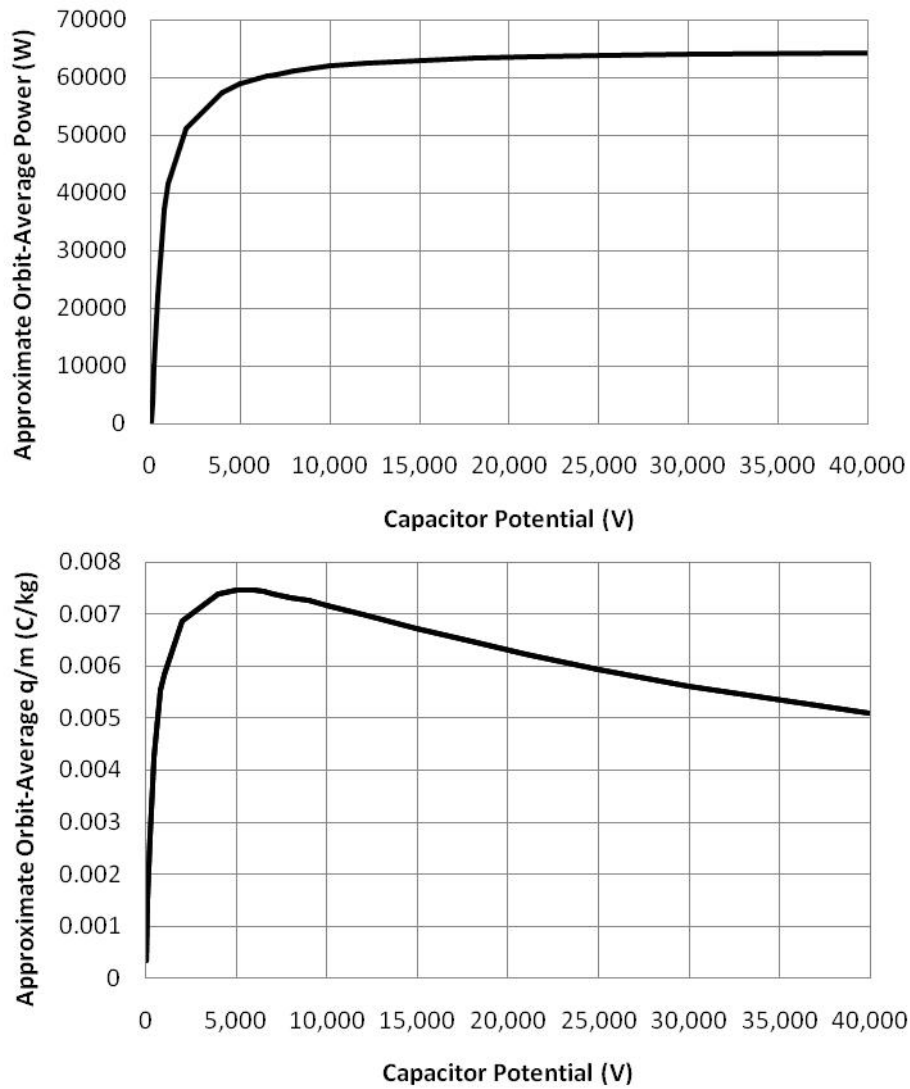


Figure 4.3: Orbit Average Power and $\frac{q}{m}$ vs. Capacitor Potential

Lorentz force. The direction of the force is set by the magnetic field and the velocity of the spacecraft with respect to that magnetic field, neither of which can be altered by the spacecraft control system.

A further limiting factor is that the best system architectures provide only one polarity of charge (negative). Because electrons in the ionosphere are far more mobile than ions, significantly less power is required to maintain a negative charge

than a positive charge. The single-polarity system limits what changes can be made to the RAAN, Ω , and the argument of perigee, ω . For a given charge polarity, Ω and ω evolve only in a single direction (in low Earth orbit). For a negative charge in LEO, Ω always decreases and ω always increases.

Table 4.5: LAO Effects for $\frac{q}{m} < 0$ in LEO

Element	Net Effect of Constant Charge	Signs of Possible Changes	Notes
a	0	+/-	a/i coupled for $e = 0$ or $i = 90^\circ$, $\dot{a} = 0$ for $i = 0^\circ$ and $e = 0$
e	0	+/-	$\dot{e} > 0$ for $e = 0$
i	0	+/-	a/i coupled for $e = 0$ or $i = 90^\circ$
Ω	-	-	Ω undefined for $i = 0^\circ$
ω	+	+	ω undefined for $i = 0^\circ$ and $e = 0$
ν	0	+/-	

Table 4.5 summarizes some of the abilities and limits of LAO propulsion for a single polarity of charge. The first column of the table shows the net effect of a constant charge on a spacecraft. The second column shows the available directions of change for each orbital element for a variable (but single-polarity) charge. The final column summarizes some of the special cases and coupling within the dynamics. Some of these special cases are addressed more explicitly in our earlier work.[12, 14]

The Lorentz force is at its strongest in LEO. The strength of the dipole component of the magnetic field drops off with the cube of radial distance. Additionally, spacecraft velocities with respect to the magnetic field tend to be larger in LEO.

A geostationary spacecraft has no velocity with respect to the magnetic field and thus experiences no Lorentz force.

4.3.2 Example Maneuver: LEO Inclination Change and Orbit Raising

The minimum inclination a spacecraft can be launched into is equal to the latitude of its launch site. For a United States launch, this minimum inclination is generally 28.5° , the latitude of Cape Canaveral, FL. However, for certain missions, equatorial orbits are desirable. The plane change between $i = 28.5^\circ$ and $i = 0^\circ$ is expensive in terms of ΔV and requires either a launch vehicle upper stage or a significant expenditure of spacecraft resources. We develop a control algorithm to use the Lorentz force to perform this inclination change without the use of propellant, while simultaneously raising the orbital altitude.

This maneuver is primarily concerned with inclination change in circular orbit. Equation 4.6 describes the relevant dynamics. As energy change and inclination change are coupled in this situation, Eq. 4.4 describes both the energy and plane changes. In this circular case, only the radial component of the magnetic field affects the energy and inclination. For the inclination to decrease, the energy must increase. With these facts, we develop a bang-off controller based upon the argument of latitude and the sign of the radial component of the field. Using $\frac{q}{m} < 0$, the term $\cos u(\mathbf{B} \cdot \hat{\mathbf{r}})$ must be negative. We know that $(\mathbf{B} \cdot \hat{\mathbf{r}})$ is positive below the magnetic equator (Zones I, II, III, and IV) and negative above the magnetic equator (Zones V, VI, VII, and VIII). Thus, for northward motion of the satellite ($\cos u > 0$), the charge should be nonzero within Zones V-VIII. For

southward satellite motion ($\cos u < 0$), nonzero charge is applied in Zones I-IV. In other words, the charge should be off for the first quadrant of the orbit, on for the second quadrant, off for the third, and on for the fourth. This control can be represented as

$$\frac{q}{m} = \begin{cases} -\left(\frac{q}{m}\right)_{max} & \text{if } \cos u > 0, (\mathbf{B} \cdot \hat{\mathbf{r}}) < 0 \\ 0 & \text{if } \cos u > 0, (\mathbf{B} \cdot \hat{\mathbf{r}}) > 0 \\ -\left(\frac{q}{m}\right)_{max} & \text{if } \cos u < 0, (\mathbf{B} \cdot \hat{\mathbf{r}}) > 0 \\ 0 & \text{if } \cos u < 0, (\mathbf{B} \cdot \hat{\mathbf{r}}) < 0 \end{cases} \quad (4.9)$$

where $-\left(\frac{q}{m}\right)_{max}$ is largest available negative charge-to-mass ratio.

However, when this simple quadrant control is used, the eccentricity of the orbit tends to grow undesirably large. Maintaining an identically zero eccentricity is impossible, though. Any charge on a circular-orbiting spacecraft causes an increase in the eccentricity. However, if the oblateness of the Earth is considered, the eccentricity remains bounded by a small value. Figure 4.4 shows this result, plotting a short simulation of an orbit under the quadrant controller. The black line shows the growth of eccentricity with J2 absent, while the grey line shows the bounding of e under the influence of J2. The effect of J2 on the eccentricity of the orbit is larger than that of the Lorentz force. The J2 perturbation does not effect the overall performance of the maneuver, though. The Lorentz force depends on the velocity of the spacecraft which only changes by small amount due to presence of J2. The presence of J2 only creates a small periodic disturbance to both a and e .

The eccentricity can be kept using only charging means as well. Equation 4.7 implies that, as the orbit approaches equatorial, the term involving $(\mathbf{B} \cdot \hat{\phi})$ dominates the eccentricity increase. As $(\mathbf{B} \cdot \hat{\phi})$ is of a single sign for most latitudes

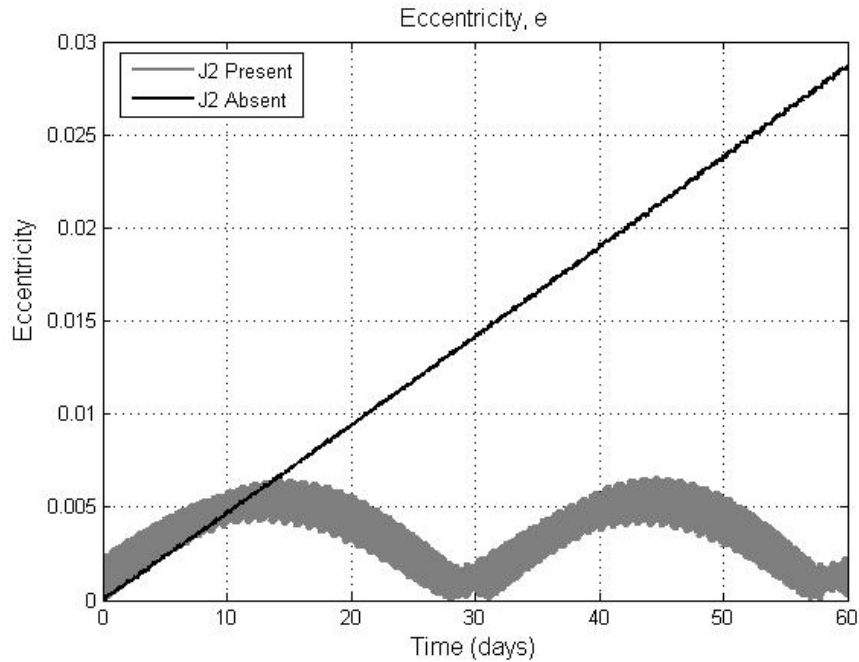


Figure 4.4: Effect of Earth oblateness on the eccentricity under the quadrant control.

(as Fig. 1.3 shows), the sign of this term corresponds to the sign of $\sin \nu$. In turn, the sign of $\sin \nu$ exactly follows the sign of the radial velocity, \dot{r} . For positive radial velocity (away from the center of the Earth) and negative charge, the eccentricity change is negative. For negative radial velocity and negative charge, the eccentricity change is positive. These two facts inspire a control algorithm that limits eccentricity growth. This e -limiting algorithm can be superimposed on the quadrant control described above. First a maximum desired eccentricity, e_{max} , is defined. When e_{max} is approached, charge is applied only if the radial velocity of the spacecraft is greater than zero, causing the eccentricity to decrease. With e now below e_{max} , the charge can be applied as required by the quadrant method until e_{max} is approached again. This e -limiting quadrant control offers performance in changing a and i that is close to, but less than, the performance of the unmodified control. However, for the rest of this chapter, the e -limiting controller will not be

used. Earth oblateness is relied on to keep the eccentricity small, as this results in no reduction in performance.

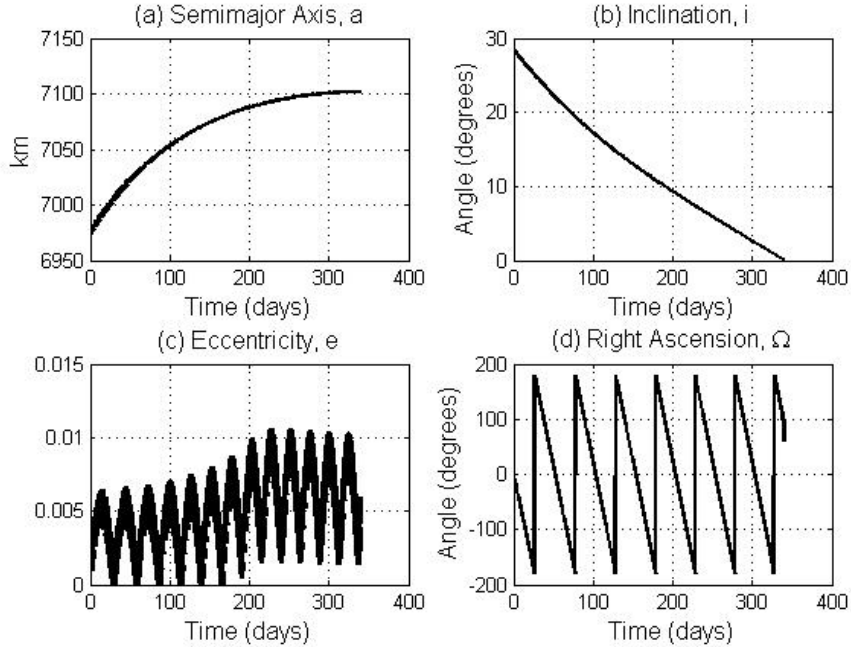


Figure 4.5: Orbital elements for the LEO plane-change and orbit-raising maneuver.

Figure 4.5 shows the results of a simulation using the e -limiting quadrant method. The simulation begins with a 600 km altitude circular orbit. The charge-to-mass ratio is $\frac{q}{m} = -0.007$ C/kg. A full model of J2 is used. The simulation lasts until an equatorial orbit is reached. The IGRF95 magnetic field model is used to 10th degree and order. In Fig. 4.5, plot (a) shows the increase in semimajor axis given by the quadrant method. The initial 600 km orbit is raised to a 724.0 km circular orbit, an increase of 124 km. Plot (b) shows the desired decrease in inclination. Since the magnetic equator does not align with the true equator, the inclination can be brought to exactly zero. Zero inclination is reached in about 340 days with this value of charge. Figure 4.5, plot (c), shows the eccentricity. The eccentricity is bounded by the J2 perturbation to a small value. Finally, Fig. 4.5,

plot (d), shows the RAAN. For a negative $\frac{q}{m}$ in LEO, the RAAN always decreases, however, in this simulation, the effect of J2 on RAAN dominates.

If the maneuver simulated above is performed using conventional impulsive thrust, it requires a ΔV of 3.75 km/s. Thus using LAOs could significantly increase the payload ratio of a spacecraft that needed such a maneuver. However, this mass savings comes at a cost of time spent, the mass of the capacitor and power system, and electrical power consumed during the maneuver.

Optimality of the Quadrant Bang-Off Controller

Bang-bang or bang-off controllers are generally Hamilton-Jacobi-Bellman optimal solutions[53]. They use the maximum capabilities of an actuator to achieve some goal. Here, we numerically verify that, for the simplified case of the non-tilted dipole field, the quadrant bang-off controller is the optimal way to decrease the inclination. Under the non-tilted field, there are only two zones: above the equator and below the equator. (For this field, the magnetic equator and true equator are the same.)

For a circular orbit in the non-tilted dipole field, the change in energy of the orbit due to the Lorentz force is given in Eq. 2.2. Using the relationship between energy and inclination change in Eq. 4.6, the inclination change in this case becomes

$$\frac{di}{dt} = 2B_0 \frac{\sqrt{\mu} \omega_E r^2 \cos i - h}{r^{5/2} h^2 \sin i} \sin u \cos u \frac{q}{m}(u) \quad (4.10)$$

where the charge-to-mass ratio has been made a function of the argument of latitude. Solving for Δi , the change in inclination per orbit, gives

$$\Delta i = 2B_0 \frac{1}{r} \frac{\omega_E r^2 \cos i - h}{h^2 \sin i} \int_0^{2\pi} \sin u \cos u \frac{q}{m}(u) du \quad (4.11)$$

With Eq. 4.11, we can set up an optimization problem to gain the most decrease in inclination per orbit:

$$\min \Delta i \text{ subject to } 0 \geq \frac{q}{m} \geq -\left(\frac{q}{m}\right)_{max} \quad (4.12)$$

Allowing Matlab's optimization routines to solve the problem in Eq. 4.12 gives the charge-to-mass ratio shown in Fig. 4.6. This figure shows $\frac{q}{m}$ on the y -axis and argument of latitude on the x -axis. Also shown are hatched regions showing where $(\mathbf{B} \cdot \hat{\mathbf{r}})$ (red hatching) and $\cos u$ (blue hatching) are greater than zero. As expected, the $\frac{q}{m}$ signal shows bang-off behavior, with switches at quadrant boundaries of u : 90, 180, 270, and 360 degrees. This result does not imply that quadrant controller is optimal for the spherical harmonic field, but it does show that quadrant control is optimal in at least some cases.

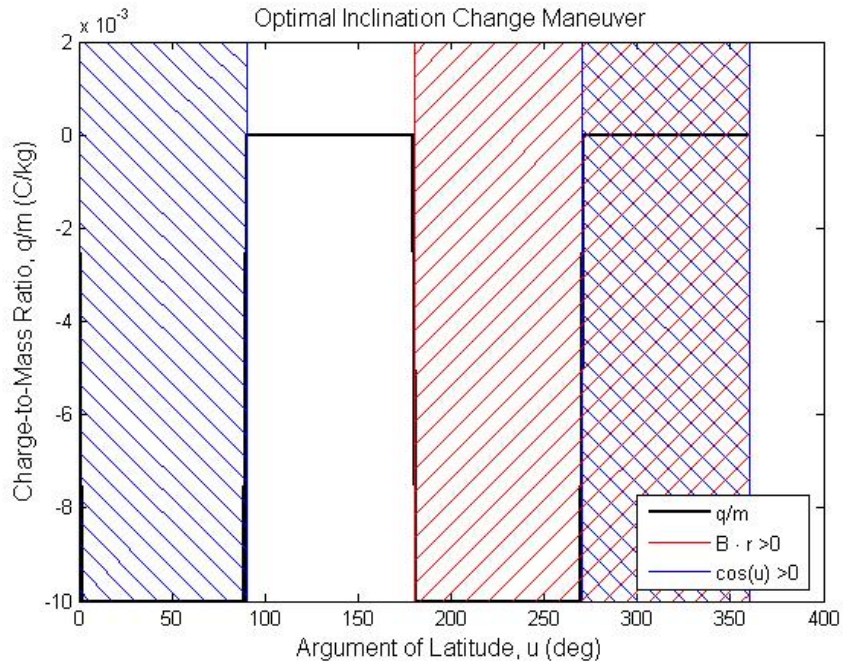


Figure 4.6: Optimal charge-to-mass ratio for inclination change.

4.3.3 Example Maneuver: GEO Transfer Inclination Change

Another commonly performed, expensive maneuver is the combined plane change/circularization of a geostationary transfer orbit (GTO) to a geosynchronous orbit. Again, a GEO satellite can be launched only into an orbit with inclination greater than or equal to the latitude of its launch site. The subsequent plane change is expensive to perform. We attempt to perform this inclination change using LAOs.

In the LEO plane-change maneuver discussed above, inclination change was maximized according to the constraint of keeping the eccentricity small. In the GTO maneuver, the initial orbit is highly eccentric. So, no consideration is placed upon eccentricity change. A simple control is used: charge is on whenever Eq. 4.2 is less than zero (to decrease inclination) and off otherwise.

The results of a one-year simulation using this controller are shown in Fig. 4.7. This simulation begins with a GTO orbit (apogee at GEO, perigee at 600 km altitude). Earth oblateness is not considered. The initial inclination is 28.5° . The charge-to-mass ratio is -0.007 C/kg. In Fig. 4.7, plot (a) shows the increase in semimajor axis that results from the coupling of inclination and energy changes. The semimajor axis grows by about 857 km. In the inclined GTO case, the energy change and inclination change are not exactly coupled as in the circular case, but they generally trend inversely. Plot (b) of Fig. 4.7 displays the desired inclination decrease. However, because the spacecraft spends much of its orbit far from the Earth, the change in inclination is much smaller than over the same time period in LEO. Over the course of one year, the inclination decreases only by 2.16° . Plot

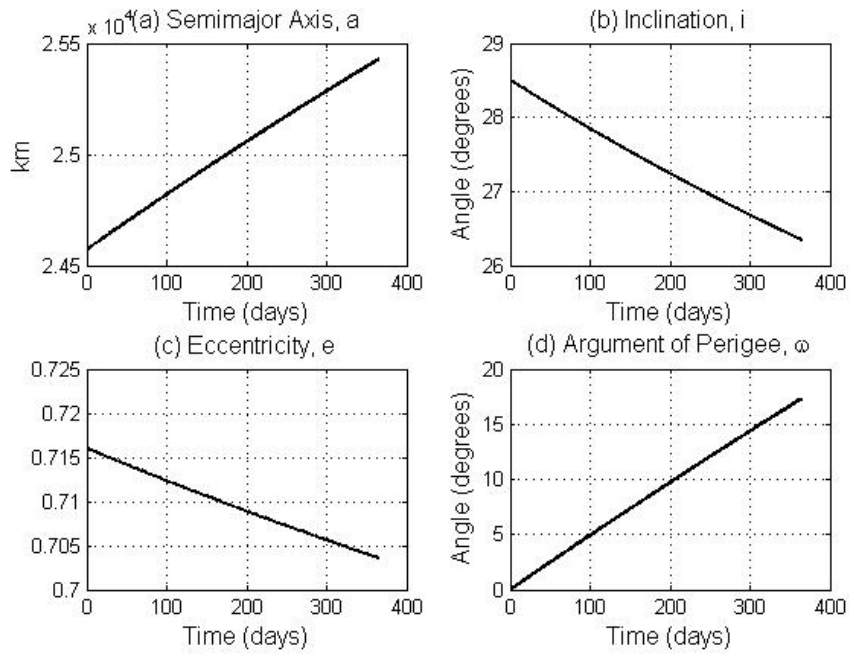


Figure 4.7: Orbital elements for the GTO plane-change maneuver. Plot (a) is the semimajor axis, plot (b) is the inclination, plot (c) is the orbital eccentricity, and plot (d) is the argument of perigee.

(c) shows the orbital eccentricity over the course of the maneuver. In this case, the eccentricity tends to get smaller, decreasing by 0.012 over the year. Figure 4.7, plot (d), shows the argument of perigee of the satellite. As the charge is of only one polarity, ω tends to go in only one direction (positively). The change in ω causes the orbit to rotate within the orbital plane.

The GTO inclination maneuver is not as effective as the LEO plane change. By virtue of always remaining at low altitude where the Lorentz force is strongest, the LEO plane change happens 10 times faster. The long time scale of the GTO maneuver makes it impractical to use. After one year, the LAO saves little in terms of propellant use. For the most favorable geometries, the ΔV savings afforded by the LAO maneuver over a conventional propulsive maneuver is only 159 m/s.

4.4 LAO Power Consumption and Plasma Density-based Control

The simulations in Section 4.3 do not include a model of the Earth’s ionosphere. The spacecraft design process is carried out initially using the IRI model, and then that design is used in simulation. The simulation assumes the spacecraft maintains its design charge-to-mass ratio, regardless of the local plasma conditions. In this section, we explore the use of a more in-depth LAO simulation by revisiting the LEO inclination-change maneuver. Here, we use a different code that takes into account local ionospheric conditions and their effect on the instantaneous charge-to-mass ratio and power consumption of the spacecraft.

The high-fidelity, plasmadynamics simulation is based upon the Global Core Plasma Model (GCPM)[57]. The GCPM model is a framework for blending multiple empirical plasma density models and extending the IRI model to full global coverage. For the simulations below, the GCPM model at one particular time is used. This time corresponds to mean solar conditions. Although there is a strong correlation between plasma conditions and time of day, this effect is averaged out by simulating over the course of multiple days.

This simulation functions in a different fashion from the results presented in Section 4.3. The earlier simulations assume that $\frac{q}{m}$ is either zero or constant at a value of -0.007 C/kg. The GCPM simulation assumes that the spacecraft maintains a constant potential on the capacitor. Because of local variations in plasma density a constant potential results in varying values of charge-to-mass ratio and varying power required to hold the constant potential. While the mean $\frac{q}{m}$ and orbit-average power are consistent with those predicted in our earlier analysis in the

Section 4.2, they have peak and minimum values that depend on to the local plasma environment.

The local electron number density, n_e , is a strong predictor of power usage and is readily available from the GCPM model. A higher n_e corresponds to a denser plasma, which, in turn, results in more current collection for a stocking at a given potential. Thus, high n_e values correlate to high power usage. In a gross sense, n_e is larger in the low to mid latitudes on the daytime side of the Earth. The density of the plasma also drops sharply as a function of altitude.

Assuming the spacecraft has knowledge of its local plasma conditions, significant power savings can be realized by limiting the charge-on time when n_e is high. The spacecraft simply follows its normal control law but turns off the charge whenever n_e exceeds a particular value. A sample of this power savings and cost in time is shown in Table 4.6. This table lists the results of four simulations performed with the constant-potential code. Each simulation integrates over three days and begins with the same initial conditions. Reported for each run is the mean $\frac{q}{m}$ achieved (during times of nonzero charging), the average power used (over the entire simulation), the peak instantaneous power used, the total inclination change over the simulation, and an efficiency in the form of degrees of inclination change per day divided by the average power used. The first simulation uses the e -limiting quadrant controller discussed above with no modification based on electron density. The other three runs superimpose an n_e -based, density-limited control, turning off the charge when n_e is greater some value.

The average $\frac{q}{m}$ achieved by each successive simulation is slightly lower, as seen in the first row of Table 4.6. In regions of high plasma density, the capacitance of the stocking is increased by a tighter plasma sheath, leading to a larger capacitance.

Table 4.6: Limiting Power Usage Via n_e (in m^{-3}) Sensing for 3 Day Simulations at an Initial Inclination of $i = 28.5^\circ$ at an Altitude of 600 km

	No n_e Control	$n_e < 2e11$	$n_e < 1.5e11$	$n_e < 1.1e11$
$\frac{q}{m_{mean}}$ (C/kg)	-0.0060	-0.0057	-0.0054	-0.0048
P_{mean} (kW)	53.54	35.88	24.33	12.94
P_{peak} (kW)	418.57	220.01	140.64	89.59
Δi ($^\circ$)	0.3764	0.3292	0.2653	0.1747
$^\circ/\text{day}/\text{kW}_{mean}$	0.0023	0.0031	0.0036	0.0045

However, this increase $\frac{q}{m}$ requires significantly more power to maintain, as the denser plasma greatly increases the current collected by the stocking. The power reduction due to density-limited control is shown in the second and third rows of Table 4.6. Without density-based control, the average power usage over the simulation is 53.54 kW, but with a peak instantaneous power usage of 418.57 kW. When charge is only applied for an n_e of less than $1.1e11m^{-3}$ (the mean electron density in this orbit), the power usage drops to a mean of 12.94 kW, with a peak of 89.59 kW. Of course, the decreased power usage is coupled with a lengthening of the maneuver time. Row 4 of Table 4.6 shows the inclination change achieved over three days for each level of density control. The unlimited control changes inclination at a rate about 2.2 times higher than the $n_e < 1.1e11$ case. However, the density-limited controllers achieve inclination changes in a more efficient way. The fifth row of Table 4.6 displays an efficiency metric for each simulation, namely degrees of inclination change achieved per day per average kilowatt used. Charging only at low values of n_e more efficiently uses the available power to effect inclination change.

The profile of electron densities experienced by a spacecraft varies greatly de-

pending on its orbit. In the 28.5° inclination change example, both the change in inclination and the change in altitude during the maneuver cause no one limit on n_e to be appropriate. However, recreating this entire maneuver using the GCPM, constant voltage simulation is impractical in its computational demands. A reasonable approximation is a hybrid simulation in which a constant charge-to-mass ratio is used, but the electron density is calculated at each step in the integration in order to superimpose the density-limited control strategy. To take advantage of the orbit raising that occurs during the maneuver, the n_e cutoff value is made a linear function of the spacecraft altitude. This line is defined by two points: n_e equal to $2.0e11m^{-3}$ at an altitude of 600 km, and n_e equal to $1.6e11m^{-3}$ at an altitude of 700 km. These values are chosen to give a reasonable trade-off between power savings and maneuver time.

Figure 4.8 shows the results of this hybrid simulation. The top plot of this figure shows semimajor axis, while the lower plot gives the inclination, both versus time in days. The solid black lines are the results of the hybrid constant $\frac{q}{m}$, density-limited simulation. For comparison, the dashed grey lines show the results of the constant-charge-only simulation. The hybrid strategy completes the inclination-change maneuver in 380 days compared to 340 days for the original strategy.

To provide insight into the power saved by using the density-limited hybrid strategy, short-duration simulations are run using the full GCPM, constant voltage code. These simulations are run for three points in the trajectory of both the hybrid simulation and the original inclination-change maneuver. When each trajectory reaches 28.5° , 10° , and 1° of orbital inclination, its state is retrieved and used as the initial conditions for a three-day simulation using the full GCPM code. The results of these simulations are summarized in Table 4.7. This table gives the

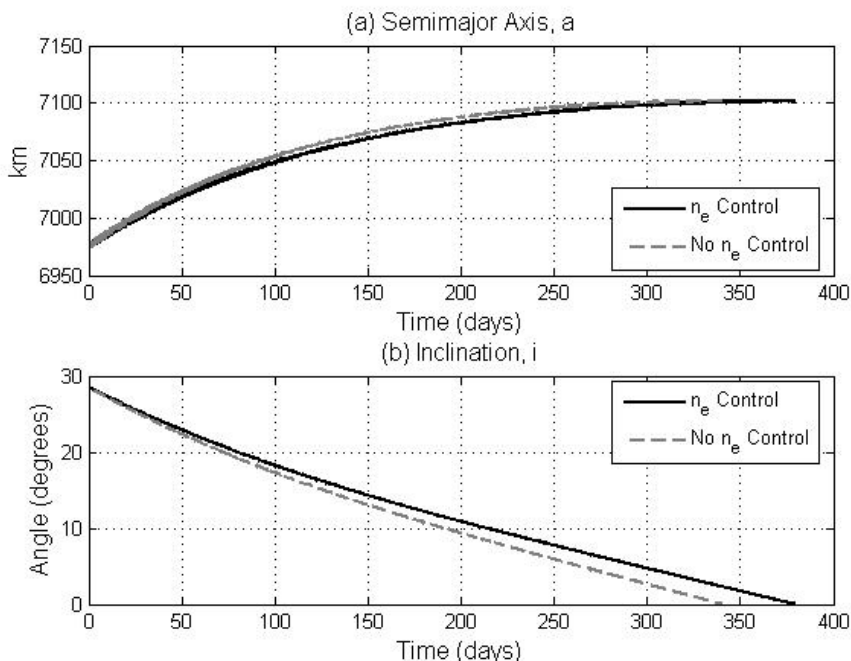


Figure 4.8: Comparison of hybrid simulation of constant charge-to-mass ratio with plasma density-limited control to constant $\frac{q}{m}$ only control.

mean achieved charge-to-mass ratio, average and peak power consumptions, and inclination change over the three-day simulation for each control strategy for each inclination considered. The addition of density-limited control reduces both the mean and peak power usage but also decreases the speed of the inclination change.

4.5 Chapter Conclusions

While the direction of the Lorentz force is fixed by the velocity of the spacecraft and the local field, varying the magnitude of the charge-to-mass ratio of the satellite can produce novel and useful changes to an orbit. A simple on-off (or bang-off) charging scheme is sufficient to perform most available maneuvers and can create large savings of ΔV .

Table 4.7: Comparison of Power Usage During Both the Hybrid Simulation and the Original, Constant Charge Simulation.

Inclination		Constant Charge	Hybrid, Density-limited
28.5°	$\frac{q}{m_{mean}}$ (C/kg)	-0.0060	-0.0057
	$P_{mean}(P_{peak})$ (kW)	53.54 (418.57)	36.50 (217.15)
	Δi (°)	0.3764	0.3308
10°	$\frac{q}{m_{mean}}$ (C/kg)	-0.0055	-0.0053
	$P_{mean}(P_{peak})$ (kW)	56.79 (259.47)	43.64 (208.58)
	Δi (°)	0.1806	0.1622
1°	$\frac{q}{m_{mean}}$ (C/kg)	-0.0055	-0.0053
	$P_{mean}(P_{peak})$ (kW)	58.39 (235.89)	43.54 (208.39)
	Δi (°)	0.1447	0.1330

A preliminary evaluation of some possible architectures leads us to the tentative conclusion that up to 0.0070 C/kg can be reached by a negatively charged LEO spacecraft of 600 kg mass. These designs use cylindrical mesh “stocking” capacitive structures that are shorter than most proposed electrodynamic tethers and offer the important benefit that their performance is independent of their attitude in the magnetic field. That simplicity largely decouples attitude control from propulsion, a consideration that can complicate the operation of tether-driven spacecraft.

The Earth’s magnetic field is a complex structure. Accurate analytical expressions for orbital perturbations are difficult to obtain. The proposed control method accommodates this complexity by breaking the geomagnetic field into distinct zones based on its sign in three orthogonal directions, leading to eight zones. Within each zone an LAO tends to evolve in certain directions for certain orbital elements. Understanding how the orbital evolution relates to the zone the space-

craft is in allows us to develop control strategies to execute complex maneuvers. A simple, but effective strategy is to operate a bang-off control scheme that switches only at zone boundaries. This scheme allows for the execution of a sample maneuver of a LEO plane change without the use of propellant, saving a ΔV of 3.75 km/s required for a conventional propulsive maneuver. However, this maneuver lasts for 340 days and requires about 53 kW of power on average. A controller that limits charging in response to local plasma-density measurements reduces this power requirement to an average of 40 kW but increases the maneuver time to 380 days.

CHAPTER 5

FORMATION FLIGHT USING THE LORENTZ FORCE

Spacecraft formation flight is an enabling technology for many spacecraft missions. Traditional formations require formation keeping and maintenance throughout their lifetime. Using traditional propulsion systems for these maneuvers limits the useful lifetime of a spacecraft formation. Using the Lorentz force allows for propellantless maintenance in addition to allowing novel formation geometries. In this chapter, we discuss the relative orbit dynamics in a simple case of LAO formation flight. A novel formation is examined for controllability and then a sample formation maneuver is presented.

5.1 Relative Dynamics and Controllability Analysis

As discussed in Chapter 1, LAO-based propulsion is not the only method charged of spacecraft formation keeping. The Coulomb Spacecraft Formation (CSF) uses the Coulomb interaction between two charged spacecraft as a method of actuation.[39]. Due to plasma shielding, CSF does not perform well in LEO because the Coulomb force from a charged spacecraft is only felt over a short distance. CSF requires a sparse plasma to work, but does not require a magnetic field, and thus is better suited for use at GEO. Conversely, LAOs exist regardless of plasma density, but its effectiveness depends on the strength of the magnetic field. LAO formations are better suited for use in LEO. Table 5.1 summarizes these ideas.

We look at the relative orbit dynamics of two spacecraft. In this simplified case, the spacecraft are both nominally orbiting in the Earth's equatorial plane. The geomagnetic field is represented by the non-tilted dipole model. The positions

Table 5.1: Relative strength of the Lorentz force and the Coulomb force between charged spacecraft.

	LEO	GEO
Plasma Density	High	Low
Ratio of circular speed to speed of magnetic field	High	Near One
Coulomb force	Near Zero	High
Lorentz force	High	Near Zero

of the two spacecraft are given by the vectors \mathbf{r}_1 and \mathbf{r}_2 , measured from the center of the Earth. These vectors are shown in Fig. 5.1.

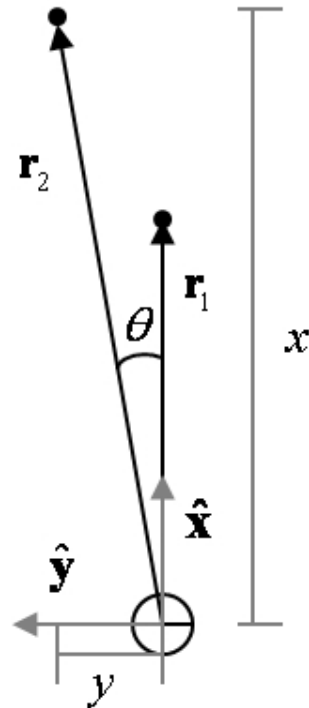


Figure 5.1: Reference Coordinates

We wish to develop the relative orbit dynamics of the two spacecraft in the

formation. For the purposes of this analysis, we assume that \mathbf{r}_1 gives the location of a reference satellite that is solely under the influence of two-body gravity. The second spacecraft, represented by \mathbf{r}_2 , will be allowed to be charged, so it will act under the influence of both gravity and the Lorentz force. The relative dynamics including the Lorentz force are conveniently described in a Hill-like frame[53]. This frame rotates with the orbit of the reference satellite. The position of spacecraft 2 in this frame is defined by a Cartesian coordinate system. The x -direction in these coordinates is measured along the \mathbf{r}_1 vector, as shown in Fig. 5.1. The y coordinate is orthogonal to this direction in the equatorial, again as is shown in Fig. 5.1. The z -direction points out of the plane, forming an appropriate right-handed coordinate system.

Recalling our earlier expression for the Lorentz force

$$\mathbf{F}_L = q\mathbf{v}_r \times \mathbf{B} \tag{1.2}$$

where \mathbf{v}_r represents the velocity of the spacecraft with respect to the magnetic field. Previously, we needed to correct for the fact that the magnetic field rotates with the Earth. In our new coordinates, we must also account for the fact that our reference frame is rotating with spacecraft 1 in its orbit. Adding this rotation to our expression for \mathbf{v}_r yields

$$\mathbf{F}_L = (\mathbf{v} + n\hat{\mathbf{n}} \times \mathbf{r}_2 - \omega_E\hat{\mathbf{n}} \times \mathbf{r}_2) \times \mathbf{B} \tag{5.1}$$

where n is the mean motion of the reference orbit and $\hat{\mathbf{n}}$ is a unit vector aligned with the Earth's spin axis. As the reference orbit is equatorial, both the Earth's spin and the coordinate frame rotation are in the same direction.

Expressing various vectors in the rotating frame yields:

$$\mathbf{r}_2 = \begin{bmatrix} x \\ y \\ z \end{bmatrix}; n\hat{\mathbf{n}} = \begin{bmatrix} 0 \\ 0 \\ n \end{bmatrix}; \omega_E\hat{\mathbf{n}} = \begin{bmatrix} 0 \\ 0 \\ \omega_E \end{bmatrix} \quad (5.2)$$

Here a model must be introduced for the Earth's magnetic field. A non-titled dipole model, valid for small excursions away from the equator, is:

$$\mathbf{B}_{\text{ref}} = \frac{B_{\text{ref}}}{r^2} \begin{bmatrix} zx \\ zy \\ z^2 \end{bmatrix} + B_{\text{ref}} \begin{bmatrix} 0 \\ 0 \\ 1 \end{bmatrix} \quad (5.3)$$

where B_{ref} is the magnitude of the magnetic field evaluated at the radius of the reference orbit, given by:

$$B_{\text{ref}} = \frac{\mu_0 m}{4\pi r_1^3} \quad (5.4)$$

where μ_0 is the permeability of free space, and m is the Earth's magnetic moment.

Using the definitions in Eqs. 5.2 and 5.3 with Eq. 5.1 give an expression for the Lorentz force in the rotating frame:

$$\mathbf{F}_{\mathbf{L}} = \frac{q}{m} B_{\text{ref}} \left(\begin{bmatrix} \dot{y} \\ -\dot{x} \\ 0 \end{bmatrix} + (n - \omega_E) \begin{bmatrix} x \\ y \\ 0 \end{bmatrix} + \frac{1}{r^2} \begin{bmatrix} \dot{y}z^2 - \dot{z}zy \\ \dot{z}zx - \dot{x}z^2 \\ \dot{x}zy - \dot{y}zx \end{bmatrix} + \frac{n - \omega_E}{r^2} \begin{bmatrix} xz^2 \\ yz^2 \\ -zy^2 - zx^2 \end{bmatrix} \right) \quad (5.5)$$

The dynamics of the rotating frame give:

$$\begin{bmatrix} \ddot{x} \\ \ddot{y} \\ \ddot{z} \end{bmatrix} + 2n \begin{bmatrix} -\dot{y} \\ \dot{x} \\ 0 \end{bmatrix} = n^2 \begin{bmatrix} -x \\ -y \\ 0 \end{bmatrix} + \mathbf{F}_{\text{grav}} + \mathbf{F}_{\mathbf{L}} \quad (5.6)$$

With two-body gravity taking the form:

$$\mathbf{F}_{\text{grav}} = -\frac{\mu}{r^3} \begin{bmatrix} x \\ y \\ z \end{bmatrix} \quad (5.7)$$

Combining Eqs. 5.5, 5.6, and 5.7, creates the following three equations of motion for spacecraft 2:

$$\begin{aligned} \ddot{x} = & \left(\frac{q}{m} B_{ref}(n - \omega_E) + n^2 - \frac{\mu}{(x^2 + y^2 + z^2)^{3/2}} \right) x \\ & + \left(\frac{q}{m} B_{ref} + 2n \right) \dot{y} + \frac{q}{m} \frac{B_{ref}}{x^2 + y^2 + z^2} [\dot{y}z^2 - \dot{z}zy + (n - \omega_E)xz^2] \end{aligned} \quad (5.8)$$

$$\begin{aligned} \ddot{y} = & \left(\frac{q}{m} B_{ref}(n - \omega_E) + n^2 - \frac{\mu}{(x^2 + y^2 + z^2)^{3/2}} \right) y \\ & - \left(\frac{q}{m} B_{ref} + 2n \right) \dot{x} + \frac{q}{m} \frac{B_{ref}}{x^2 + y^2 + z^2} [-\dot{x}z^2 + \dot{z}zx + (n - \omega_E)yz^2] \end{aligned} \quad (5.9)$$

$$\begin{aligned} \ddot{z} = & -\frac{\mu}{(x^2 + y^2 + z^2)^{3/2}} z + \frac{q}{m} \frac{B_{ref}}{x^2 + y^2 + z^2} [\dot{x}yz - \dot{y}xz \\ & - (n - \omega_E)x^2z - (n - \omega_E)y^2z] \end{aligned} \quad (5.10)$$

In this simple circular, equatorial problem, the Lorentz force on spacecraft will generally be in the radial direction. Effectively this force is a central force either augmenting or decrementing gravity. By changing the magnitude of the central force acting on the spacecraft, we change the angular velocity at which it orbits. Using the Lorentz force, we can create a “levitating” formation, in which spacecraft 2 can be at a different orbital radius than spacecraft 1 (in the same plane), but have same orbital angular velocity. In the rotating frame satellite 2 appears stationary, “levitating” over spacecraft one. In this equilibrium state, the following expressions hold true:

$$y = z = \dot{x} = \dot{y} = \dot{z} = 0; x = x_0 \quad (5.11)$$

Using these conditions in the equations of motion, an equilibrium charge can be

defined:

$$\left(\frac{q}{m}\right)_0 = \frac{\mu - n^2 x_0^3}{x_0^3 B_{ref}(n - \omega_E)} \quad (5.12)$$

This nominal charge $\left(\frac{q}{m}\right)_0$ allows spacecraft to be stationary in the rotating frame. By levitating multiple spacecraft, a formation of arbitrary shape can be formed in the equatorial plane.

We wish to linearize this system about the levitating equilibrium in order to examine its stability and controllability. Using these definitions:

$$x = x_0 + \delta x; y = 0 + \delta y; z = 0 + \delta z; \frac{q}{m} = \frac{q_0}{m} + \frac{\delta q}{m} \quad (5.13)$$

the linear equations of motion become:

$$\begin{aligned} \ddot{\delta x} = & \left[\left(\frac{q}{m}\right)_0 B_{ref}(n - \omega_E) + n^2 + \frac{2\mu}{x_0^3} \right] \delta x + \left(\left(\frac{q}{m}\right)_0 B_{ref} + 2n \right) \dot{\delta y} \\ & + [B_{ref}(n - \omega_E)x_0] \frac{\delta q}{m} \end{aligned} \quad (5.14)$$

$$\ddot{\delta y} = - \left(\left(\frac{q}{m}\right)_0 B_{ref} + 2n \right) \dot{\delta x} + \left[\left(\frac{q}{m}\right)_0 B_{ref}(n - \omega_E) + n^2 - \frac{\mu}{x_0^3} \right] \delta y \quad (5.15)$$

$$\ddot{\delta z} = - \left[\frac{\mu}{x_0^3} - \left(\frac{q}{m}\right)_0 B_{ref}(n - \omega_E) \right] \delta z \quad (5.16)$$

Note that the linear dynamics in the z -direction is uncoupled from the other motions and represent a simple harmonic oscillator. The system can be reworked into a state space model of the following form:

$$\begin{bmatrix} \dot{\delta x} \\ \dot{\delta y} \\ \dot{\delta z} \\ \ddot{\delta x} \\ \ddot{\delta y} \\ \ddot{\delta z} \end{bmatrix} = A \begin{bmatrix} \delta x \\ \delta y \\ \delta z \\ \dot{\delta x} \\ \dot{\delta y} \\ \dot{\delta z} \end{bmatrix} + B \frac{\delta q}{m} \quad (5.17)$$

where:

$$A = \begin{bmatrix} 0 & 0 & 0 & 1 & 0 & 0 \\ 0 & 0 & 0 & 0 & 1 & 0 \\ 0 & 0 & 0 & 0 & 0 & 1 \\ \frac{3\mu}{x_0^3} & 0 & 0 & 0 & [\alpha + 2n] & 0 \\ 0 & 0 & 0 & -[\alpha + 2n] & 0 & 0 \\ 0 & 0 & \left[\alpha\Delta - \frac{\mu}{x_0^3}\right] & 0 & 0 & 0 \end{bmatrix} \quad (5.18)$$

$$B = \begin{bmatrix} 0 \\ 0 \\ 0 \\ B_{ref}\Delta x_0 \\ 0 \\ 0 \end{bmatrix} \quad (5.19)$$

using these definitions:

$$\alpha = \frac{q_0}{m} B_{ref}; \Delta = n - \omega_E \quad (5.20)$$

As noted before, the z motion is uncoupled from the in-plane motion, oscillatory, and is also uncontrollable.

Examining only the in-plane system (x and y coordinates and their derivatives), the stability of the levitating equilibrium is studied. The reduced 4x4 A matrix has two stable eigenvalues in the left half plane and two zero eigenvalues. Thus the linear system is marginally stable. The controllability matrix for the reduced system is given by

$$\mathcal{C} = \begin{bmatrix} A & AB & AAB & AAAB \end{bmatrix} \quad (5.21)$$

and has rank 3. Thus, the system has three controllable states and one uncontrollable state. Examining the null space of \mathcal{C} shows that the uncontrollable direction corresponds to $\dot{\delta}y$. Thus, velocity in the along track direction cannot be controlled

in this system. However, as will be seen in the next section, intelligent maneuver planning using the natural relative orbit dynamics will allow useful maneuvers to occur without this controllability.

5.2 Simple LAO Formation Maneuver

A simple formation maneuver is performed entirely using the Lorentz force. The formation is a three-satellite, planar triangle. This triangle is in the Earth’s equatorial plane. One spacecraft, Satellite A, in the formation is used as a reference satellite. This satellite is in a Keplerian circular, equatorial, orbit. The two remaining spacecraft begin the maneuver in “levitating” equilibria. One LAO satellite, Satellite B, is leading the reference and one, Satellite C, is trailing, forming a triangular formation.

The goal of the maneuver is to have the leading and trailing LAO satellites switch roles. They must exit their LAO hovering and perform a phasing correction, using only the Lorentz force. The reconfiguration is accomplished by calculating an open loop trajectory that achieves this goal, and using a closed loop PD controller to follow this trajectory. The open loop reference is required because of the controllability issue discussed in the previous section. The trajectory is formed by inputting the size of the desired phasing action, dr , and calculating the time, t_{man} , to perform such a maneuver with respect to a known reference maneuver. These quantities are related by the simple linear expression

$$t_{man} = \frac{dr}{dr_{ref}} t_{ref} \quad (5.22)$$

where dr_{ref} and t_{ref} are the reference maneuver size and duration, respectively. The inputs to the controller are the satellite’s desired angular velocity, radial posi-

tion, and radial velocity. These inputs come from the previously calculated trajectory. This trajectory planning is necessary because of the uncontrollability issues discussed above. The controller outputs a charge-to-mass ratio commanded to the spacecraft. Thus, the controller is of the form

$$\frac{q}{m} = \mathbf{K} \begin{bmatrix} \omega_{des} - \omega \\ r_{des} - r \\ \dot{r}_{des} - \dot{r} \end{bmatrix} \quad (5.23)$$

where \mathbf{K} is a 1x3 gain matrix. The PD controller is also used to maintain the hovering state of the satellite when desired.

The simulation used to demonstrate this maneuver is a full three-dimensional system, integrating full dynamics for all three satellites. The orbit of the reference satellite is a 400 km altitude, circular, equatorial orbit. The tilted dipole magnetic field model is used. In Section 5.1, the non-tilted dipole model was used to derive the levitating behavior. Here, the PD controller is able to maintain the levitating equilibrium in the presence of this unmodeled portion of the magnetic field. In this simulation the value of \mathbf{K} is given by $[-14e4, 0.3, -5]$. The reference maneuver is a manually tuned 50m phasing maneuver that takes one orbit to complete. The desired maneuver is 25m phasing change that allows the two moving satellites to switch positions in the triangular formation.

The maneuver lasts for 2.5 orbits of the reference satellite. During the first orbit the triangle formation is maintained by the controller in order to show that it is stable throughout an orbit. During the following half orbit of Satellite A, the maneuver is performed by Satellites B and C. The final full orbit shows that the new configuration is stable as well, again with the controller active.

The resulting path of the satellites is shown in Fig. 5.2. This figure shows

the track of each spacecraft relative to Satellite A. Circular points represent initial positions, with triangular points denoting final positions. Figure 1 shows that the maneuver is a success. Figure 5.3 shows the charge-to-mass ratio, $\frac{q}{m}$, commanded by the controller to each LAO satellite. The charge-to-mass ratio was capped at 0.005 C/kg. This limit could be removed if the gains were tuned to prevent actuator saturation. The maneuver is completed successfully.

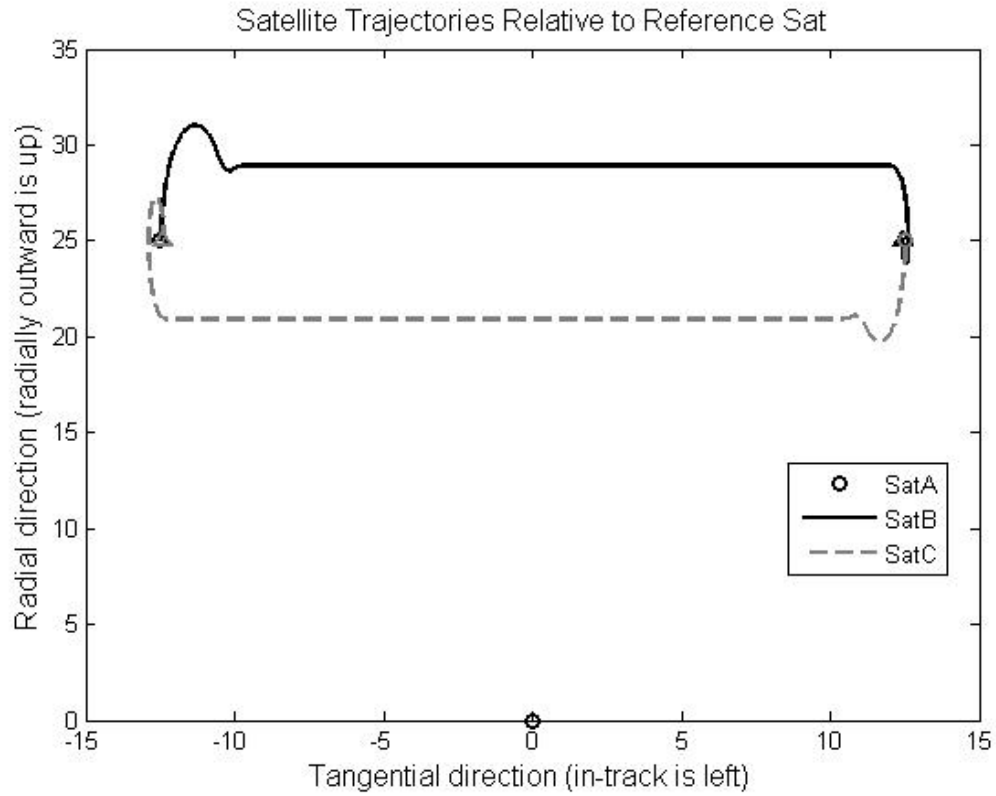


Figure 5.2: Track of the formation satellites with reference frame centered on Satellite A. Circular points represent starting positions, with triangular points denoting finishing positions.

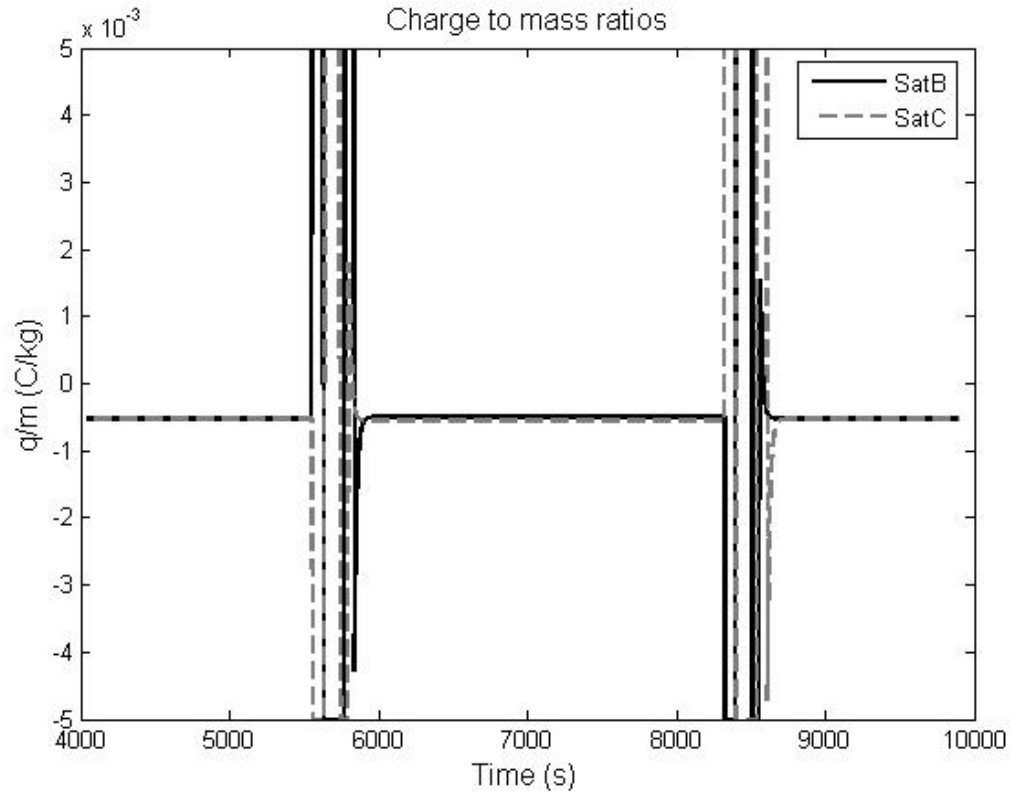


Figure 5.3: Charge-to-mass ratio in C/kg for each LAO satellite in the formation. The maximum q/m ratio for each satellite was capped at a magnitude of 0.005 C/kg.

5.3 Chapter Conclusions

The Lorentz force can be used as a spacecraft formation actuator. In the equatorial plane, "levitating" formations of arbitrary shape can be created within the plane. Under linearized dynamics, these formations are marginally stable, and three out of four states are controllable by simply varying the magnitude of the charge on a spacecraft. By exploiting the natural relative orbit dynamics in addition to the Lorentz force, useful maneuvers can be performed with LAO formations.

CHAPTER 6

CONCLUSION

The Lorentz Augmented Orbit (LAO) has been examined in depth, including its dynamics, novel mission concepts it enables, and a possible implementation of an LAO-capable spacecraft. This chapter summarizes and concludes that work, with suggestions for possible avenues of future research.

6.1 Summary and Conclusions

Control of the charge on a spacecraft enables engineering applications of an LAO. This type of propellantless propulsion is used to develop a number of applications and novel missions including:

- With high charge-to-mass ratios, new Earth-synchronous orbits can be created. One such orbit is the LAO GT-1, a single-pass repeat-groundtrack orbit. This orbit always passes over the same set of points on the ground. While derived for a simple magnetic field model, this behavior can be recovered for more complex field structure. In addition to Earth-synchronous orbits, new Sun-synchronous orbits can be created for a much wider class of orbits than previously possible.
- The Lorentz force can increase the flexibility and effectiveness of gravity-assist maneuvers about planets with magnetic fields. An LAO-capable spacecraft can be temporarily and reversibly captured at the target planet. In addition allowing for more flexible timing, the spacecraft can make small changes to its orbit while captured, affecting its eventual exit from the target planet, and thus the effective ΔV of the flyby.

- Under realistic magnetic field conditions and using near-term technology (achieving a $\frac{q}{m}$ of 0.007 C/kg), useful LAO maneuvers are still available. Partitioning the geomagnetic field into distinct zones and using a bang-bang controller allows for a tractable control synthesis problem. The Lorentz force is particularly well suited for LEO inclination change maneuvers. These maneuvers can save large amount of propellant at the cost of longer maneuver duration and significant electrical power.
- The small magnitude of the Lorentz force suggests that it can be useful for spacecraft formations. In equatorial orbits, sets of LAOs can be found to allow for the creation of arbitrarily shaped, planar formations. Combining the Lorentz force and natural relative orbit dynamics, useful formation maneuvers can be performed.

These applications are explored using both analytical and numerical methods with varying levels of detail and three different magnetic field models.

6.2 Recommendations for Future Work

This research can be extended in a number of ways. While same basic orbit dynamics applies in all LAOs, the space of LAO applications has not been fully explored. There is also a large amount of work that needs to be completed in order to produce a working LAO-capable spacecraft, but that direction of research will not be discussed in this section.

One fertile area for future work is the area of Lorentz-augmented formation flight. The material presented in Chapter 5 is only a first look at formations of LAOs.

That work describes only a restricted look at LAO formations in the equatorial plane under a simplified magnetic field. There are many other places to search for uses of LAOs in building and maintaining formations, including the fusion of the Coulomb spacecraft formation with Lorentz-based propulsion .

There are also a number of ways to optimize LAOs that have not been discussed here. The effectiveness of a particular LAO spacecraft design such as the one presented in Chapter 4 depends heavily on local plasma parameters. In turn, the local plasma properties depend heavily upon altitude and latitude, and to a lesser extent longitude. The classes of orbits used in an LAO application can be optimized based upon plasma models to achieve maximum charge-to-mass ratios or minimum power usage. In addition to optimizing over particular orbit classes, the central body can also be optimized. Earth, Jupiter, and Saturn are all tempting candidates. How effective an LAO spacecraft can be at any given planet depends upon its local plasma parameters and magnetic fields. A more in-depth look across the different planets may identify an application particularly well suited to LAOs.

The effect of more complicated/time-varying magnetic structures on an LAO should be examined. The Earth has time-varying components of its field in addition to large structures such as the magnetic tail formed by interaction with the solar wind. These features are not included in a spherical harmonic representation of the geomagnetic field and could produce significant effects, especially outside of LEO. The magnetic field of Jupiter is also more complex than a spherical harmonic model, including interactions with the sun and ionized volcanic plumes from its moon Io. Additionally, the sun has its own complex magnetic field that dominates interplanetary space, and has not been examined for LAO prospects in this work.

An additional novel LAO that has not been developed is called the Joviastat. In

this configuration, the relatively strong magnetic field and fast rotation of Jupiter can actually balance the gravitational force on a spacecraft, allowing it to have zero inertial motion for a reasonably small charge-to-mass ratio. The spacecraft then “hovers” as Jupiter rotates under it. The applications or feasibility of such a system have not been thoroughly examined.

One final possible future research topic is the development and analysis of a combined LAO/electrodynamic tether system. The LAO architecture presented in Chapter 4 shares many similarities with tether spacecraft architectures. The forces produced by a body charge and a tether current tend to be complimentary, allowing for a more general force to be produced by the still-propellantless combined system. Together the two technologies may be able to produce compelling applications that take advantage of the each ones strengths, while skirting their individual weaknesses.

APPENDIX A

MAGNETIC POTENTIAL AND FIELD EXPANSIONS

The magnetic vector potential field \mathbf{A} and magnetic field \mathbf{B} expanded by spherical harmonic term up to 2nd degree, 2nd order. The fields are shown with respect to the Earth-centered, Earth-fixed spherical harmonic unit vectors. A discussion of this model appears in Section 1.2. The 1,0 term represents the non-tilted dipole field component. The combination of the 1,0 and 1,1 terms gives the tilted dipole model.

1,0:

$$\begin{aligned}
 \mathbf{A}_{1,0} \cdot \hat{\mathbf{r}} &= 0 \\
 \mathbf{A}_{1,0} \cdot \hat{\phi} &= 0 \\
 \mathbf{A}_{1,0} \cdot \hat{\theta} &= R_E g_{1,0} \left(\frac{R_E}{r} \right)^2 \sin \phi
 \end{aligned} \tag{A.1}$$

$$\begin{aligned}
 \mathbf{B}_{1,0} \cdot \hat{\mathbf{r}} &= 2g_{1,0} \left(\frac{R_E}{r} \right)^3 \cos \phi \\
 \mathbf{B}_{1,0} \cdot \hat{\phi} &= g_{1,0} \left(\frac{R_E}{r} \right)^3 \sin \phi \\
 \mathbf{B}_{1,0} \cdot \hat{\theta} &= 0
 \end{aligned} \tag{A.2}$$

1,1:

$$\begin{aligned}
 \mathbf{A}_{1,1} \cdot \hat{\mathbf{r}} &= 0 \\
 \mathbf{A}_{1,1} \cdot \hat{\phi} &= -R_E \left(\frac{R_E}{r} \right)^2 (-g_{1,1} \sin \theta + h_{1,1} \cos \theta) \\
 \mathbf{A}_{1,1} \cdot \hat{\theta} &= R_E \left(\frac{R_E}{r} \right)^2 (-g_{1,1} \cos \theta + h_{1,1} \sin \theta) \cos \phi
 \end{aligned} \tag{A.3}$$

$$\begin{aligned}
\mathbf{B}_{1,1} \cdot \hat{\mathbf{r}} &= -2 \left(\frac{R_E}{r} \right)^3 (g_{1,1} \cos \theta + h_{1,1} \sin \theta) \sin \phi \\
\mathbf{B}_{1,1} \cdot \hat{\phi} &= \left(\frac{R_E}{r} \right)^3 (g_{1,1} \cos \theta + h_{1,1} \sin \theta) \cos \phi \\
\mathbf{B}_{1,1} \cdot \hat{\theta} &= \left(\frac{R_E}{r} \right)^3 (-g_{1,1} \sin \theta + h_{1,1} \cos \theta)
\end{aligned} \tag{A.4}$$

2,0:

$$\begin{aligned}
\mathbf{A}_{2,0} \cdot \hat{\mathbf{r}} &= 0 \\
\mathbf{A}_{2,0} \cdot \hat{\phi} &= 0 \\
\mathbf{A}_{2,0} \cdot \hat{\theta} &= \frac{3}{4} g_{2,0} R_E \left(\frac{R_E}{r} \right)^3 \sin 2\phi
\end{aligned} \tag{A.5}$$

$$\begin{aligned}
\mathbf{B}_{2,0} \cdot \hat{\mathbf{r}} &= \frac{3}{4} g_{2,0} \left(\frac{R_E}{r} \right)^4 (3 \cos 2\phi + 1) \\
\mathbf{B}_{2,0} \cdot \hat{\phi} &= \frac{3}{2} g_{2,0} \left(\frac{R_E}{r} \right)^4 \sin 2\phi \\
\mathbf{B}_{2,0} \cdot \hat{\theta} &= 0
\end{aligned} \tag{A.6}$$

2,1:

$$\begin{aligned}
\mathbf{A}_{2,1} \cdot \hat{\mathbf{r}} &= 0 \\
\mathbf{A}_{2,1} \cdot \hat{\phi} &= -\frac{3}{2} R_E \left(\frac{R_E}{r} \right)^3 (-g_{2,1} \sin \theta + h_{2,1} \cos \theta) \cos \phi \\
\mathbf{A}_{2,1} \cdot \hat{\theta} &= \frac{3}{2} R_E \left(\frac{R_E}{r} \right)^3 (g_{2,1} \cos \theta + h_{2,1} \sin \theta) (2 \cos^2 \phi - 1)
\end{aligned} \tag{A.7}$$

$$\begin{aligned}
\mathbf{B}_{2,1} \cdot \hat{\mathbf{r}} &= -\frac{9}{2} \left(\frac{R_E}{r} \right)^4 (g_{2,1} \cos \theta + h_{2,1} \sin \theta) \sin 2\phi \\
\mathbf{B}_{2,1} \cdot \hat{\phi} &= 3 \left(\frac{R_E}{r} \right)^4 (g_{2,1} \cos \theta + h_{2,1} \sin \theta) \cos 2\phi \\
\mathbf{B}_{2,1} \cdot \hat{\theta} &= 3 \left(\frac{R_E}{r} \right)^4 (-g_{2,1} \sin \theta + h_{2,1} \cos \theta) \cos \phi
\end{aligned} \tag{A.8}$$

2,2:

$$\begin{aligned}\mathbf{A}_{2,2} \cdot \hat{\mathbf{r}} &= 0 \\ \mathbf{A}_{2,2} \cdot \hat{\phi} &= 3R_E \left(\frac{R_E}{r} \right)^3 (-g_{2,2} \sin 2\theta + h_{2,2} \cos 2\theta) \sin \phi \\ \mathbf{A}_{2,2} \cdot \hat{\theta} &= -3R_E \left(\frac{R_E}{r} \right)^3 (g_{2,2} \cos 2\theta + h_{2,2} \sin 2\theta) \sin \phi \cos \phi\end{aligned}\tag{A.9}$$

$$\begin{aligned}\mathbf{B}_{2,2} \cdot \hat{\mathbf{r}} &= 9 \left(\frac{R_E}{r} \right)^4 (g_{2,2} \cos 2\theta + h_{2,2} \sin 2\theta) \sin^2 \phi \\ \mathbf{B}_{2,2} \cdot \hat{\phi} &= -6 \left(\frac{R_E}{r} \right)^4 (g_{2,2} \cos 2\theta + h_{2,2} \sin 2\theta) \sin \phi \cos \phi \\ \mathbf{B}_{2,2} \cdot \hat{\theta} &= -6 \left(\frac{R_E}{r} \right)^4 (-g_{2,2} \sin 2\theta + h_{2,2} \cos 2\theta) \sin \phi\end{aligned}\tag{A.10}$$

APPENDIX B

CANONICAL VARIABLES AND HAMILTONIANS

Canonical coordinates and conjugate momenta with corresponding Hamiltonian for individual spherical harmonic components. Each canonical set below assumes that only a single magnetic harmonic is present to isolate the effect of that particular harmonic on the dynamics. The 0,0 case represents Keplerian orbital motion in the Earth-centered, Earth-fixed frame with no magnetic field component present. These expressions make use of the material in Schaffer and Burns[22] and are discussed in more detail in Section 1.3.

0,0:

$$\begin{aligned}
 r \quad p_{r_{0,0}} &= m\dot{r} \\
 \phi \quad p_{\phi_{0,0}} &= mr^2\dot{\phi} \\
 \theta \quad p_{\theta_{0,0}} &= mr^2 \sin^2 \phi (\dot{\theta} + \omega_E)
 \end{aligned} \tag{B.1}$$

$$\begin{aligned}
 H_{0,0} &= \frac{1}{2m}p_r^2 + \frac{1}{2mr^2}p_\phi^2 + \frac{1}{2mr^2 \sin^2 \phi} (p_\theta - mr^2 \omega_E \sin^2 \phi)^2 \\
 &\quad + m\Phi_g - \frac{1}{2}mr^2 \omega_E^2 \sin^2 \phi
 \end{aligned} \tag{B.2}$$

1,0:

$$\begin{aligned}
 r \quad p_{r_{1,0}} &= m\dot{r} \\
 \phi \quad p_{\phi_{1,0}} &= mr^2\dot{\phi} \\
 \theta \quad p_{\theta_{1,0}} &= mr^2 \sin^2 \phi (\dot{\theta} + \omega_E) + qg_{1,0}R_E^3 \frac{1}{r} \sin^2 \phi
 \end{aligned} \tag{B.3}$$

$$\begin{aligned}
 H_{1,0} &= \frac{1}{2m}p_r^2 + \frac{1}{2mr^2}p_\phi^2 + \frac{1}{2mr^2 \sin^2 \phi} (p_\theta - mr^2 \omega_E \sin^2 \phi - qg_{1,0}R_E^3 \frac{1}{r} \sin^2 \phi)^2 \\
 &\quad + m\Phi_g - \frac{1}{2}mr^2 \omega_E^2 \sin^2 \phi
 \end{aligned} \tag{B.4}$$

1,1:

$$\begin{aligned}
r \quad p_{r_{1,1}} &= m\dot{r} \\
\phi \quad p_{\phi_{1,1}} &= mr^2\dot{\phi} - qR_E^3\frac{1}{r}(-g_{1,1}\sin\theta + h_{1,1}\cos\theta) \\
\theta \quad p_{\theta_{1,1}} &= mr^2\sin^2\phi(\dot{\theta} + \omega_E) + qR_E^3\frac{1}{r}(g_{1,1}\cos\theta\cos\phi + h_{1,1}\sin\theta\sin\phi)\sin\phi
\end{aligned} \tag{B.5}$$

$$\begin{aligned}
H_{1,1} &= \frac{1}{2m}p_r^2 + \frac{1}{2mr^2}(p_\phi + qR_E^3\frac{1}{r}[-g_{1,1}\sin\theta + h_{1,1}\cos\theta])^2 \\
&\quad + \frac{1}{2mr^2\sin^2\phi}(p_\theta - mr^2\omega_E\sin^2\phi - qR_E^3\frac{1}{r}(g_{1,1}\cos\theta\cos\phi + h_{1,1}\sin\theta\sin\phi)\sin\phi)^2 \\
&\quad + m\Phi_g - \frac{1}{2}mr^2\omega_E^2\sin^2\phi
\end{aligned} \tag{B.6}$$

2,0:

$$\begin{aligned}
r \quad p_{r_{2,0}} &= m\dot{r} \\
\phi \quad p_{\phi_{2,0}} &= mr^2\dot{\phi} \\
\theta \quad p_{\theta_{2,0}} &= mr^2\sin^2\phi(\dot{\theta} + \omega_E) + \frac{3}{4}qg_{2,0}R_E^4\frac{1}{r^2}\sin 2\phi\sin\phi
\end{aligned} \tag{B.7}$$

$$\begin{aligned}
H_{2,0} &= \frac{1}{2m}p_r^2 + \frac{1}{2mr^2}p_\phi^2 + \frac{1}{2mr^2\sin^2\phi}(p_\theta - mr^2\omega_E\sin^2\phi - \frac{3}{4}qg_{2,0}R_E^4\frac{1}{r^2}\sin 2\phi\sin\phi)^2 \\
&\quad + m\Phi_g - \frac{1}{2}mr^2\omega_E^2\sin^2\phi
\end{aligned} \tag{B.8}$$

2,1:

$$\begin{aligned}
r \quad p_{r_{2,1}} &= m\dot{r} \\
\phi \quad p_{\phi_{2,1}} &= mr^2\dot{\phi} - \frac{3}{2}qR_E^4\frac{1}{r^2}(-g_{2,1}\sin\theta + h_{2,1}\cos\theta)\cos\phi \\
\theta \quad p_{\theta_{2,1}} &= mr^2\sin^2\phi(\dot{\theta} + \omega_E) + \frac{3}{2}qR_E^4\frac{1}{r^2}(g_{2,1}\cos\theta + h_{2,1}\sin\theta)(2\cos^2\phi - 1)
\end{aligned} \tag{B.9}$$

$$\begin{aligned}
H_{2,1} &= \frac{1}{2m} p_r^2 + \frac{1}{2mr^2} (p_\phi + \frac{3}{2} q R_E^4 \frac{1}{r^2} (-g_{2,1} \sin \theta + h_{2,1} \cos \theta) \cos \phi)^2 \\
&+ \frac{1}{2mr^2 \sin^2 \phi} (p_\theta - mr^2 \omega_E \sin^2 \phi - \frac{3}{2} q R_E^4 \frac{1}{r^2} [g_{2,1} \cos \theta + h_{2,1} \sin \theta] [2 \cos^2 \phi - 1])^2 \\
&+ m \Phi_g - \frac{1}{2} mr^2 \omega_E^2 \sin^2 \phi
\end{aligned} \tag{B.10}$$

BIBLIOGRAPHY

- [1] McInnes, C. R., *Solar Sailing: Technology, Dynamics and Mission Applications*, Springer-Praxis, Chichester, UK, 1999.
- [2] Cosmo, M. L. and Lorenzini, E. C., *Tethers in Space Handbook Third Edition*, NASA Marshall Spaceflight Center, Huntsville, AL, 1997.
- [3] Peck, M. A., “Prospects and Challenges for Lorentz-Augmented Orbits,” *Proceedings of the AIAA Guidance, Navigation, and Control Conference*, AIAA-2005-5995, San Francisco, CA, August 2005.
- [4] Rothwell, P. L., “The superposition of rotating and stationary magnetic sources: Implications for the auroral region,” *Physics of Plasmas*, Vol. 10, No. 7, 2003, pp. 2971–2977.
- [5] Barton, C. E., “International Geomagnetic Reference Field : The Seventh Generation,” *Journal of Geomagnetism and Geoelectricity*, Vol. 49, No. 2, 1997, pp. 123–148.
- [6] Roithmayr, C. M., “Contributions of Spherical Harmonics to Magnetic and Gravitational Fields,” Tech. rep., NASA, March 2004, TM-2004-213007.
- [7] Schaffer, L. and Burns, J. A., “Charged Dust in Planetary Magnetospheres: Hamiltonian Dynamics and Numerical Simulations for Highly Charged Grains,” *Journal of Geophysical Research*, Vol. 99, 1994, pp. 17211–17223.
- [8] Russell, C. T., “Planetary Magnetospheres,” *Science Progress*, Vol. 75, 1991, pp. 93–105.
- [9] Ness, N. F., “Intrinsic Magnetic Fields of the Planets: Mercury to Neptune,” *Philosophical Transactions: Physical Sciences and Engineering*, Vol. 349, No. 1690, 1994, pp. 249–260.
- [10] Burns, J. A., “Elementary derivation of the perturbation equations of celestial mechanics,” *American Journal of Physics*, Vol. 44, No. 10, 1976, pp. 944–949.
- [11] Hough, M. E., “Lorentz Force Perturbations of A Charged Ballistic Missile,” *Proceedings of the AIAA Guidance and Control Conference*, AIAA-1982-1549, San Diego, CA, August 1982.

- [12] Streetman, B. and Peck, M. A., “New Synchronous Orbits Using the Geomagnetic Lorentz Force,” *Journal of Guidance, Control, and Dynamics*, Vol. 30, No. 6, 2007, pp. 1677–1690, AIAA-0731-5090.
- [13] Atchison, J., Streetman, B., and Peck, M. A., “Prospects for Lorentz Augmentation in Jovian Captures,” *Proceedings of the AIAA Guidance, Navigation, and Control Conference*, AIAA-2006-6596, Keystone, CO, August 2006.
- [14] Streetman, B. and Peck, M. A., “Gravity-Assist Maneuvers Augmented by the Lorentz Force,” *Proceedings of the AIAA Guidance, Navigation, and Control Conference*, AIAA-2007-6846, Hilton Head, SC, August 2007.
- [15] Streetman, B. and Peck, M. A., “A General Bang-Bang Control Method for Lorentz Augmented Orbits,” *Proceedings of the AAS Spaceflight Mechanics Conference*, AAS-08-111, Galveston, TX, January 2008.
- [16] Peck, M. A., Streetman, B., Saaj, C. M., and Lappas, V., “Spacecraft Formation Flying Using Lorentz Forces,” *Journal of the British Interplanetary Society*, Vol. 60, 2007, pp. 263–267.
- [17] Axford, W. I. and Mendis, D. A., “Satellites and Magnetospheres of the Outer Planets,” *Annual Review of Earth and Planetary Sciences*, Vol. 2, 1974, pp. 419–474.
- [18] Littlejohn, R. G., “A Guiding Center Hamiltonian: A New Approach,” *Journal of Mathematical Physics*, Vol. 20, No. 12, 1979, pp. 2445–2458.
- [19] Littlejohn, R. G., “Hamiltonian Perturbation Theory in Noncanonical Coordinates,” *Journal of Mathematical Physics*, Vol. 23, No. 5, 1982, pp. 742–747.
- [20] Morfill, G. E., “Electromagnetic Effects on Planetary Rings,” *Advances in Space Research*, Vol. 3, No. 3, 1983, pp. 87–94.
- [21] Burns, J. A., Schaffer, L. E., Greenberg, R. J., and Showalter, M. R., “Lorentz Resonances and the Structure of the Jovian Ring,” *Nature*, Vol. 316, No. 6024, 1985, pp. 115–119.
- [22] Schaffer, L. and Burns, J. A., “The Dynamics of Weakly Charged Dust: Motion Through Jupiter’s Gravitational and Magnetic Fields,” *Journal of Geophysical Research*, Vol. 92, 1987, pp. 2264–2280.

- [23] Hamilton, D. P., “Motion of Dust in a Planetary Magnetosphere: Orbit-Averaged Equations for Oblateness, Electromagnetic, and Radiation Forces with Applications to Saturn’s F Ring,” *Icarus*, Vol. 101, 1993, pp. 244–264, Erratum: *Icarus* 103, pp. 161.
- [24] Colwell, J. E. and Horanyi, M., “Magnetospheric Effects on Micrometeoroid Fluxes,” *Journal of Geophysical Research*, Vol. 101, 1996, pp. 2169–2175.
- [25] Colwell, J. E., Horanyi, M., and Grun, E., “Capture of Interplanetary and Interstellar Dust by the Jovian Magnetosphere,” *Science*, Vol. 280, 1998, pp. 88–91.
- [26] Gustafson, B. A. S. and Lederer, S. M., “Interstellar Grain Flow Through the Solar Wind Cavity around 1992,” *IAU Colloq. 150: Physics, Chemistry, and Dynamics of Interplanetary Dust*, edited by B. A. S. Gustafson and M. S. Hanner, Vol. 104 of *Astronomical Society of the Pacific Conference Series*, 1996, pp. 35–38.
- [27] Mullen, E. G., Gussenhoven, M. S., and Hardy, D. A., “SCATHA Survey of High-Voltage Spacecraft Charging in Sunlight,” *Journal of the Geophysical Science*, Vol. 91, 1986, pp. 1074–1090.
- [28] Whipple, E. C., “Potentials of Surfaces in Space,” *Reports on the Progress in Physics*, Vol. 44, 1981, pp. 1197–1250.
- [29] Schaub, H., Parker, G. G., and King, L. B., “Challenges and Prospects of Coulomb Spacecraft Formations,” *Proceedings of the AAS John L. Junkins Symposium*, AAS-03-278, College Station, TX, May 2003.
- [30] Garrett, H. B. and Whittlesey, A. C., “Spacecraft Charging, An Update,” *IEEE Transactions on Plasma Science*, Vol. 28, No. 6, 2000, pp. 2017–2028.
- [31] Lai, S. T., “An Overview of Electron and Ion Beam Effects in Charging and Discharging of Spacecraft,” *IEEE Transactions on Nuclear Science*, Vol. 36, No. 6, 1989, pp. 2027–2032.
- [32] Linder, E. G. and Christian, S. M., “The Use of Radioactive Material for the Generation of High Voltage,” *Journal of Applied Physics*, Vol. 23, No. 11, 1952, pp. 1213–1216.
- [33] Walker, E. H., *Plasma Sheath and Screening Around a Stationary Charged*

Sphere and a Rapidly Moving Charged Body, Ph.D. thesis, University of Maryland, 1964.

- [34] Parker, L. W., *Space Systems and Their Interactions with Earth's Space Environment*, chap. Plasmasheath-Photosheath Theory for Large High-Voltage Space Structures, AIAA, 1980, pp. 477–522.
- [35] Sanmartin, J. R., Martinez-Sanchez, M., and Ahedo, E., “Bare wire anodes for electrodynamic tethers,” *Journal of Propulsion Power*, Vol. 9, June 1993, pp. 353–360.
- [36] Choinière, E. and Gilchrist, B. E., “Self-Consistent 2-D Kinetic Simulations of High-Voltage Plasma Sheaths Surrounding Ion-Attracting Conductive Cylinders in Flowing Plasmas,” *IEEE Transactions on Plasma Science*, Vol. 35, No. 1, 2007, pp. 7–22.
- [37] Mariani, F., Candidi, M., Orsini, S., Terenzi, R., Agresti, R., Musmann, G., Rahm, M., Acuna, M., Panetta, P., Ness, N. F., and Neubauer, F., “Current Flow through High-Voltage Sheaths Observed by the TEMAG Experiment During TSS-1R,” *Geophysical Research Letters*, Vol. 25, No. 4, 1998, pp. 425–428.
- [38] Fuhrhop, K. R., West, B., Choinière, E., Bilén, S. G., and Gilchrist, B. E., “Current Collection to Electrodynamic-Tether Systems in Space,” *Proceedings of the International Energy Conversion Engineering Conference*, AIAA-2004-5670, Providence, RI, August 2004.
- [39] King, L. B., Parker, G. G., Deshmukh, S., and Chong, J., “A Study of Inter-Spacecraft Coulomb Forces and Implications for Formation Flying,” *Proceedings of the AIAA Joint Propulsion Conference*, AIAA-2002-3671, Indianapolis, IN, July 2002.
- [40] Schaub, H., “Stabilization of Satellite Motion Relative to a Coulomb Spacecraft Formation,” *Journal of Guidance, Control, and Dynamics*, Vol. 28, No. 6, 2005, pp. 1231–1239.
- [41] Beletskii, V. V. and Khentov, A. A., “Secular Evolution in the Rotational Motion of a Satellite With an Electrified Shield,” *Kosmicheskie Issledovania (Cosmic Research)*, Vol. 20, No. 3, 1982, pp. 342–351.
- [42] Tikhonov, A. A., “Refinement of the Oblique Dipole Model in the Evolution of Rotary Motion of a Charged Body in the Geomagnetic Field,” *Cosmic Research*, Vol. 40, No. 2, 2002, pp. 157–162.

- [43] Tikhonov, A. A., “A Method of Semipassive Attitude Stabilization of a Spacecraft in the Geomagnetic Field,” *Cosmic Research*, Vol. 41, No. 1, 2003, pp. 69–79.
- [44] Wertz, J. R. and Larson, W. J., *Space Mission Analysis and Design*, Microcosm Press, El Segundo, 1999.
- [45] Forward, R. L., Hoyt, R. P., and Uphoff, C., “The Terminator Tether: A Low-Mass System for End-of-Life Deorbit of LEO Spacecraft,” *Tether Technical Interchange Meeting*, Huntsville, AL, 1997.
- [46] Willems, J. L., *Stability Theory of Dynamical Systems*, Wiley and Sons, New York, NY, 1970.
- [47] DeCarlo, R. A., *Linear Systems*, Prentice Hall, Englewood Cliffs, NJ, 1989.
- [48] Rosenbrock, H. H., “The Stability of Linear Time-dependent Control Systems,” *Journal of Electronics and Control*, Vol. 15, 1963.
- [49] Desoer, C. A. and Haneda, H., “The Measure of a Matrix as a Tool to Analyze Computer Algorithms for Circuit Analysis,” *IEEE Transactions on Circuit Theory*, Vol. 19, No. 5, 1972, pp. 480–486.
- [50] Strom, T., “On Logarithmic Norms,” *SIAM Journal of Numerical Analysis*, Vol. 12, No. 5, 1975, pp. 742–753.
- [51] Soderlind, G., “The Logarithmic Norm. History and Modern Theory,” *BIT Numerical Mathematics*, Vol. 46, 2006.
- [52] Mori, T., Fukuma, N., and Kuwahara, M., “A Stability Criterion fo Linear Time-Varying Systems,” *International Journal of Control*, Vol. 34, No. 3, 1981, pp. 585–591.
- [53] Schaub, H. and Junkins, J. L., *Analytical Mechanics of Space Systems*, AIAA, Reston, VA, 2003.
- [54] Byrnes, D. V., Longuski, J. M., and Aldrin, B., “Cycler Orbit Between Earth and Mars,” *Journal of Spacecraft and Rockets*, Vol. 30, No. 3, 1993, pp. 334–336.
- [55] DARPA Broad Agency Announcement, *Fast Access Spacecraft Testbed (FAST)*, November 2007, BAA 07-65.

- [56] Bilitza, D., “International Reference Ionosphere 2000,” *Radio Science*, Vol. 36, No. 2, 2001, pp. 261–275.
- [57] Gallagher, D. L., Craven, P. D., and Comfort, R. H., “Global Core Plasma Model,” *Journal of Geophysical Research*, Vol. 105, 2000, pp. 18819–18833.